755

755

SANDIA REPORT SAND83-0757 • Unlimited Release • UC-70
Printed August 1983

Comparison of Waste Emplacement Configurations for a Nuclear Waste Repository in Tuff
IV. Thermo-Hydrological Analysis

Lisa A. Mondy, Rodney K. Wilson, Nathan E. Bixler

Prepared by
Sandia National Laboratories
Albuquerque, New Mexico 87185 and Livermore, California 94550
for the United States Department of Energy
under Contract DE-AC04-76DP00789

PREFACE

The Nevada Nuclear Waste Storage Investigations (NNWSI) Project is being conducted for the purpose of examining the feasibility of siting a repository for high-level nuclear waste at Yucca Mountain on, and adjacent to, the Nevada Test Site (NTS). This project is managed by the Nevada Operations Office of the U. S. Department of Energy.

The work described in this report is intended to contribute toward a general understanding of the hydrology for two of three emplacement schemes proposed for the storage of nuclear waste. It is anticipated that this information will be used in a comparison of the two schemes. Funding for this work was provided by the NNWSI Project.

SAND83-0757 Distribution
Printed August 1983 UC-70
Unlimited Release

COMPARISON OF WASTE EMPLACEMENT CONFIGURATIONS FOR A NUCLEAR WASTE REPOSITORY IN TUFF: IV.THERMO-HYDROLOGICAL ANALYSIS

L. A. Mondy, R. K. Wilson and N. E. Bixler
Fluid and Thermal Sciences Department
Sandia National Laboratories
Albuquerque, New Mexico 87185

ABSTRACT

This report summarizes the results of a hydrological analysis of two emplacement schemes being considered for the storage of commercial high level nuclear waste at the Nevada Test Site. The analysis is two-dimensional, considers the flow of water in partially saturated tuff (the Topopah Springs member of the Paintbrush tuff in Yucca Mountain) and includes the effects of the heat source (waste canisters) on that flow. The results include measures of the heat flux entering the access and emplacement drifts, measures of the flow rates near the canisters and a comparison of the temperature fields. It was neccessary in the analysis to approximate the boundary conditions at the walls of the access and emplacement drifts in order to simulate the ventilation process. As a result the analysis was done for several cases which were expected to bracket the actual situation. A discussion of this problem is also included in the report. It should be noted that these results are intended as a means of comparing emplacement schemes, not as a performance assessment.

*This work performed at Sandia National Laboratories supported by the U. S. Department of Energy under Contract DE-AC04-76DP00789.

LIST OF FIGURES

TABLE OF CONTENTS

List of Figures (cont.) Page

Page

List of Figures (cont.)

List of Figures (cont.) Page

LIST OF TABLES

1. INTRODUCTION

Sandia National Laboratories is currently engaged in the study of nuclear waste storage in volcanic tuffs at the Nevada Test Site (NTS). Three emplacement schemes are currently being considered as means of storing canisters of spent fuel (3.4 kW/can). In emplacement scheme 1, self shielding nuclear waste canisters are placed on the floor of drifts transverse to the drift centerlines . In emplacement scheme 2 (the "floor emplacement scheme"), the waste canisters are placed in vertical wells spaced along the drift centerline with isolation plugs sealing the wells (Figures 1-2). In emplacement scheme 3 (the "wall emplacement scheme"), the waste canisters are placed end to end in horizontal boreholes in rock pillars between parallel access drifts. The end of each borehole is sealed with two isolation plugs: one at the drift wall and the other 23.5m into the borehole (Figures 3-5). The region between plugs is filled only with air. In each scheme the gross thermal load is 50 kW/acre.

Here, we present the results of a thermo-hydrological analysis of emplacement schemes 2 and 3. This analysis is one part of an engineering study undertaken by the Fluid & Thermal Sciences Department 1510 and the Engineering Analysis Department 1520 to help select an emplacement scheme [1,2].

In this analysis it was assumed that the repository is located in a partially saturated region of Yucca Mountain, the Topopah Springs member of the Paintbrush Tuff. Thus the finite element code SAGUARO [3], which solves heat and mass transport equations for flow in saturated and partially saturated porous media, was used. We analyzed each scheme with drifts ventilated and unventilated. If the access drift was ventilated, it was assumed that the wall temperature of the drift remained fixed at 25°C. The moisture content at the ventilated drift walls should be less than the in-situ value. The actual moisture content there is unknown a priori, so several values were chosen to bracket the moisture content that would occur in the field. This is discussed further in Appendix A.

The results of this study provide information which should aid in the selection of an emplacement scheme.

(1) Temperature fields were calculated for use in thermo-structural analyses and for determining the volume of rock where the temperature exceeds 100°C (to give an estimate of the amount of water vaporized).

(2) Heat fluxes at the drift wall were calculated for the fixed temperature (25°C) simulating ventilation.

(3) The moisture fluxes into the drift were also determined to aid in comparing emplacement schemes.

(4) Finally, the velocities of fluid flowing past the canisters were calculated to provide a basis for estimating transport rates in the vicinity of the canisters.

The reader is cautioned that the analyses presented here are two-dimensional approximations to three-dimensional problems.

Therefore, the results should NOT be taken as predictions of actual performance. Rather, they represent solutions to simplified problems in which the properties, and therefore the results, are "smeared out" in one of the spatial dimensions. Thus, for example, the maximum temperatures reported in this report should be lower than those which would be obtained from a three-dimensional analysis. Nevertheless, the results should be useful for the purpose of comparing the relative merits of emplacement schemes 2 and 3.

2. THEORETICAL MODEL

SAGUARO, a finite element code developed by R. R. Eaton, et al. [3], was used to model groundwater flow in the partially saturated region near the repository. SAGUARO simultaneously solves Richards equation [4] and a convective/conductive heat transfer equation. Richards equation is a well known extension of Darcy's law [4] for flow through partially saturated porous media and has the form:

$$\frac{\partial}{\partial x_i}\left(\frac{k_{ij}}{\mu}\frac{\partial \Phi}{\partial x_j}\right) - \frac{\partial}{\partial x_i}\left(\frac{k_{ij}}{\mu}\rho_o g \beta \Delta T\right) + \frac{\partial}{\partial x_i}\left(D_{ij}\frac{\partial T}{\partial x_j}\right) = \frac{C}{\rho_o g}\frac{\partial \Phi}{\partial t} \quad . (1)$$

Here, k_{ij} is the intrinsic permeability tensor which is a function of saturation; μ is the dynamic viscosity of water; Φ is the hydraulic head, i.e. the hydrodynamic pressure plus the effective pressure due to gravity,

$$\Phi = \rho_o g(\psi + z) \quad ,$$

where ϕ is the pressure head ($\phi = P/\rho_o g$); ρ_o is the density of water at the reference temperature; g is the acceleration due to gravity; β is the coefficient of volumetric expansion of water; ΔT is the difference between the local temperature and the reference temperature; D_{ij} is the thermal diffusion tensor of water, i.e. it describes the tendency of water to diffuse in the direction of thermal gradients; θ is the local moisture content in the rock; C is the derivative of moisture content with respect to pressure head, $\partial\theta/\partial\phi$; x_i is the i^{th} component in a rectangular coordinate system, shown in Figure 6; and t is time. The superficial water velocity is related to hydraulic head and temperature by [3]:

$$v_i = \frac{-k_{ij}}{\mu}\left(\frac{\partial\Phi}{\partial x_j} - \rho_o g \beta \Delta T \frac{\partial z}{\partial x_j}\right) + D_{ij}\frac{\partial T}{\partial x_j} \quad . \tag{2}$$

The superficial velocity is defined as the average water velocity over a small cross-section consisting of rock, water, and air. In other words, the superficial velocity is smaller than the true pore velocity by a factor equal to the fraction of the local cross-sectional area that is occupied by water:

$$v_i = \theta v_i^* \tag{3}$$

where v_i^* represents the i^{th} component of the true velocity.

The heat transfer equation solved by SAGUARO is:

$$(\rho C_p)_{eff}\frac{\partial T}{\partial t} + (\theta/\phi)\rho_o C_{pf} v_i \frac{\partial T}{\partial x_i} - \frac{\partial}{\partial x_i}\left[\left(\lambda_{eff_{ij}} - \phi E_{ij}\right)\frac{\partial T}{\partial x_j}\right] - Q = 0 \quad . \tag{4}$$

Here, $(\rho C_p)_{eff}$ is the effective volumetric heat capacity of the composite of rock, water, and air; $(\rho_o C_{pf})$ is the volumetric heat capacity of water; $\lambda_{eff_{ij}}$ is the effective thermal conductivity of the composite of rock, water, and air; ϕ is the porosity of the rock; E_{ij} is the thermal dispersion tensor; and Q is a volumetric heat source term.

Thermal diffusion of water in tuffacious rock is generally thought to be negligible (although little experimental data is available to verify this belief), so the thermal diffusion tensor, D_{ij}, was set to zero in this study. The thermal dispersion tensor, E_{ij}, was set to zero for the same reason. With these two simplifications, the third term in Equation (1), the third term in Equation (2), and the fourth term in Equation (4) all drop out. Values of the remaining coefficients in Equations (1)-(4) are given in Section 3.

Figures 7 and 8 show the boundary conditions that were used in SAGUARO. Zero heat flux conditions were imposed on all four sides of the rectangular domains: the zero heat flux conditions on the vertical boundaries are symmetry conditions; the zero heat flux conditions on the upper and lower boundaries are chosen to approximate the conditions far from the canisters. In this study, the upper and lower boundaries were located far enough away from the canisters so that negligible heat penetrated to them during the hundred-year time frame for which calculations were made, that is, the temperatures at the upper and lower boundaries remained constant to within two degrees Celcius during the hundred-year time frame. Zero mass flux conditions were also imposed on the upper and side boundaries of the rectangular domains. The zero flux conditions at the side boundaries again represent symmetry conditions, and the condition at the upper boundary is again a stand-in to approximate the conditions far above the canisters. At the lower boundary the pressure was specified so that the rock at the elevation of the drift was 80% saturated.

Calculations were made for cases in which the storage drifts were ventilated and unventilated. In the cases in which the drifts were unventilated, the above set of boundary conditions were sufficient. However, additional boundary conditions were needed to account for loss of heat and moisture into the air when the storage drifts were ventilated. In reality, the ventilation air absorbs heat and moisture as it travels through the drift. To a good approximation, the heat and mass transfer into the air can be thought of as occurring from the drift wall to a well mixed air core through a thin boundary layer. The boundary conditions consistent with this approximation are of the third kind -- that is, the flux, either heat or mass, is proportional to the difference in conditions, either temperature or moisture, between the drift and the air core. Furthermore, the problem is three-dimensional. However, because the analysis presented here is two-dimensional, it was necessary to simplify the boundary conditions. The conditions chosen were constant temperature and constant moisture content. To provide reasonable comfort for workers, the target temperature for the storage drift is 25°C. The temperature was set to this value at the surface of the drift. A reasonable value of the moisture content at the drift walls was less obvious, so several values were tried and the results compared. Appendix A describes calculations which establish limits on the moisture contents that are possible at the drift walls for the ventilation scheme being considered. These calculations are based on the capacity of the ventilation air to carry away the moisture which enters the drift.

A set of initial conditions were needed to complete the specification of the problem. The initial temperature was chosen to be 25°C everywhere in the domain. The initial hydraulic head was determined from the hydrostatic condition, i.e., no flow initially, and with the saturation at the elevation of the drift equal to 80%. Finally, when the moisture content at the drift walls was fixed, the initial pressure there was specified according to the characteristic curve described in Section 3.

When no driving force for flow of water is imposed, which is the case when no pressure boundary condition is set at the drift walls, the sole mechanism for heat transfer is conduction. SAGUARO does not account for buoyancy forces (free convection) if the saturation is less than 0.99, because liquid must fill the pore space before it can travel upward. In order to determine if free convection might be important for the configurations and heat sources considered here, we used SAGUARO to calculate how much free convection would occur if the medium were saturated. Results showed that free convection was negligible. The details of this calculation are presented in Appendix B. Comparisons were also made between SAGUARO results and results using the heat conduction code COYOTE [10] for cases where convection of water was negligible. These comparisons are described in Appendix C. Agreement was found to be excellent.

3. MATERIAL PROPERTIES AND CHARACTERISTIC CURVES

The candidate horizon is located in the Topopah Springs member of the Paintbrush Tuff in Yucca Mountain at NTS. Using information from references [5-8], the material properties given below were determined for use in the finite element code SAGUARO. Note that the air in the drift and in the air gap of emplacement scheme 3 was given an artificially high value of thermal conductivity to simulate radiation effects [7]. The permeability of the air was chosen to be four orders of magnitude larger than that of the rock. Thus the resistance to water flow through the drift and the air gap was negligible compared to the resistance in the rock. SAGUARO computes volume averaged properties for heat capacity and thermal conductivity from the intrinsic properties given in Table 1.

In partially saturated regions, the permeability (or hydraulic conductivity) and saturation are strongly dependent on the pressure head [3]. The dependences of permeability and saturation on pressure head used in this analysis are represented by the curves shown in Figures 9-11.

TABLE 1. Material Properties

MATERIAL PROPERTY	VALUE		REFERENCE
grain density of tuff	2550.	kg/m^3	[5]
density of air*	1.177	kg/m^3	[6]
density of water*	974.1	kg/m^3	[6]
density of "rock"**	2338.	kg/m^3	**
porosity	0.12		[5]
initial saturation	0.80		[5]
thermal conductivity of tuff***	1.972	W/m°C	[5]
thermal conductivity of canister	1.16	W/m°C	[1]
thermal conductivity of air in drift (artificially high to account for radiation)	25.	W/m°C	[7]
thermal conductivity of water*	0.668	W/m°C	[5]
heat capacity of tuff***	795.	J/kg°C	[5]
heat capacity of canister	939.	J/kg°C	[1]
heat capacity heat of air*	1009.	J/kg°C	[6]
heat capacity of water*	4196.	J/kg°C	[6]
permeability of tuff (saturated)	8.0×10^{-15}	m^2	[5]

*During most of the time frame of interest, the temperatures are greater than 50°C. In many cases it is greater than 100°C. Therefore, the properties for air and water were taken at 80°C.

**The properties of the "rock" refer to the mixture of tuff, air and water and represent a volume or density weighted value. For example, the density of the "rock" is computed by
ρ_{rock} = (0.88)(2550.) + (0.80)(0.12)(974.1) + (0.20)(0.12)(1.177) = 2338. kg/m^3

***These intrinsic tuff properties were calculated from the average properties for the tuff, air and water matrix given in reference [5].

4. COMPUTATION OF THE VOLUMETRIC HEAT SOURCE

(i) Emplacement Scheme 2

The analysis in this report is based on the emplacement of spent fuel that gives a gross thermal loading of 50 kW/acre [1]. Referring to Figure 2 this loading is equivalent to placing a volumetric heat source in the canister with an initial value determined by:

$$Q_o = (TPO)/(W)(H)(P)$$

where

TPO = Thermal power output per canister (3.4 kW)
W = Diameter of heat source (0.6452 m)
H = Height of heat source (4.084 m)
P = Pitch (distance between canisters located in the same drift) (11.034 m)

Thus

$$Q_o = 116.233 \text{ W/m}^3 = 3.666 \times 10^9 \text{ J/m}^3\cdot\text{yr}.$$

The heat source decays exponentially. Decay data obtained from [8] is given below and shown graphically in Figure 12.

TABLE 2. Decay Data for Heat Source

TIME (YRS)	Q/Q_o
0	1.0
1	0.95
2	0.907
3	0.871
4	0.851
5	0.810
6	0.783
7	0.769
8	0.734
9	0.714
10	0.692
15	0.600
20	0.529
30	0.402
40	0.313
70	0.157
100	0.0864

(ii) Emplacement Scheme 3

Referring to Figure 4, the 50 kW/acre gross thermal load is equivalent to placing a volumetric heat source in the effective canister volume according to:

$$(S)(L)(GTL) = Q_o(D)(L-2A)(S)$$

where

GTL	=	gross thermal load	(50 kW/acre)
Q_o	=	initial magnitude of heat source	
S	=	spacing between parallel torpedo tubes	(45.415 m)
L	=	distance between access drifts	(206 m)
A	=	stand off distance	(24.384 m)
D	=	diameter of torpedo tube	(0.6416 m)

Thus

$$Q_o = 25.327 \text{ W/m}^3 = 7.987 \times 10^8 \text{ J/m}^3\cdot\text{yr} \quad .$$

The decay of the heat source is the same for both emplacement schemes (Figure 12).

5. RESULTS

a. TEMPERATURE FIELDS

Isotherms calculated using SAGUARO are shown in Figures 13-18 and 20-25. In Figures 13-18 the isotherms for emplacement scheme 2 are shown at 1, 10, 50 and 100 years. The maximum rock temperatures reached during the 100 year time interval are shown in Table 3.

TABLE 3. Maximum Rock Temperatures During 100 Year Period
Emplacement Scheme 2

CASE	SATURATION AT DRIFT WALL	T(MAX)
VENTILATED (25°C)	0.80	96°C
	0.78	96°C
	0.751	96°C
	0.635	95°C
	0.47	94°C
UNVENTILATED	0.80	110°C

The location of the maximum temperature at early times is shown in Figure 19. It is interesting to note that the maximum temperature of the rock never exceeded 100°C for the ventilated case. For the unventilated case it did, and this fact may be important for investigating vapor transport.

For emplacement scheme 3 the isotherms are shown in Figures 20-25. In this case the maximum temperatures are:

TABLE 4. Maximum Rock Temperatures During 100 Year Period
Emplacement Scheme 3

CASE	SATURATION AT DRIFT WALL	T(MAX)
VENTILATED (25°C)	0.80	106°C
	0.78	105°C
	0.751	104°C
	0.635	102°C
	0.47	99°C
UNVENTILATED	0.80	107°C

For emplacement scheme 3 the location of the maximum temperatures are shown in Figure 26. In this case the maximum temperatures do exceed 100°C. Moreover, three-dimensional thermal analysis [11] has shown that the two-dimensional calculations presented here underestimate the volume enclosed by the 100°C isotherm. We note that the temperatures calculated using SAGUARO are higher than those calculated in two-dimensions using COYOTE in reference [11]. This is due to the fact that the heat of vaporization of water cannot be accounted for in SAGUARO.

Because of the proximity of the canister to the drift in emplacement scheme 2, the greatest change in the temperature profiles was caused by assuming that the temperature at the drift was 25°C (to simulate ventilation), as shown in Table 3. The fluid flow caused by the saturation boundary condition at the drift influenced the temperature profiles less. In emplacement scheme 3, however, water passing the canisters had a pronounced cooling effect, as shown in Table 4.

b. HEAT FLUX CALCULATIONS

Heat fluxes at the drift wall were calculated using SAGUARO for both emplacement schemes 2 and 3. It is difficult to directly compare results for the two emplacement schemes; however, we have provided the results in two forms. We have computed the amount of heat removed from the drift per canister and per unit length of drift and plotted the values as functions of time. Referring to Figures 27 and 28, the results indicate two things. First, more heat is removed per canister as the moisture content at the drift wall is reduced. Second, it appears that more heat is removed per canister in emplacement scheme 2 than in emplacement scheme 3. However, more heat per unit length of drift is removed in emplacement scheme 3. Therefore, given the same number of canisters in the repository, more ventilation would be required for emplacement scheme 2; but, given the same amount of drift footage, more heat must be removed for emplacement scheme 3.

The heat flux necessary to keep the drift at 25°C reaches a peak in 10 to 20 years after emplacement in scheme 2. In emplacement scheme 3, however, the peak is reached much later. In fact, only in the case where the saturation at the drift wall is 0.47 is the peak reached within the 100 year time frame. This is because the heat source represented by the tube of canisters is not only 34 times as long but more than twice as far away from the drift as the heat source represented by the single canister placed below the drift in emplacement scheme 2. Thus, at 100 years energy is still arriving at the drift wall from the farthest canister in the emplacement scheme 3.

c. MOISTURE FLUX INTO THE DRIFT

The average superficial velocities into the drift and corresponding volumetric flow rates through the drift are listed for each case in Table 5.

TABLE 5. Moisture Flux Results (at 100 years)

SATURATION AT DRIFT WALL	SUPERFICIAL VELOCITY (m/s)	VOLUMETRIC FLOW RATE $(m^3/day)/m$ length of drift
EMPLACEMENT SCHEME 2		
0.78	0.24×10^{-8}	0.0044
0.751	0.63×10^{-8}	0.0166
0.635	2.4×10^{-8}	0.0443
0.47	5.5×10^{-8}	0.1014
EMPLACEMENT SCHEME 3		
0.78	0.99×10^{-8}	0.0209
0.751	2.95×10^{-8}	0.0621
0.635	11.39×10^{-8}	0.2400
0.47	27.53×10^{-8}	0.5800

We note that the velocities for emplacement scheme 3 are larger than those for emplacement scheme 2. The primary reason for this is that the flow is disturbed in a much larger zone. Recall that the tube of canisters is represented as a plate that extends the entire distance between tubes. Since the canisters are impermeable, this plate prevents upward flow past the canisters and, instead, tends to direct flow towards the drift. In reality, the tube would offer much less resistance to flow, since there would be a path around the canisters. Remember that these velocities result only from pressure gradients (forced convection), since SAGUARO neglects buoyancy in partially saturated media.

d. FLOW RATES PAST CANISTERS

To provide a basis for estimating transport rates in the vicinity of the canisters, we consider the velocities occurring near the canisters. These results are presented in graphical form in order to show the localized nature of the flow.

(i) Emplacement Scheme 2: Figures 29-32 show the horizontal velocity distributions along a plane that extends from the mid-point of the canister wall towards the right hand boundary (symmetry plane) for several values of moisture content at the drift wall. In these figures curves marked with 0, 1, 2, 3, 4 and 5 represent 0.67, 1, 10, 30, 50 and 100 years, respectively. Note that the curves for times greater than 1 year often overlap. The horizontal velocity component increases in magnitude for approximately six meters and then decreases to the specified zero value at the symmetry plane. Furthermore, the magnitudes increase for smaller moisture contents. Figures 33-36 show the vertical component of velocity along this same plane. Magnitudes of vertical velocity decrease monotonically from a maximum value near the can to zero at the symmetry plane. In Figures 37-44 the velocity components are shown along a vertical plane extending from the bottom boundary to the top, about 0.6 m to the right of the drift wall. It is clear from these figures that during the 100 year time period the change in moisture content resulting from the emplacement scheme (drift and canister) affects the flow over a region only sixty meters in length.*

*In these figures, the curve marked with a "0" represents the velocities at very early times (less than one year) and does not represent the actual flow but a change of the initial state by the application of jump conditions, which are not physical, at the boundaries. This applies to the velocity profile plots for both emplacement schemes.

(ii) Emplacement Scheme 3: Figures 45-68 show velocity profiles along three cross sections for emplacement scheme 3. In these figures curves marked with 0, 1, 2, 3, 4 and 5 represent 1, 10, 30, 50, 70 and 100 years, respectively. Figures 45-48 are horizontal velocity profiles along a horizontal plane which cuts through the rock about 4 m below the drift floor. Results for four values of moisture content at the drift walls are shown. The curves are all similar except that the magnitudes increase as drift wall moisture content decreases, as expected. In each of the curves, the velocities are to the left (toward the drift) and increase in magnitude below the drift, decrease through a minimum below the air gap then increase again, and decrease to zero at the symmetry plane through the midpoint of the torpedo tube. Vertical velocities along the same plane are upward in direction and increase in magnitude from nearly zero near the tube midpoint. Again, there is a local maximum beneath the air gap. As with the horizontal velocities, the magnitudes of the vertical velocities increase with decreasing drift wall moisture content. Figures 49-68 show velocity profiles along two vertical cross sections about 4 m from the drift and 14 m from the tube midpoint for the same four values of moisture content at the drift walls. The main conclusions from these figures are that the water flows in a narrow region, about 10 m below to 10 m above the tube, near the drift, but in a much wider region near the tube midpoint. However, the velocities are much smaller near the tube midpoint than they are near the drift. The complicated nature of the velocity profiles in Figures 45-68 is due to the highly non-linear dependence of permeability on saturation and to the wide differences in properties of the air, canisters and rock.

Table 6 summarizes the maximum true velocity near the canisters. Recall that in emplacement schemes 2 and 3 this velocity occurs at the end of the canister nearest the drift. Note, however that in emplacement scheme 2 the velocities are nearly the same everywhere near the canister, while for emplacement scheme 3 the velocities decrease in magnitude for each canister as their position relative to the drift increases (i.e., as they become closer to the symmetry plane where the velocity is zero.) Also note that the values which appear in Table 6 are TRUE velocities, not superficial velocities (cf. equation 3)).

TABLE 6. Maximum Velocities Near Canisters

MOISTURE CONTENT	MAXIMUM TRUE VELOCITIES (m/s)
Emplacement Scheme 2	
0.78	0.37×10^{-7}
0.751	0.97×10^{-7}
0.635	3.68×10^{-7}
0.47	8.42×10^{-7}
Emplacement Scheme 3	
0.78	0.81×10^{-7}
0.751	2.44×10^{-7}
0.635	9.82×10^{-7}
0.47	23.01×10^{-7}

6. SUMMARY

In this report we have presented an analysis of the thermohydrology of two emplacement schemes being considered for the storage of nuclear waste in partially saturated tuff. This analysis includes the effects of the emplacement drifts on the in situ flow as well as the effects of the heat source on the undisturbed rock temperatures. Included in the results of this study are estimates of the moisture flux into the drift, the heat flux into the drift, the maximum rock temperatures and fluid velocities reached during the 100 year time period. All of these quantities are important in making a decision as to which emplacement scheme is best. The main conclusions that can be drawn from the analysis are:

1) The maximum rock temperatures attained in emplacement scheme 3 are at least 10°C higher than those in emplacement scheme 2, if the drift wall is maintained at 25°C.
2) During the first 30 years, emplacement scheme 2 requires approximately six times more heat to be removed from the repository per canister than does emplacement scheme 3.
3) At the most likely drift wall saturation, the calculated moisture flux into a drift configured in emplacement scheme 3 is four times greater than in emplacement scheme 2; however, the two dimensional approximation of the tube as a slab is a worst case analysis.
4) Subject to the same approximation as in 3), the maximum, calculated, groundwater flow near the canisters is two or three times greater in emplacement scheme 3 as in 2. The order of magnitude of the velocity is likely to be 1 m/yr.

Although the analyses reported here are of two-dimensional approximations to complicated three-dimensional problems, and although some of the material properties are uncertain, the analyses are consistent so that the two emplacement schemes can be compared with some assurance.

ACKNOWLEDGEMENT

Discussions with Roger Eaton were invaluable in completing this work. We would like to express our extreme appreciation to him for sharing time with us.

REFERENCES

[1] Engineering Studies to Determine a Nuclear Waste Emplacement Scheme, memo from L. W. Scully to J. W. Nunziato, D. F. McVey and R. D. Krieg, dtd. August 11, 1982.

[2] Engineering Studies to Determine a Nuclear Waste Emplacement Scheme, memo to L. W. Scully from J. W. Nunziato, D. F. McVey and R. D. Krieg, dtd. November 1, 1982.

[3] Eaton, R. R., Gartling, D. K. and Larson, D. E., "SAGUARO -- A Finite Element Computer Program for Partially Saturated Porous Flow Problems", Sandia National Laboratories, Report No. SAND82-2772 (1983).

[4] Freeze, R. A. and Cherry, J. A., Groundwater, Prentice Hall Inc., Englewood Cliffs (1979).

[5] Average Properties for Potential Emplacement Horizon in the Topopah Springs Member of the Paintbrush Tuff, memo from R. R. Peters to distribution, dtd. May 19, 1982.

[6] Karlekar, B. V. and Desmond, R. M., Engineering Heat Transfer, West Publishing Co., St.Paul (1977).

[7] The Effect of Thermal Radiation in the Disposal of High Level Waste (HLW) in Tuff, memo from O. L. George Jr. to D. F. McVey, dtd. January 4, 1980.

[8] Eaton, R. R., Martinez, M. J., Wilson, R. K. and Nunziato, J. W., "Code development in Support of Nuclear Waste Storage Isolation", Sandia National Laboratories, Report No. SAND82-2771 (1983).

[9] Kisner, R. A., et al., "Nuclear Waste Projections and Source Term Data for FY1977", Y/OWI/TM-34, (Washington D.C.: Office of Waste Isolation, April 1978).

[10] Gartling, D. K.,"COYOTE -- A Finite Element Computer Program for Nonlinear Heat Conduction Problems", Sandia National Laboratories, Report No. SAND77-1332 Revised (1982).

[11] Bixler, N. E, et. al., "Comparison of Waste Emplacement Configurations for a Nuclear Waste Repository in Tuff: I. Thermal Analysis", Sandia National Laboratories, Report No. SAND83-0860 (1983).

[12] Hickox, C. E., "Comparison of Waste Emplacement Configurations for a Nuclear Waste Repository in Tuff: II. Ventilation Analysis", Sandia National Laboratories, Report No. SAND83-0678 (1983).

[13] Perry, R. H. and Chilton, C. H., editors, Chemical Engineering Handbook, 5th Ed., McGraw-Hill Book Co., Inc., New York (1973).

[14] Dittus, F. W. and Boelter, L. M. K., Univ. Calif., Pubs. Eng., Vol. 2, 1930. (Also, see McAdams, W. H., below.)

[15] McAdams, W. H., Heat Transmission, 3rd Ed., McGraw-Hill Book Co. Inc., New York (1954).

APPENDIX A. Computation of Moisture Content at the Drift Walls for Ventilation Boundary Conditions

Ventilation of underground drifts is likely to carry moisture from the walls into the ventilation stream. The drying, or lowering of the moisture content of the walls, produces a saturation gradient which can be a driving force in porous flow. The actual amount of drying is difficult to predict; however, a bounding value can be estimated from mass transfer correlations, if it is assumed that the resistance to flow from the porous material is less than the resistance to mass transfer from the wall to the air stream. Bounding values of the velocities of water flowing into the drift are calculated in this appendix. SAGUARO is used to estimate the saturation gradients (i.e., the difference between the saturation at the drift wall and in the native rock) necessary to drive water into the drifts at these calculated velocities. This information is in turn used to set the moisture content at the drift wall to simulate ventilation in the analyses described in the main body of this report.

According to ventilation studies by Hickox [12], a likely maximum air velocity, $\overline{V}$, for a 200 meter long drift for emplacement scheme 2 is 0.555 m/s. Emplacement scheme 3 is likely to have longer ventilated drifts. Thus, for emplacement scheme 3, the maximum velocities will range from 0.323 m/s for 200 m long drifts to 0.695 m/s for 1362 m long drifts.

The maximum amount of water that can be carried from the drift is the amount of water in a stream of saturated air:

$$\dot{m}_{H_2O} = (\overline{V}_{\substack{dry\\air}})(A_x)(\rho_{\substack{dry\\air}})\ (CW) \quad , \qquad (A.1)$$

where $\dot{m}_{H_2O}$ is the mass flow rate of water out of the drift, $\overline{V}_{\substack{dry\\air}}$ is the average stream velocity, A_x is the cross-sectional area of the drift, $\rho_{\substack{dry\\air}}$ is the density of dry air at the temperature and pressure in the drift and CW is the moisture content of the air in units of mass of liquid per mass of dry air. If the air is assumed to enter in a completely dry state and exit fully saturated at 25°C, the maximum mass of water per second that can be carried from a drift in configuration 2 is

$$(\dot{m}_{H_2O})_{max} = (0.555\ m/s)(4.57\ m)(6.1\ m)\left(1.774\ \frac{kg\ air}{m^3}\right)\left(0.0202\ \frac{kg\ H_2O}{kg\ air}\right)$$

$$= 0.554\ kg\ H_2O/s\ = 527\ gal\ H_2O_{liq}/hr.$$

The properties of air are from a standard psychometric chart [13]. Table A.1 gives a list of the maximum flow rates for emplacement scheme 3 as well.

The amount of water leaving the drift must equal the amount coming through the drift walls from the porous rock, if the entrance air is dry and there is no accumulation of water in the drift. Assuming that the water comes through the porous matrix as liquid only, the average superficial velocity into the drift, for configuration 2, is

$$\overline{v}_{max} = (\dot{m}_{H_2O})(\rho_{H_2O})^{-1}\ (A_s)^{-1} \qquad (A.2)$$

$$= \left(0.554\ \frac{kg\ H_2O}{s}\right)\left(999.\ \frac{kg\ H_2O}{m^3}\right)^{-1}\ [(2.)(199.95\ m)(4.57\ m + 6.1\ m)]^{-1}$$

$$= 1.3 \times 10^{-7}\ m/s,$$

TABLE A.1. Maximum Amount of Water Carried by Ventilation Stream

Emplacement Scheme	Drift Length	Dry Air Vel.	Mass Flow of Water into Air Stream		Superficial Water Velocity into Drift
	L	$\bar{V}$	$(\dot{m}_{H_2O})_{max}$		$\bar{v}_{max}$
	(m)	(m/s)	(kg/s)	(gal/hr)	(m/s)
2	200	0.555	0.554	527	1.3×10^{-7}
3	200	0.323	0.431	410	8.8×10^{-8}
3	1362	0.695	0.927	882	2.8×10^{-8}

where ρ_{H_2O} is the density of liquid water at the conditions at the drift wall (1 atmosphere pressure and 25°C) and A_s is the total surface area drying. Table A.1 lists the average velocities calculated from Equation (A.2).

The above calculations predict an upper bound on the amount of water that can be carried out by ventilation air at 25°C. There is no resistance to mass transfer at the drift wall. The ventilation air is likely to emerge from the drift in only a partially saturated state. Moreover, the amount of heat required to evaporate an amount of water this large exceeds the thermal output of the canisters.

A more realistic calculation can be done by allowing for a mass transfer coefficient in the mass balance equation and then coupling the mass balance equation with the heat balance equation. The rate at which heat is transferred to the ventilation air per unit length of drift must be equal to the rate of heat transfer into the drift from the canisters minus the rate at which heat is used to evaporate water, that is

$$h\Gamma(T_w - T_a) = q/L - \lambda\dot{m}_{H_2O}/L \quad , \qquad (A.3)$$

where q/L is a heat transfer rate per unit length calculated in the thermal analyses reported on in the main body of this report. This quantity is listed in Table A.2 for the two configurations studied. For the purposes of this analysis, it is assumed that the drifts will be ventilated for only 50 years. Thus q/L for configuration 2 is taken to be the maximum (seen at approximately 20 years), while for configuration 3 it is taken as the heat

TABLE A.2. Heat Transfer from Canisters for Ventilation Studies

Emplacement Scheme	Drift Length	Heat Conducted into Drift	Time
	L	(q/L)	t
	(m)	(w/m)	(yrs)
2	200	117.	20
3	200	138.	50
3	1362	138.	50

transfer rate at 50 years even though a maximum value has not yet been reached. The other parameters in Equation (A.3) include the drift length L, the heat of vaporization of the water λ, the heat transfer coefficient h, the perimeter of the drift Γ, and the temperature of the wall T_w and of the bulk air T_a.

The amount of heat per unit time that is available to heat the air from its entrance temperature T_{ao} to the temperature $T_a(x)$ at any distance x along the length of the drift is calculated from

$$\rho \overline{V} A_x C_p (T_a - T_{ao}) = (q/L)x - \lambda \left(\frac{\dot{m}_{H_2O}}{A_s(L)} \right) A_s(x) \quad , \qquad \text{(A.4)}$$

where ρ is the bulk density of the air, $\overline{V}$ is the average air velocity, C_p is the bulk heat capacity of the air, $A_s(L)$ is the total surface area of the drift and $A_s(x)$ is the amount of surface area in a length x of the drift.

Combining equations (A.3) and (A.4), one can solve for the wall temperature at the midpoint of the drift (x = L/2):

$$(T_w)_m = \frac{(q/L) - (\lambda \dot{m}_{H_2O}/L)}{h\Gamma} + \frac{(q/L)(L/s) - \lambda \left(\frac{\dot{m}_{H_2O}}{A_s(L)} \right) \left(A_s(L/2) \right)}{\rho \overline{V} A_x C_p} + T_{ao} \quad . \qquad \text{(A.5)}$$

The mass flow rate of water can be estimated using a mass transfer coefficient

$$\dot{m}_{H_2O} = w \cdot MW_{H_2O} = k \cdot A_s(L) \cdot MW_{H_2O} \frac{(X_{H_2O,w} - X_{H_2O,\infty})}{(1 - X_{H_2O,w})} \quad , \qquad \text{(A.6)}$$

where w is the molar flow across the surface, MW_{H_2O} is the molecular weight of water, k is the mass transfer coefficient,

$X_{H_2O,w}$ is the mole fraction of water at the surface and $X_{H_2O,\infty}$ is the mole fraction in the bulk air phase.

If one assumes that the air and water vapor form an ideal mixture, then it is possible to estimate the mass fraction of water vapor by

$$X_{H_2O} = \frac{P_{H_2O}}{P_T} \quad , \tag{A.7}$$

where P_{H_2O} is the partial pressure of water and P_T is the total pressure. At the drift wall,

$$X_{H_2O,w} = \frac{P_{H_2O,sat}(T_w)}{P_T} \quad , \tag{A.8}$$

where $P_{H_2O,sat}(T_w)$ is the saturation pressure (at 100% relative humidity) evaluated at the temperature of the drift wall. The partial pressures can be found from psychometric charts knowing only the temperature and the relative humidity.

The heat transfer coefficient for a developing flow in a tube subjected to a uniform wall temperature is given by the relationship developed by Dittus and Boelter and modified by McAdams [12,14,15].

$$Nu = \frac{hD}{K} = 0.023(Re)^{0.8} (Pr)^{1/3} [1 + (D/L)^{0.7}], \tag{A.9}$$

where Nu is the Nusselt number, h is the heat transfer coefficient, D is the hydraulic diameter (4 x cross-sectional area/wetted perimeter), K is the thermal conductivity of the bulk air, Re is the Reynolds number ($\overline{V}D/\nu$) and Pr is the Prandtl number (ν/α). Here, ν is the kinematic viscosity of the bulk air and α is the thermal diffusivity. Equation (A.9) is valid for Re > 10^4 and 0.7 < Pr < 12. An approximation is made at the drift wall by assuming that it is at a uniform temperature and that the heat transfer coefficient is taken from Equation (A.9).

The analogy between mass and heat transfer gives a mass transfer coefficient. Replacing the Prandtl number with the Schmidt number ($\mu/\rho \mathscr{D}_{AB}$) gives a Nusselt number (or Sherwood number) for mass transfer:

$$Nu_{AB} = \frac{kD}{c\mathscr{D}_{AB}} = 0.023\ (Re)^{0.8}\ (Sc)^{1/3}\ [1 + (D/L)^{0.7}], \qquad (A.10)$$

where k is the mass transfer coefficient, c is the concentration in moles/volume (for ideal gases this is a function of temperature and pressure only), and $\mathscr{D}_{AB}$ is the diffusivity of the system.

With $(T_w)_m$ fixed at 25°C, the system of equations (A.5), (A.6), (A.9) and (A.10) can be solved simultaneously to determine the four unknowns $\dot{m}_{H_2O}$, $\overline{V}$, k and h. The incoming air is assumed to be at 20°C. To obtain the mole fractions the ventilation air is assumed to be 50% saturated with water and at a bulk temperature of 20°C. The diffusivity is taken to be that of water vapor in nitrogen. The bulk properties of the ventilation air are estimated to be those of dry air at 20°C. Table A.3 lists the values of the parameters used.

The results are tabulated in Table A.4. The superficial velocity of water flowing through the porous matrix and into the drift is calculated as in equation (A.2). The velocity of the air stream ($\overline{V}$) is so low that the Reynolds numbers

TABLE A.3. Material Properties

Property	Value	Units
ρ	1.2104	kg/m^3
C_p	1.0056×10^3	J/kg°C
μ	1.914×10^{-5}	kg/ms
ν	1.481×10^{-5}	m^2/s
K	2.568×10^{-2}	W/m°C
α	2.090×10^{-5}	m^2/s
$\mathcal{D}_{H_2O,N_2}$	2.5×10^{-5}	m^2/s
$X_{H_2O,\infty}$	1.16×10^{-2}	--
$X_{H_2O,w}$	3.13×10^{-2}	--
Pr	0.709	--
Sc	0.63	--
λ	2.44×10^6	J/kg

TABLE A.4. Heat and Mass Balance of Water Evaporation from Drifts

Emplacement Scheme	Drift Length	Dry Air Velocity	Mass Flow of Water into Air Stream	Superficial Water Velocity into Drift
	L	$\bar{V}$	$\dot{m}_{H_2O}$	$\bar{v}$
	(m)	(m/s)	(kg/s)	(m/s)
2	200	0.024	0.0087	2.0×10^{-9}
3	200	0.026	0.01	2.0×10^{-9}
3	1362	0.03	0.074	2.2×10^{-9}

are approximately equal to 10^4. This is barely within the range of the correlation given in equation (A.9); however, because the transition region is not well understood and because the calculations include other approximations, it is felt that the heat transfer coefficient can still be estimated most accurately by using equation (A.9).

The superficial velocities listed in Table A.4 are conservative, in the sense that they are high, because it is assumed that there is no resistance to flow through the porous matrix and that the water on the wall is being replenished constantly so that a steady source exists for evaporation. It is also assumed that the entire surface of the drift is available for mass transfer, not just the area occupied by the pores. It should be emphasized for the same reasons that the calculated ventilation rates are not conservative because a higher rate may actually be needed to maintain the wall temperature at 25°C if less water is evaporated. The water velocities listed in Table A.4 are much more likely to occur than the maximum velocities that could possibly exist (Table A.1). SAGUARO was used to estimate the steady-state saturation at the drift wall that would produce a driving force capable of creating both the maximum velocities in Table A.1 and the more likely velocities given in Table A.4. These saturations are listed in Table A.5. The models used to reach the conclusions in this report were based on drift wall moisture contents in this range.

TABLE A.5. Velocities into Drift and Corresponding Boundary Saturations

Emplacement Scheme	Drift Length	Superficial Water Velocity into Drift	Approximate Saturation at Drift Wall
	L (m)	$\bar{v}$ (m/s)	θ_{drift}/ϕ
2	200	2.0×10^{-9}	0.78
		1.3×10^{-7}	< 0.4
3	200	2.0×10^{-9}	> 0.78
		8.8×10^{-8}	0.65
3	1362	2.2×10^{-9}	> 0.78
		2.8×10^{-8}	0.75

APPENDIX B. Comparison between Fully Saturated Results and Partially Saturated Results

In this appendix, a comparison is made between the results of a fully saturated analysis, in which SAGUARO does account for free convection, and the results of a partially saturated analysis in which buoyancy is neglected. This is done in order to determine the degree to which free convection could become important if the repository were to become saturated as a result of extremely unlikely hydrologic situations. To this end, we will compare temperature histories for the unventilated conditions in emplacement scheme 2 only.

In Figures 70 and 71, temperature histories are shown for six locations near the drift and two locations near the canister (these points, identified in Figure 69). These histories show that the maximum temperatures for the saturated case are within 2-3°C of those in the unsaturated case. This implies that free convection has little effect on the temperature profiles. The largest velocities calculated for the saturated case are extremely small (causing the fluid to travel less than a meter in 1000 years). One should remember, however, that in this two-dimensional analysis the heat source has been "smeared." A three-dimensional analysis would have a higher source in a smaller region, which could cause more convection locally.

APPENDIX C. Comparison between SAGUARO Results and COYOTE Results

In this appendix, a check on the results obtained using SAGUARO is made by comparing the temperature fields with those obtained using the heat conduction code COYOTE. Because we cannot include the effects of water vaporization in SAGUARO, the effects were also omitted in the COYOTE analysis. In both cases the results will not compare to what would be obtained if water vaporization were included in COYOTE. Therefore one is cautioned not to compare any of these results with those obtained in the thermal analyses [11], where all effects are included.

In Figures 70 and 72, temperature histories are shown for emplacement scheme 2 at six locations near an unventilated drift and two locations near the canister. The temperatures vary less than 2°C between codes, which is within the tolerances of comparing the two codes.

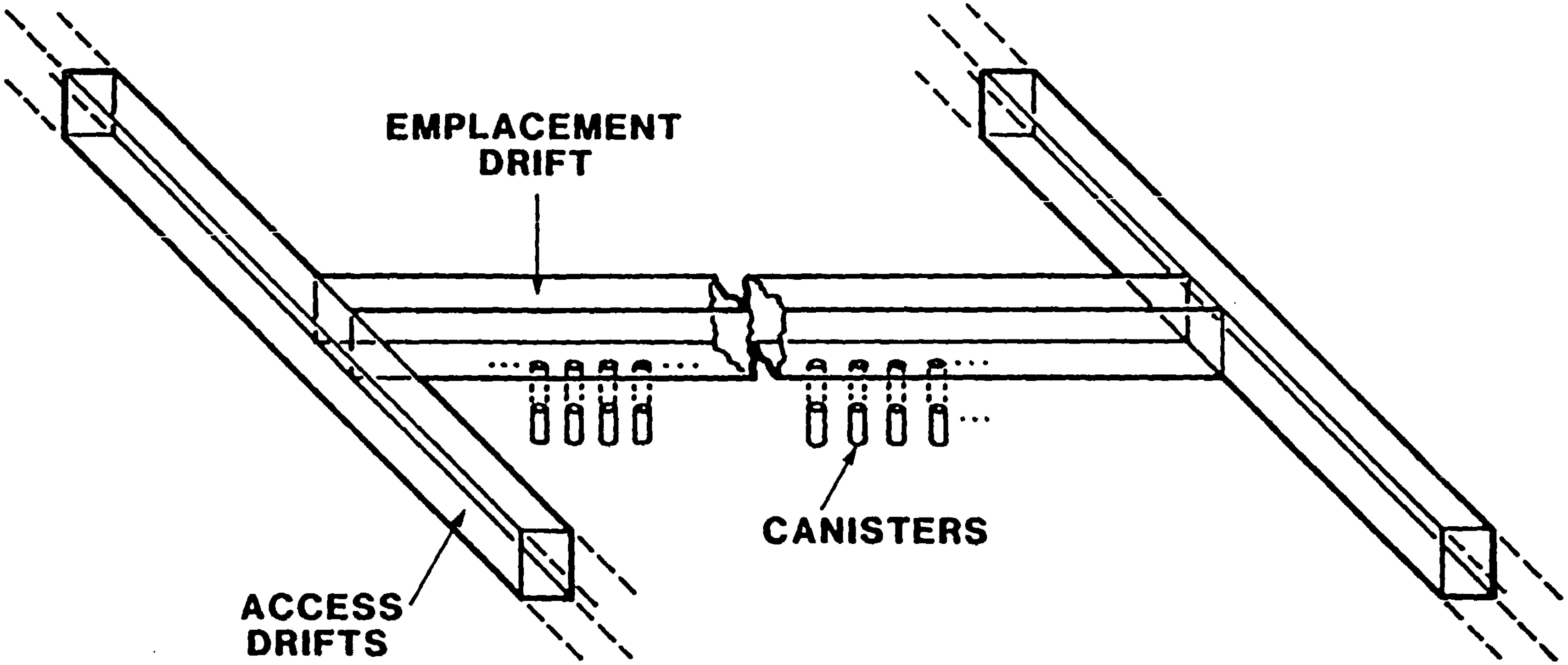

Figure 1. Layout for Emplacement Scheme 2.

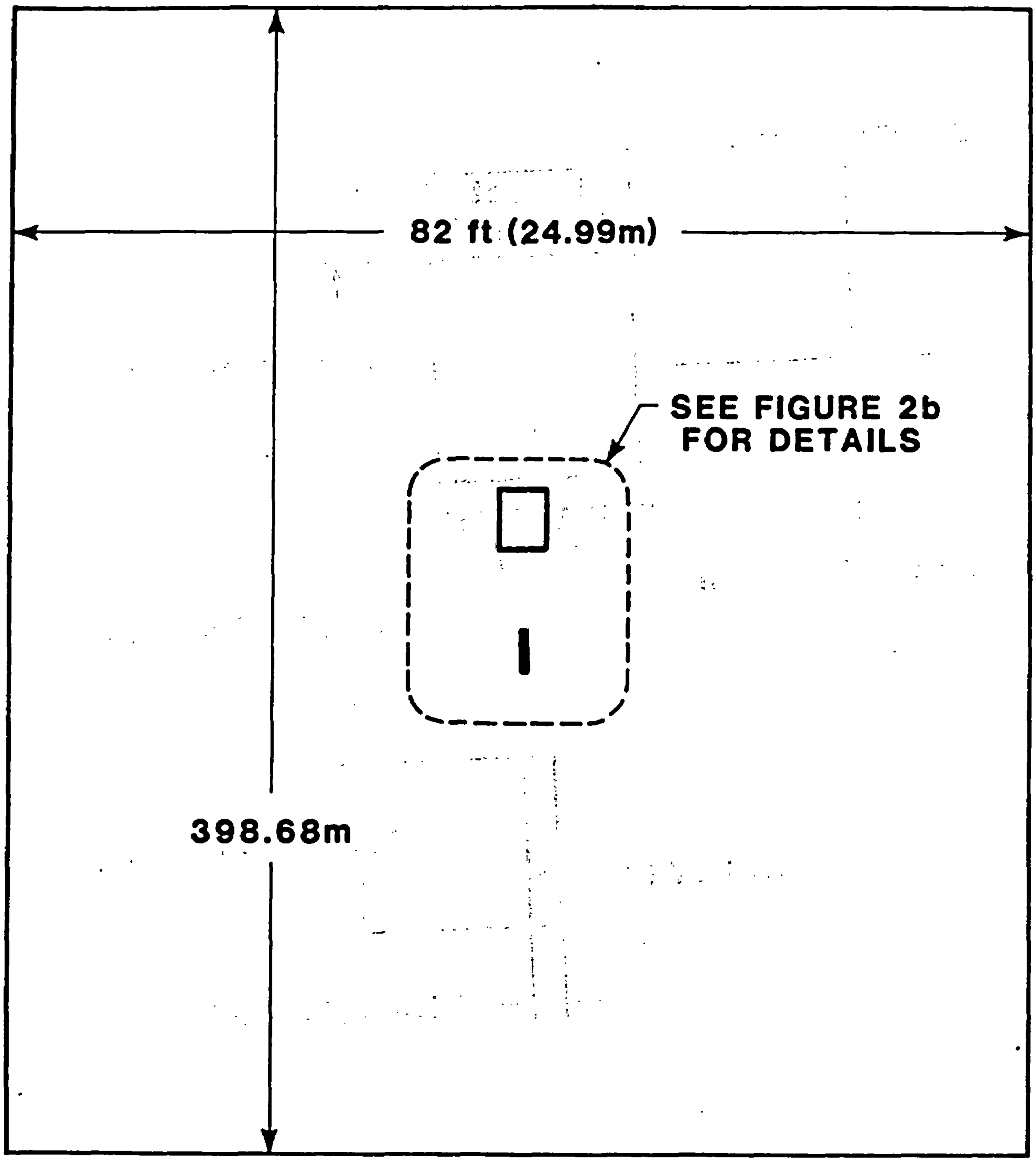

Figure 2a. Cross-Section of the Two-Dimensional Model for Emplacement Scheme 2 showing Dimensions of Outer Boundaries

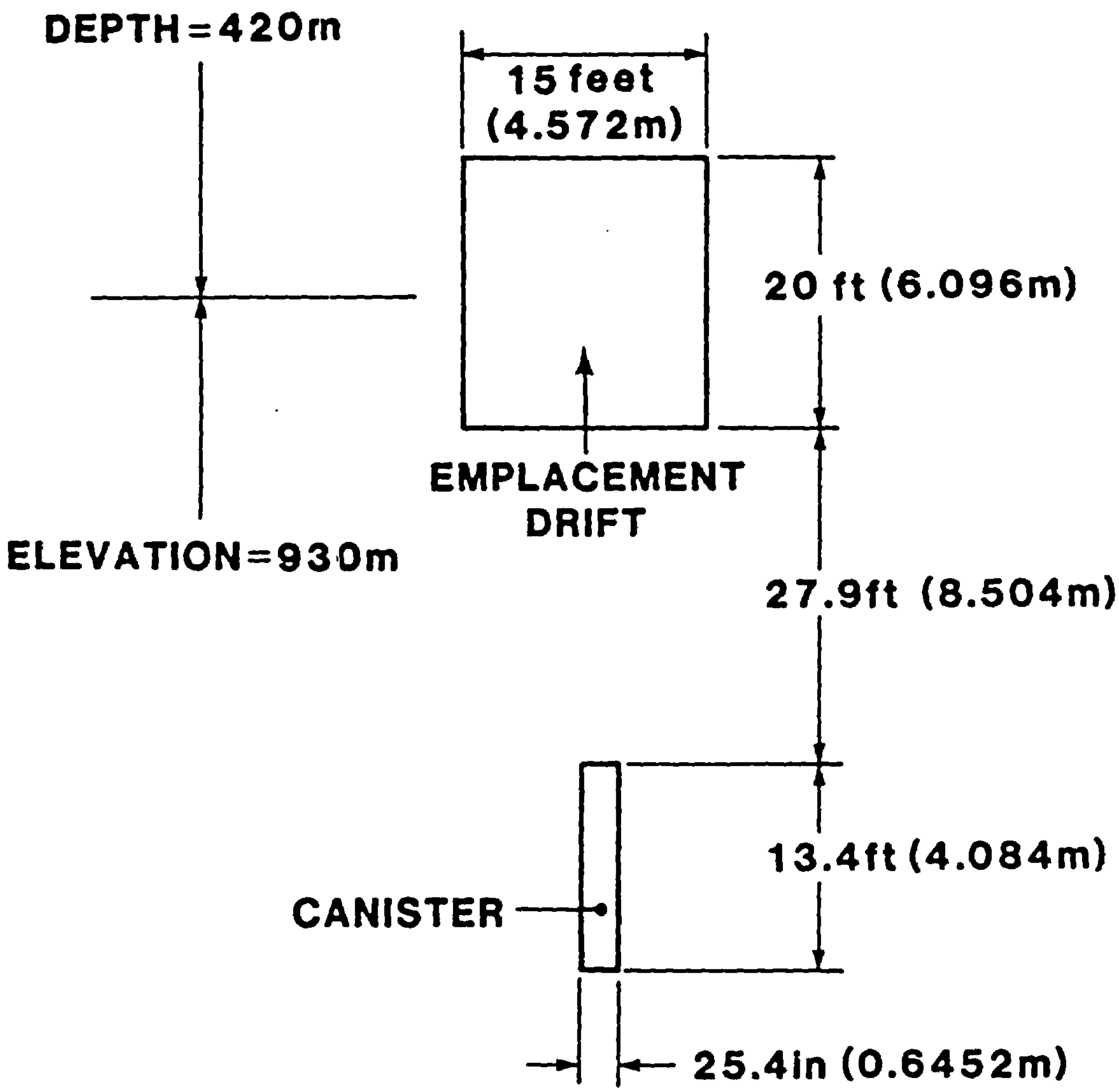

Figure 2b. Cross-Section of the Two-Dimensional Model for Emplacement Scheme 2 showing Dimensions of the Emplacement Drift and Canisters

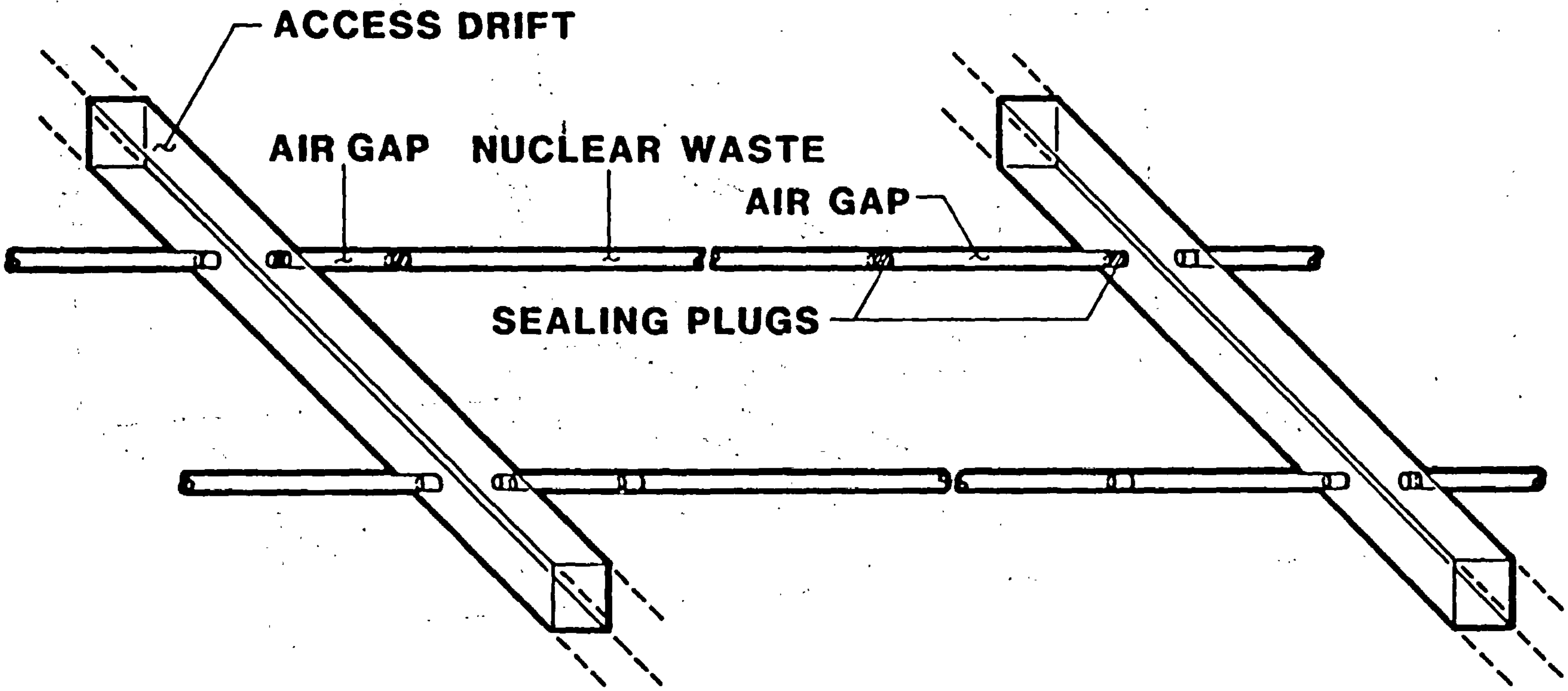

Figure 3. Layout for Emplacement Scheme 3.

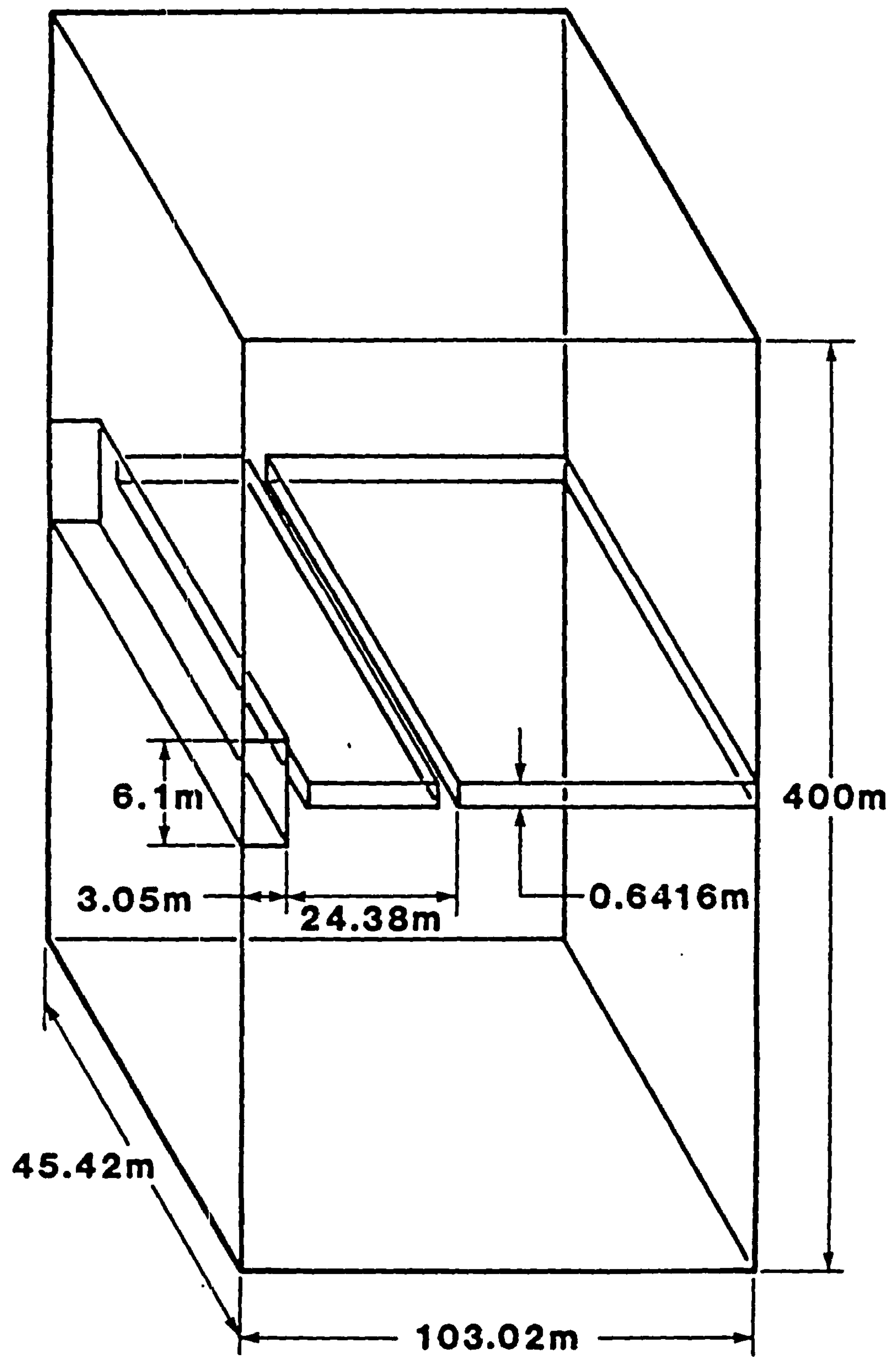

Figure 4. Unit Section of Emplacement Scheme 3 Showing Effective Volume of Canisters and Air Gap

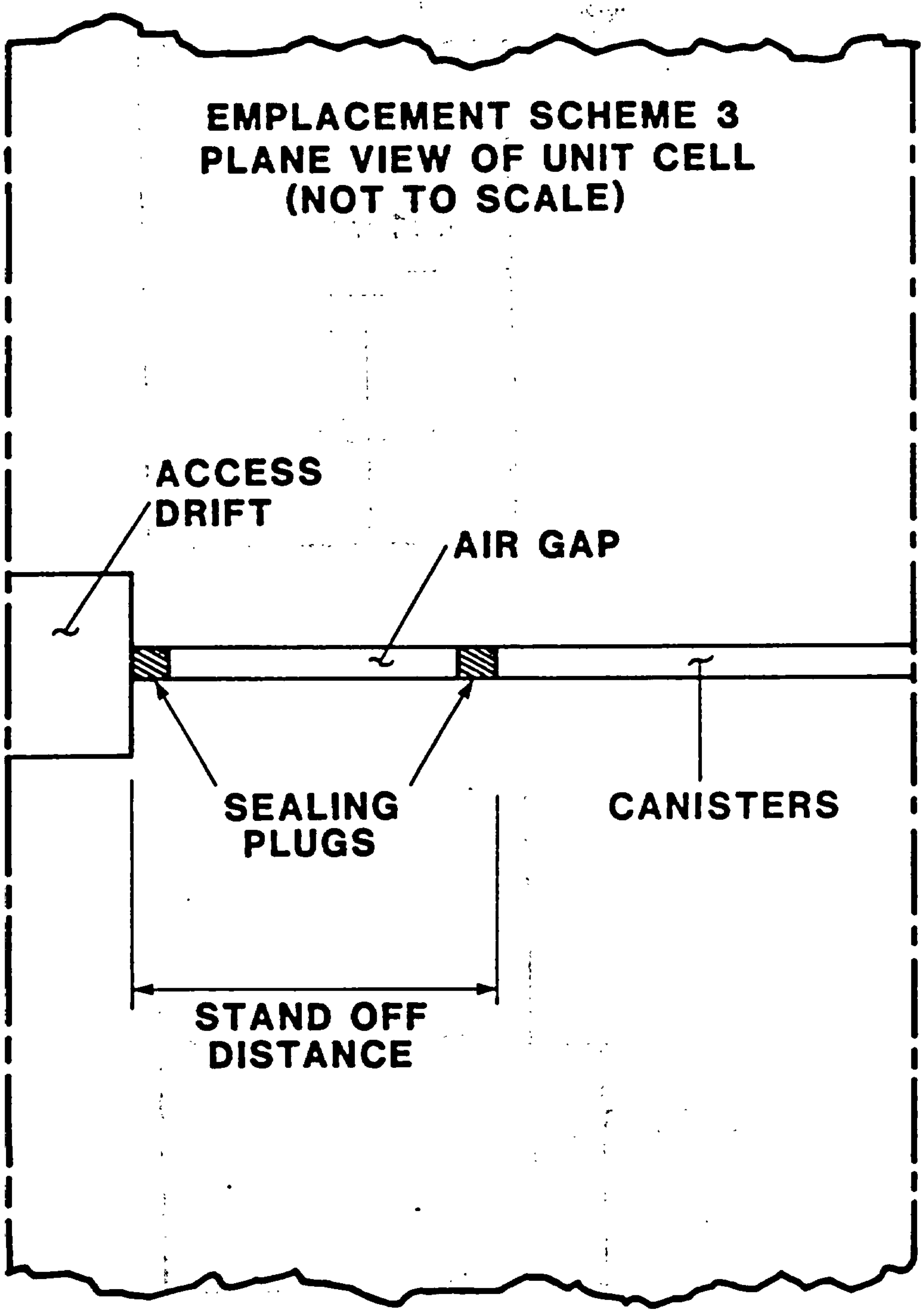

Figure 5. Plane Cross-Section of the Unit Cell for Emplacement Scheme 3

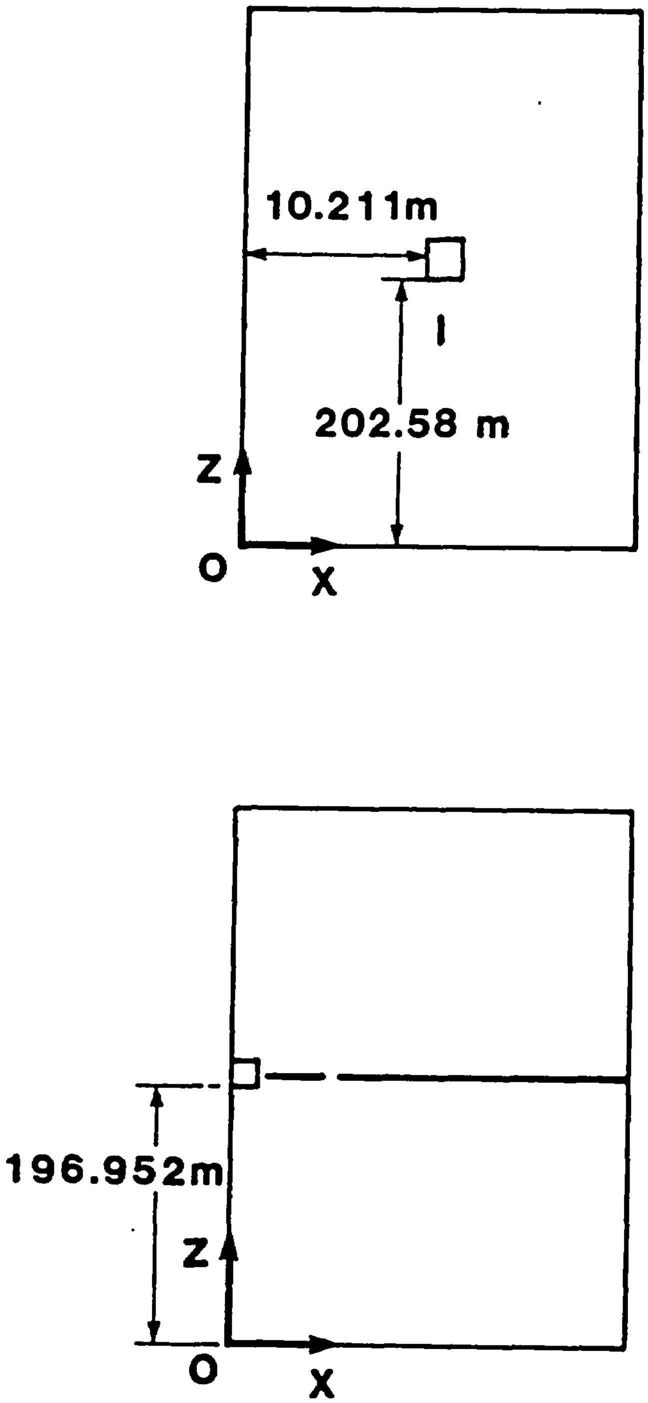

Figure 6. Diagram of the Direction and Origin of the Coordinate Axes for the Two-Dimensional Model (a) Emplacement Scheme 2 (b) Emplacement Scheme 3

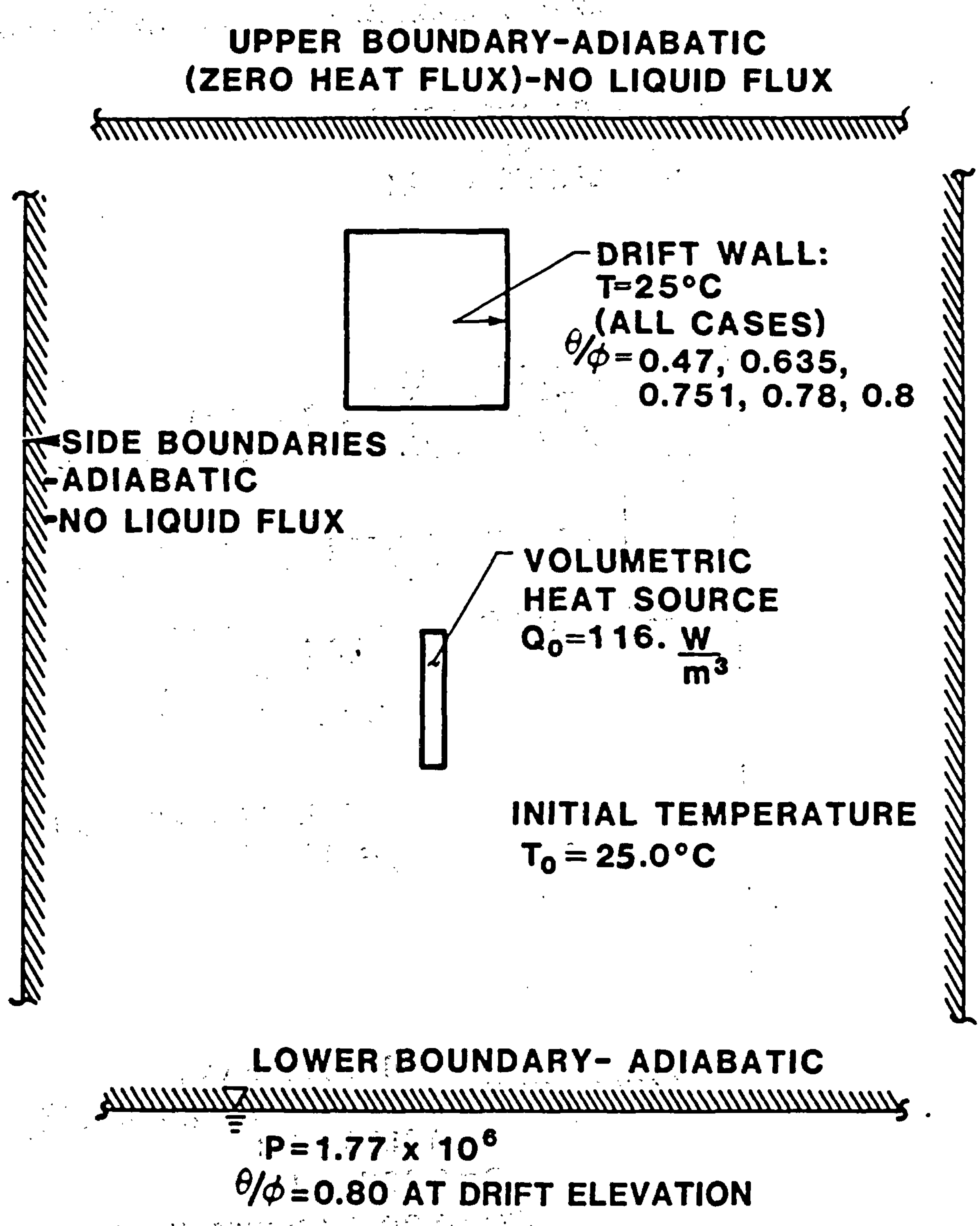

Figure 7. Boundary Conditions used in the SAGUARO Analysis of Emplacement Scheme 2

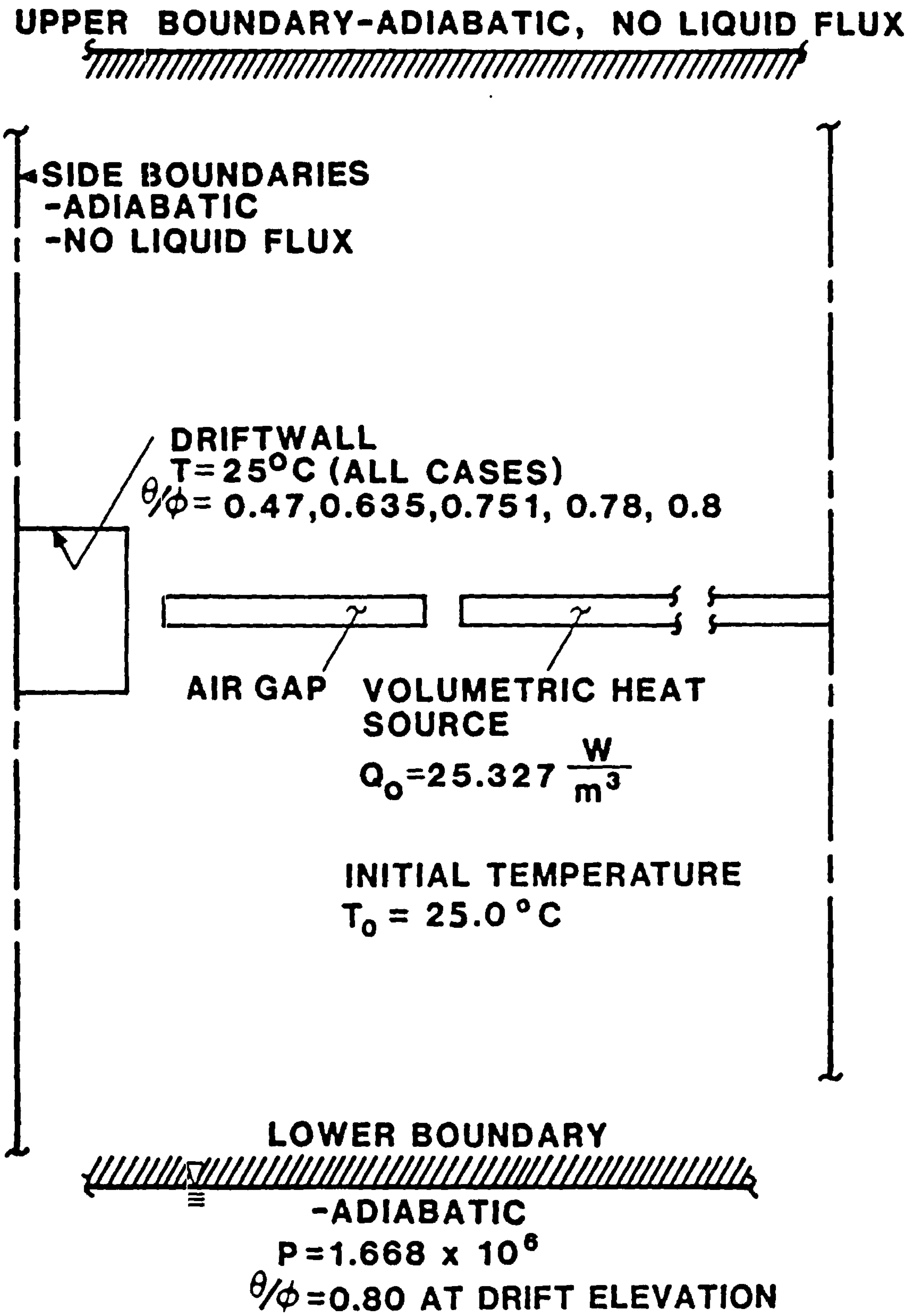

Figure 8. Boundary Conditions used in the SAGUARO Analysis of Emplacement Scheme 3

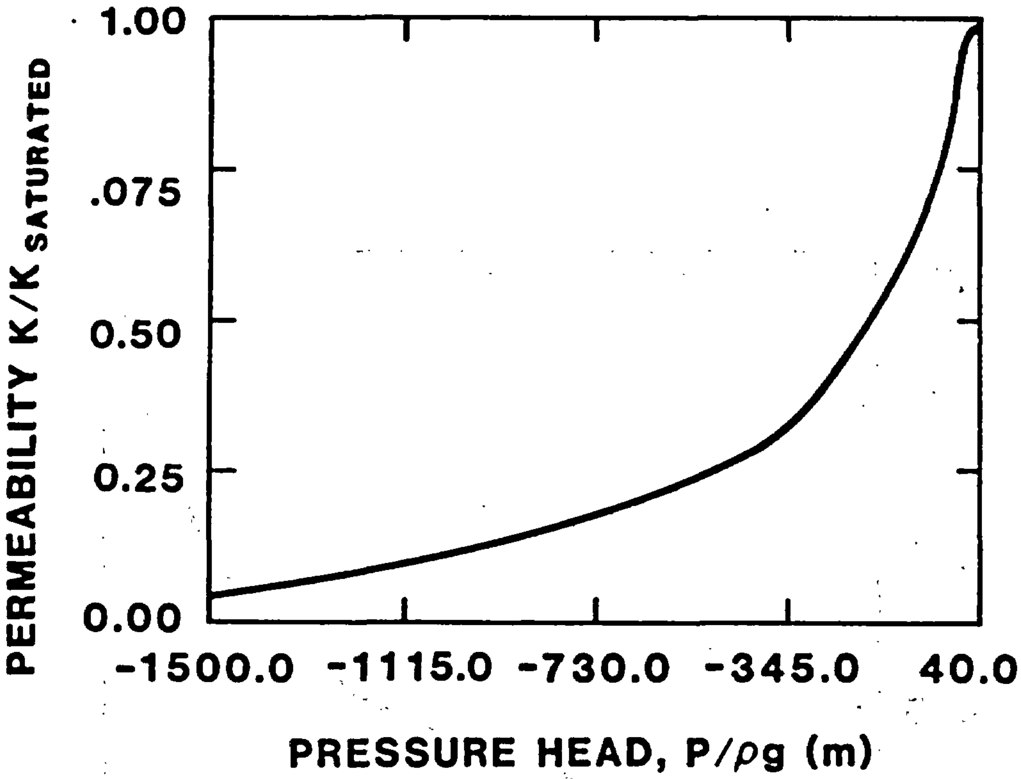

Figure 9. Nondimensional Permeability as a Function of Pressure Head

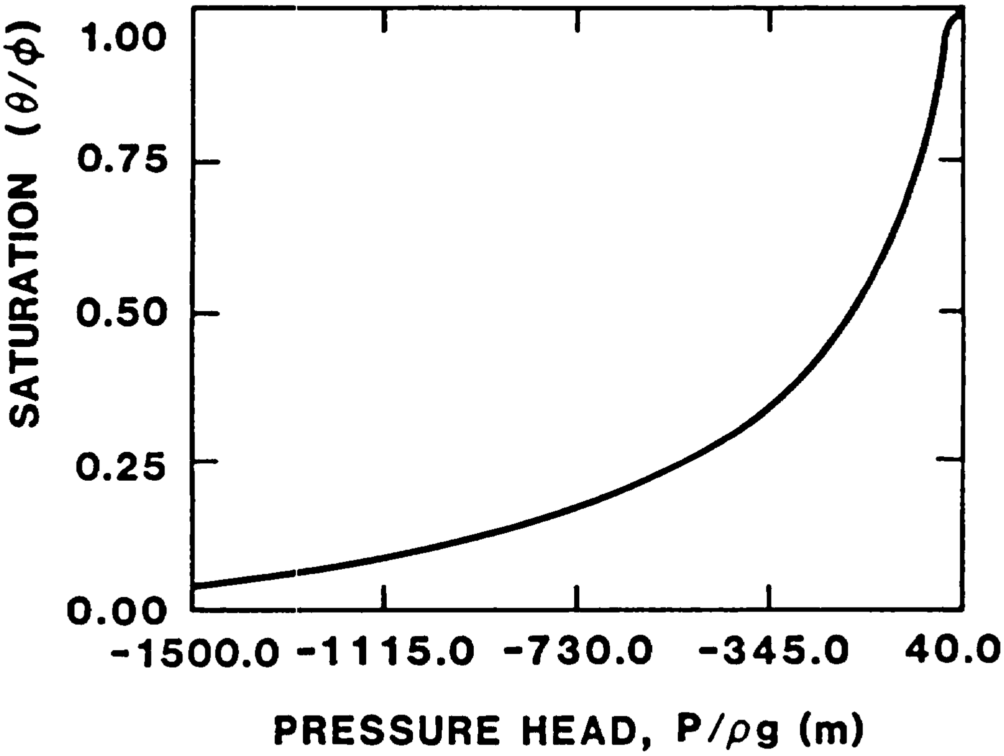

Figure 10. Nondimensional Moisture Content as a Function of Pressure Head

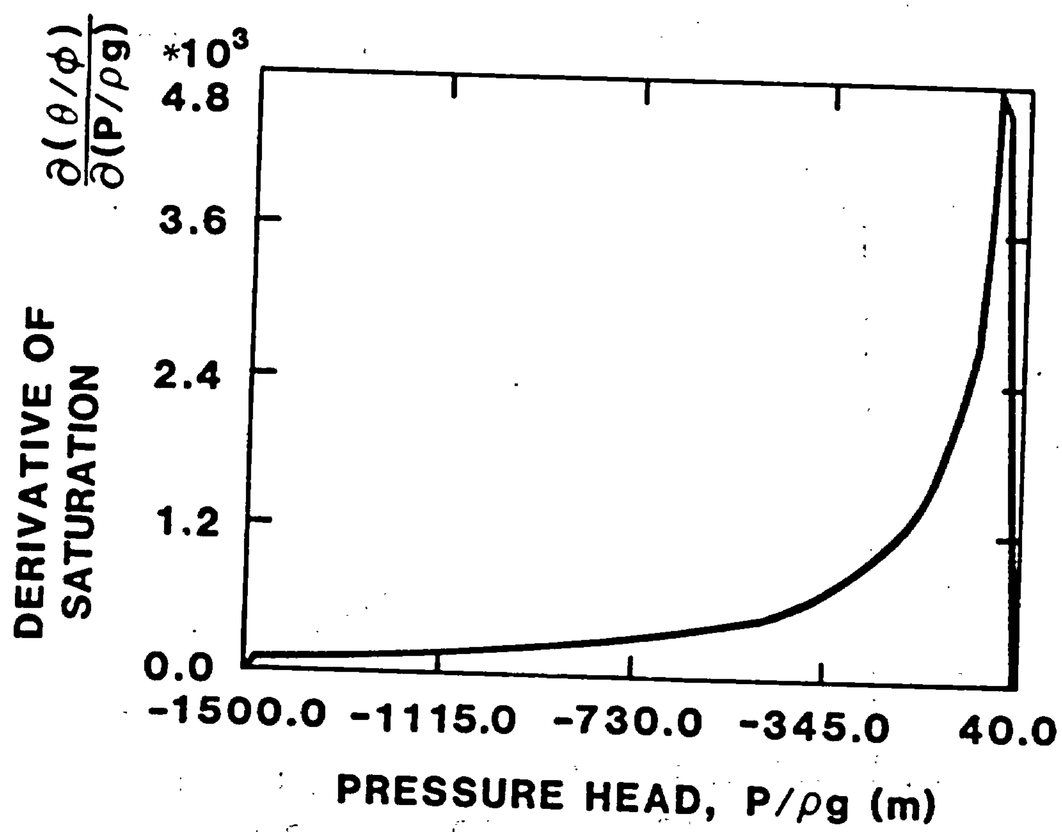

Figure 11. Derivative of Moisture Content with respect to Pressure Head

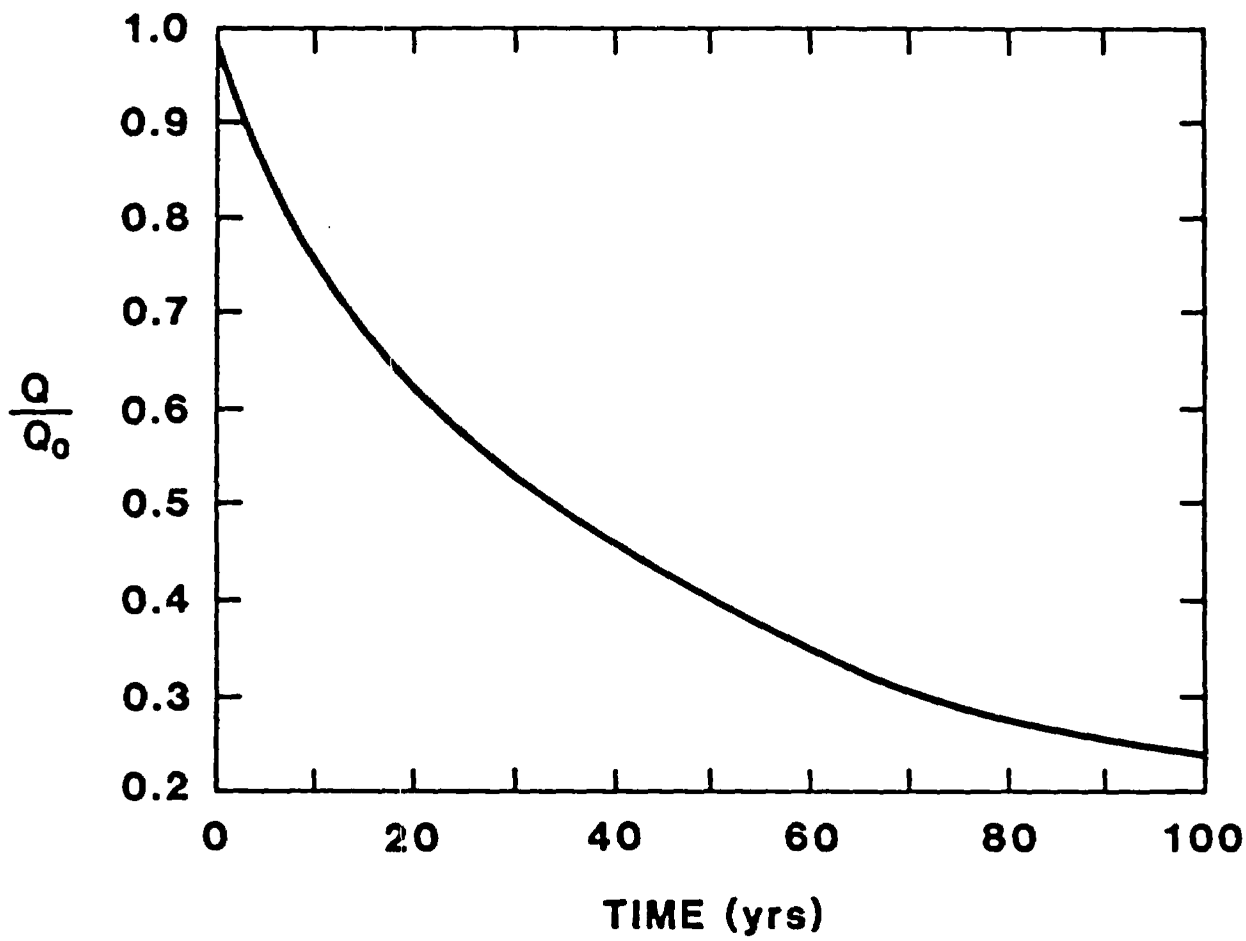

Figure 12. Time History of the Normalized Heat Source

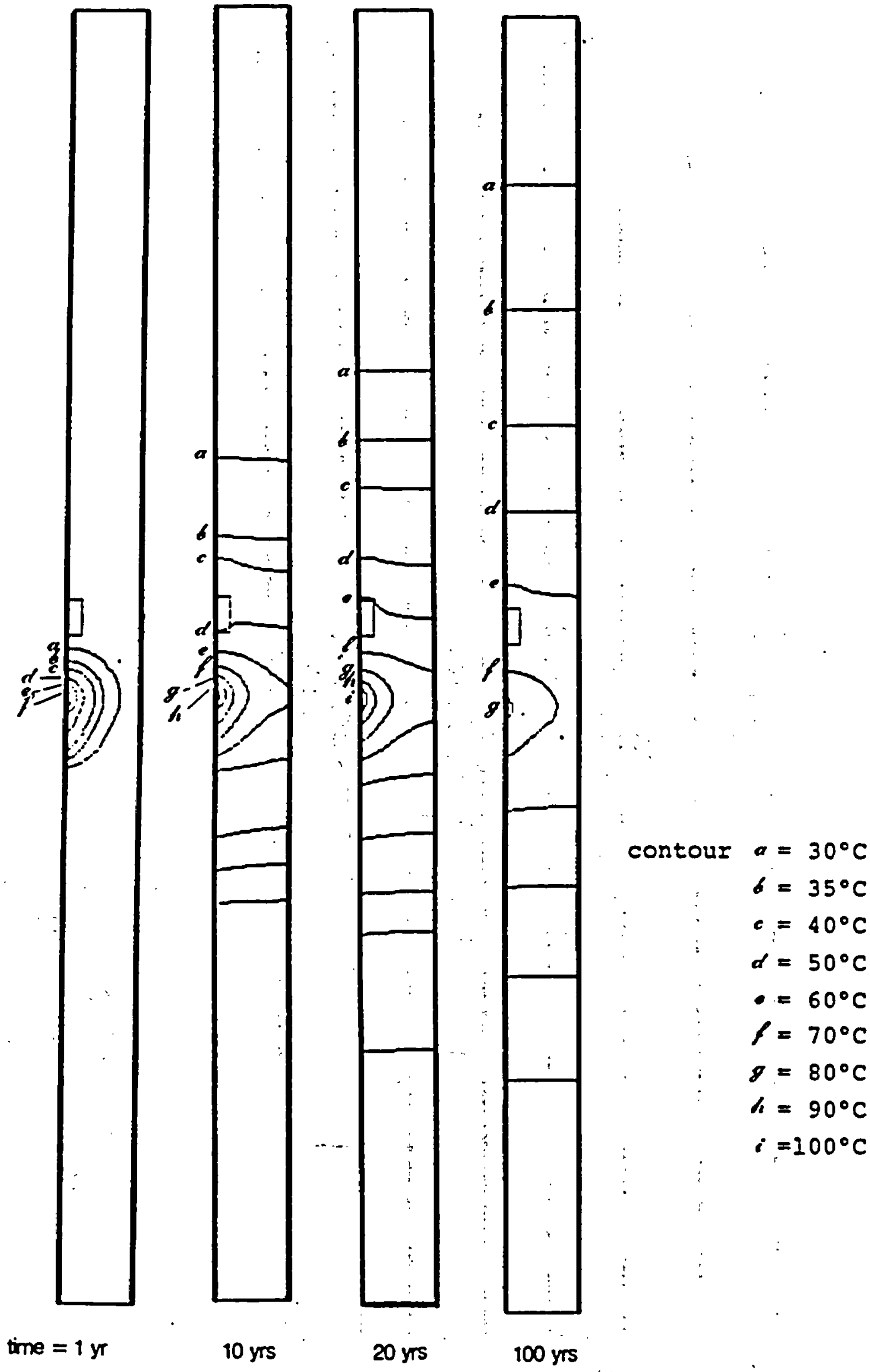

Figure 13. Temperature Contours -- Emplacement Scheme 2
(unventilated drift)

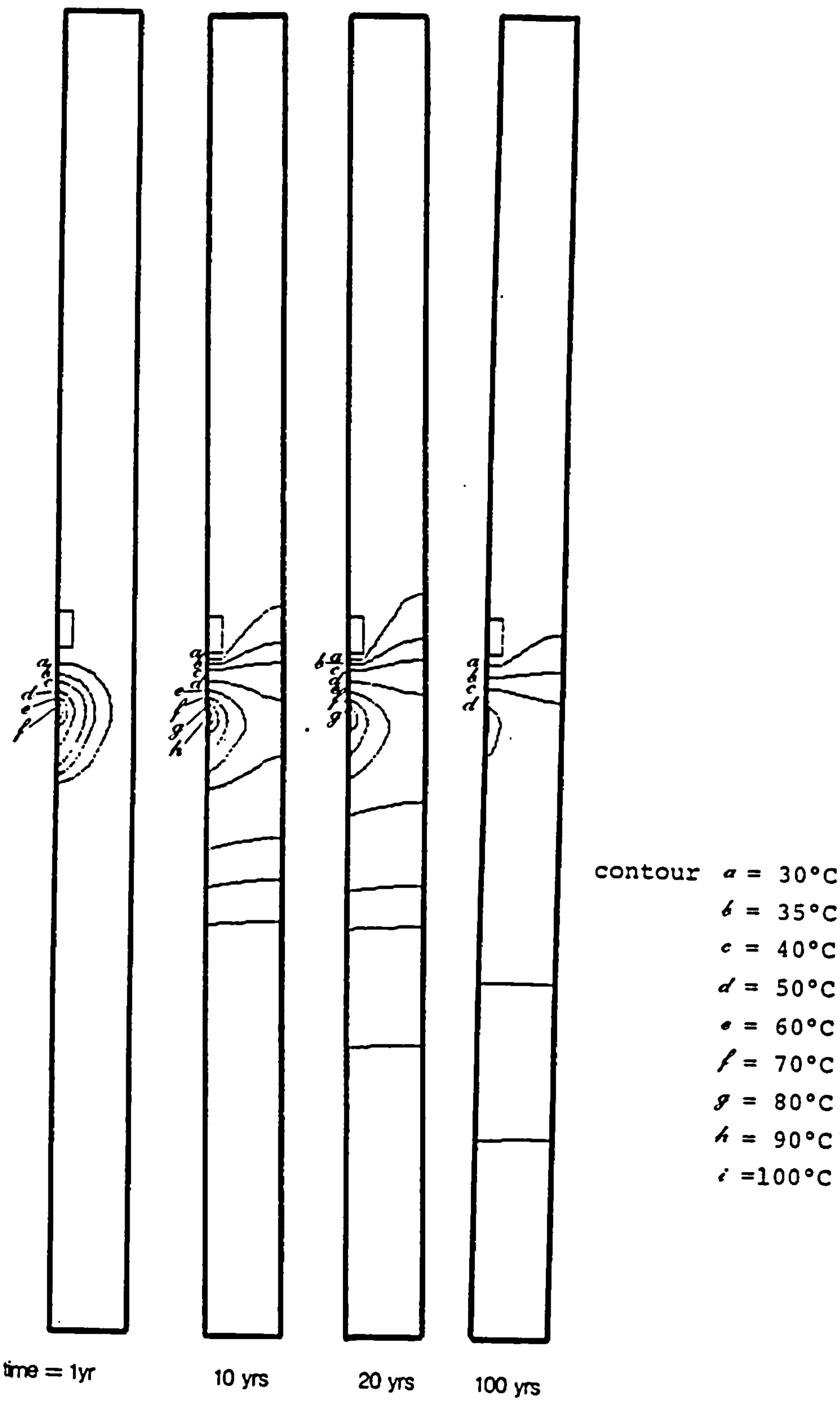

Figure 14. Temperature Contours -- Emplacement Scheme 2 (ventilated, $\theta_{drift}/\phi = 0.80$)

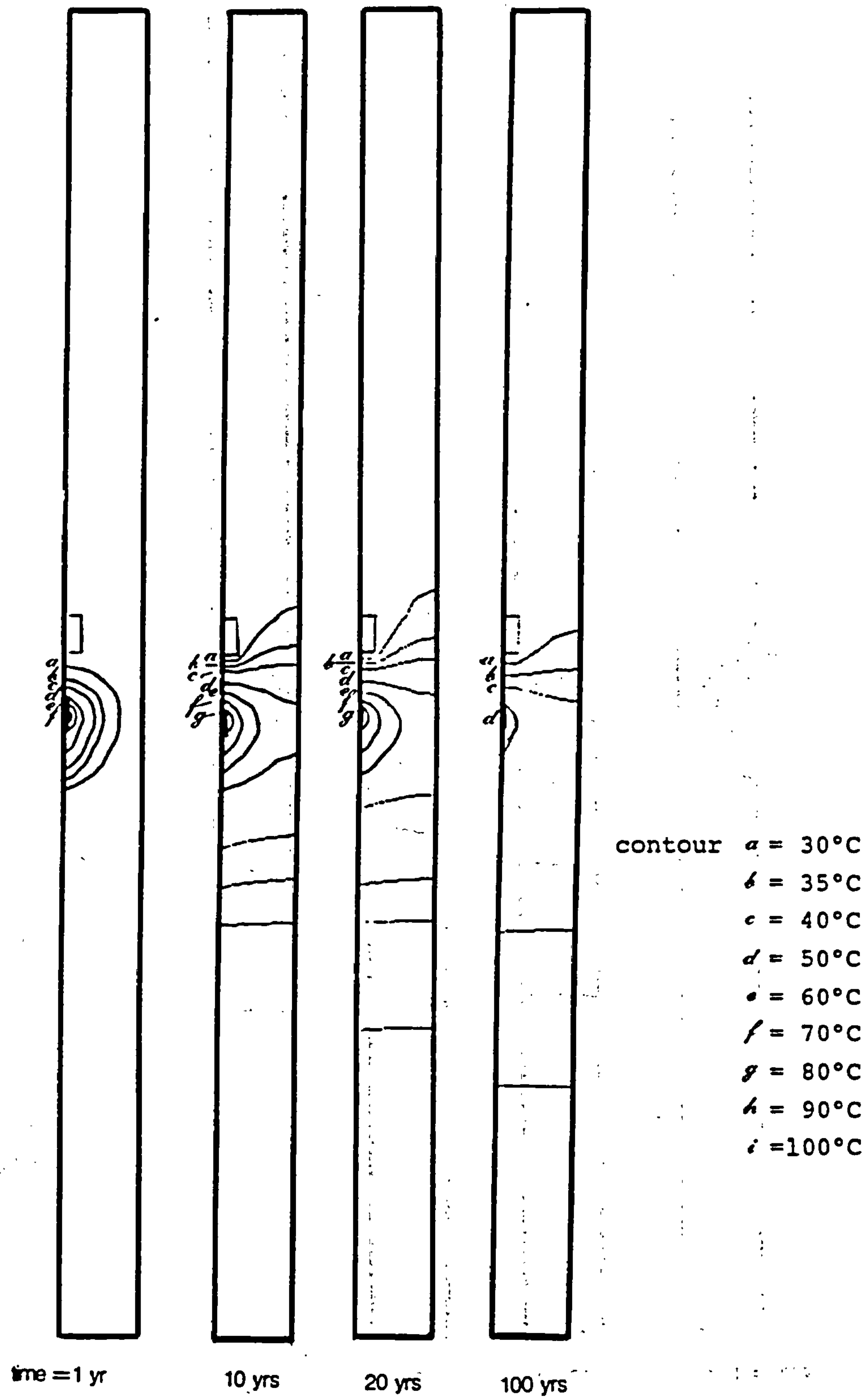

Figure 15. Temperature Contours -- Emplacement Scheme 2 (ventilated, θ_{drift}/ϕ = 0.78)

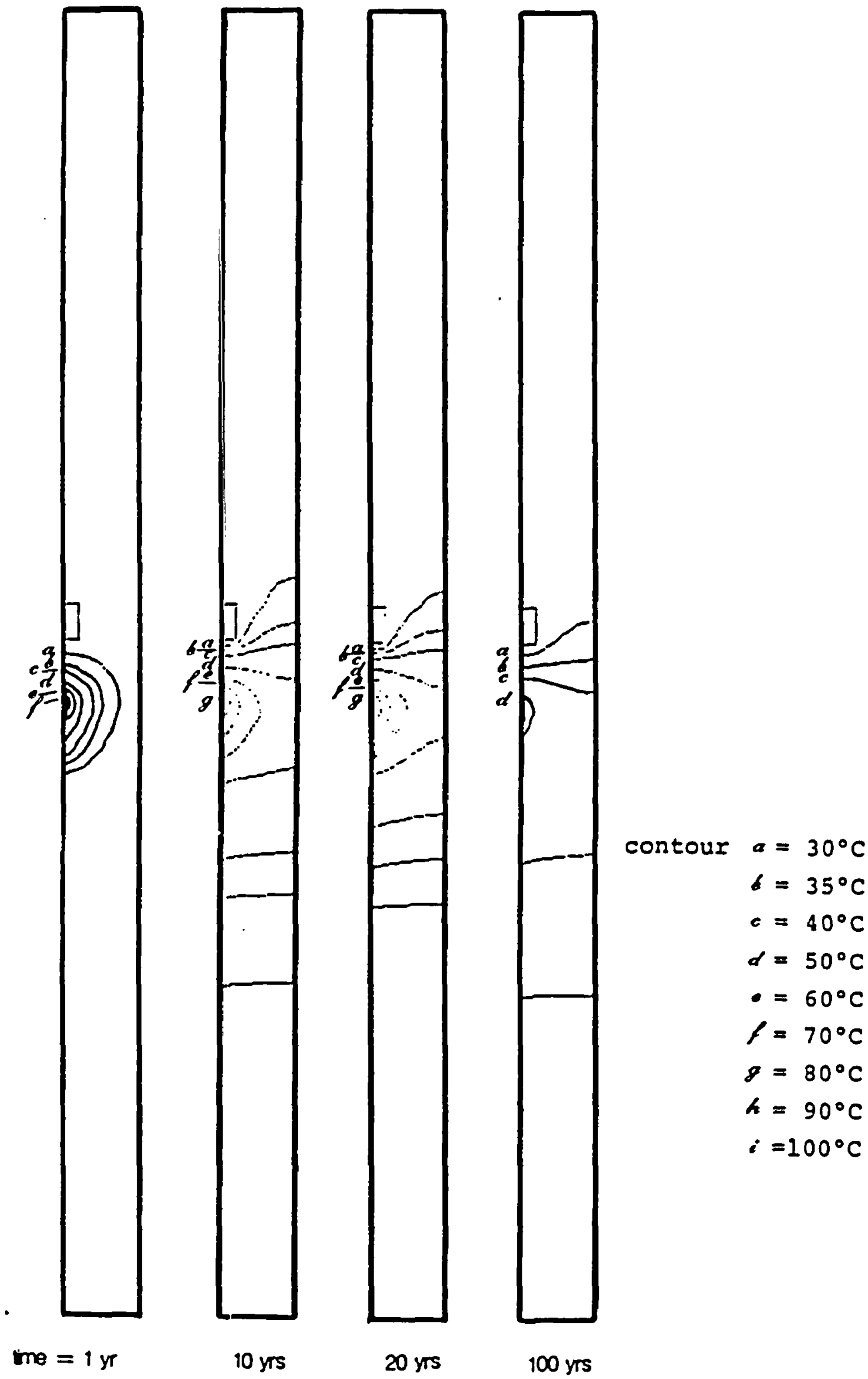

Figure 16. Temperature Contours -- Emplacement Scheme 2 (ventilated, θ_{drift}/ϕ = 0.751)

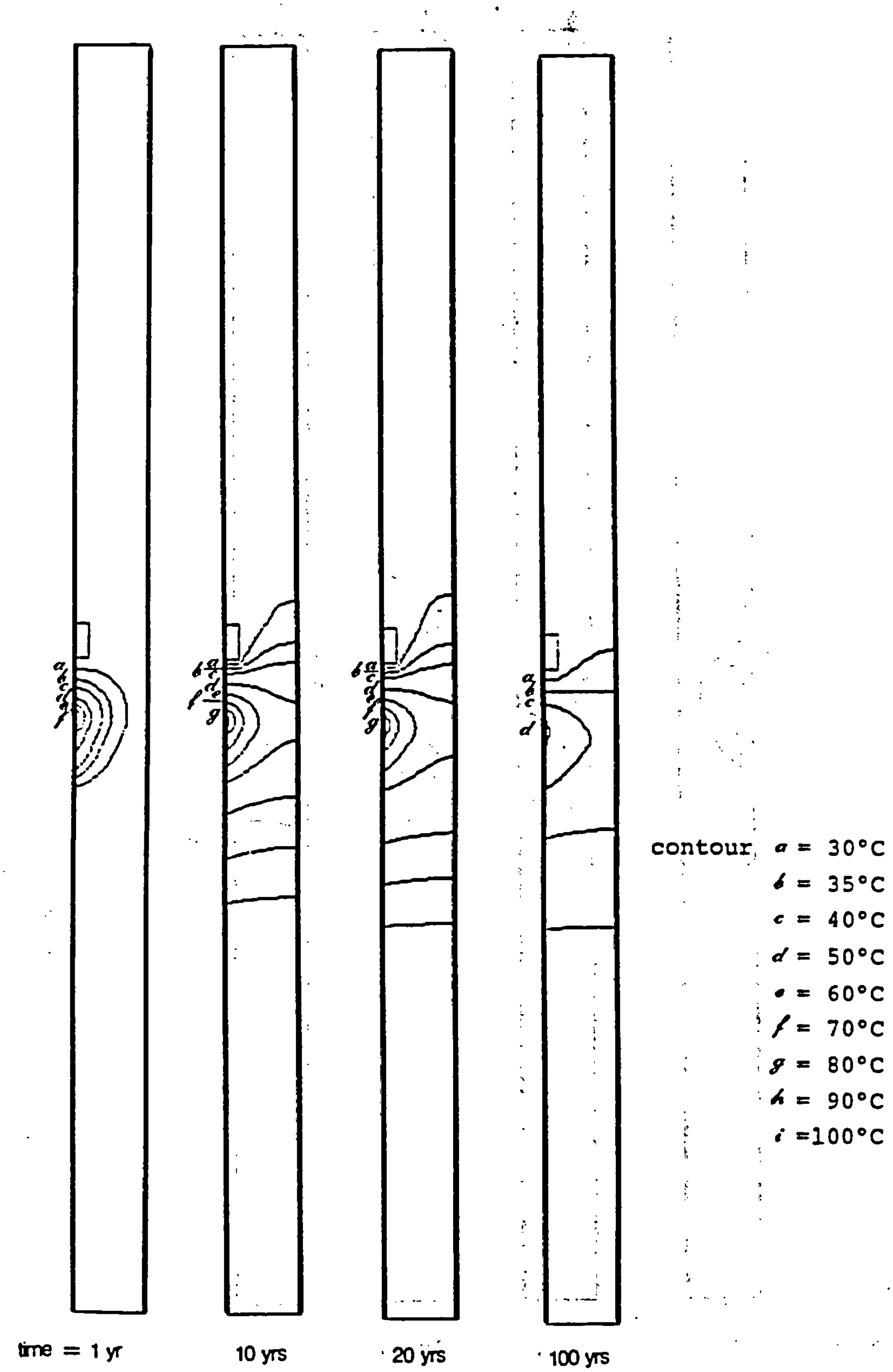

Figure 17. Temperature Contours -- Emplacement Scheme 2 (ventilated, $\theta_{drift}/\phi = 0.635$)

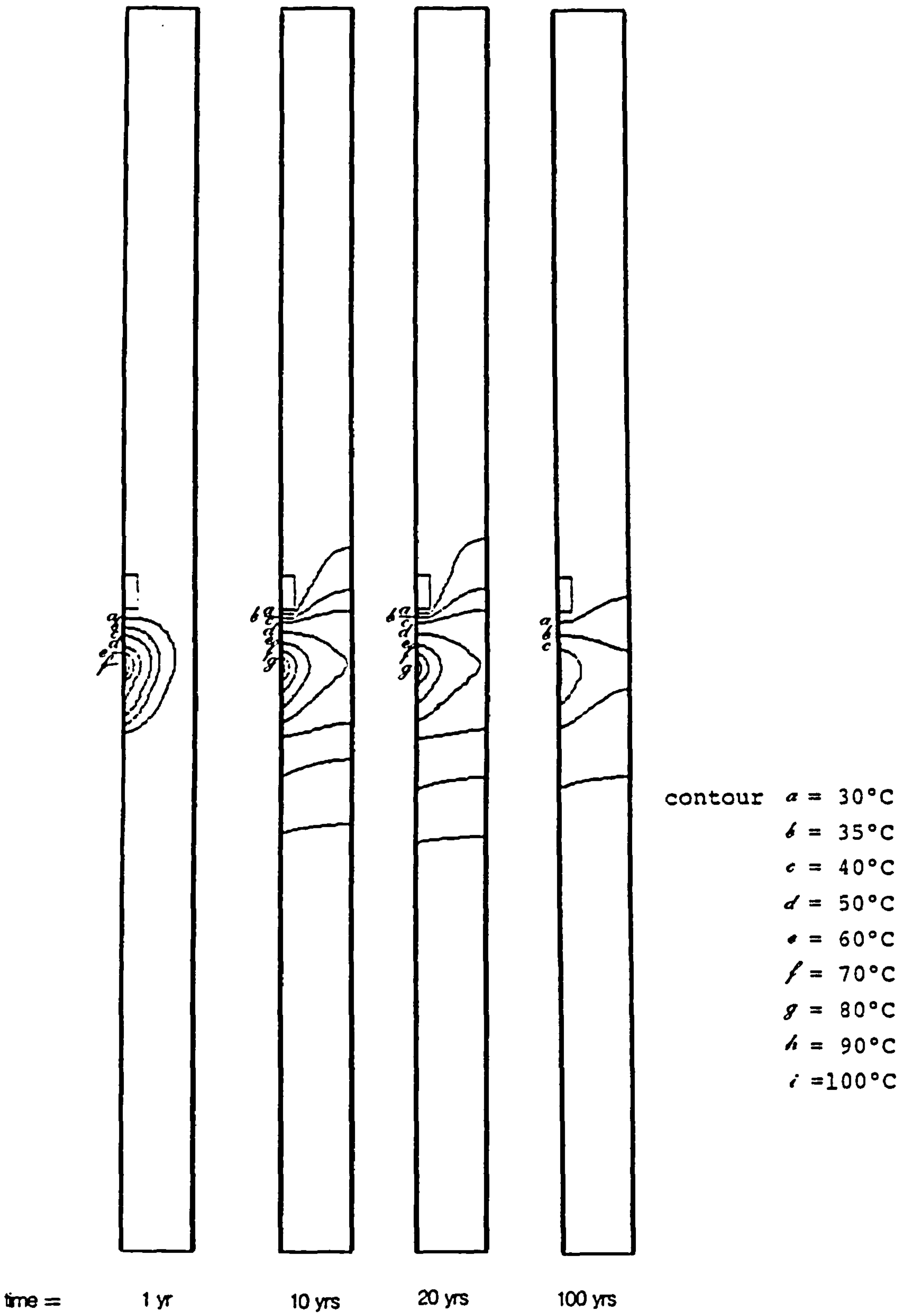

Figure 18. Temperature Contours -- Emplacement Scheme 2
(ventilated, θ_{drift}/ϕ = 0.47)

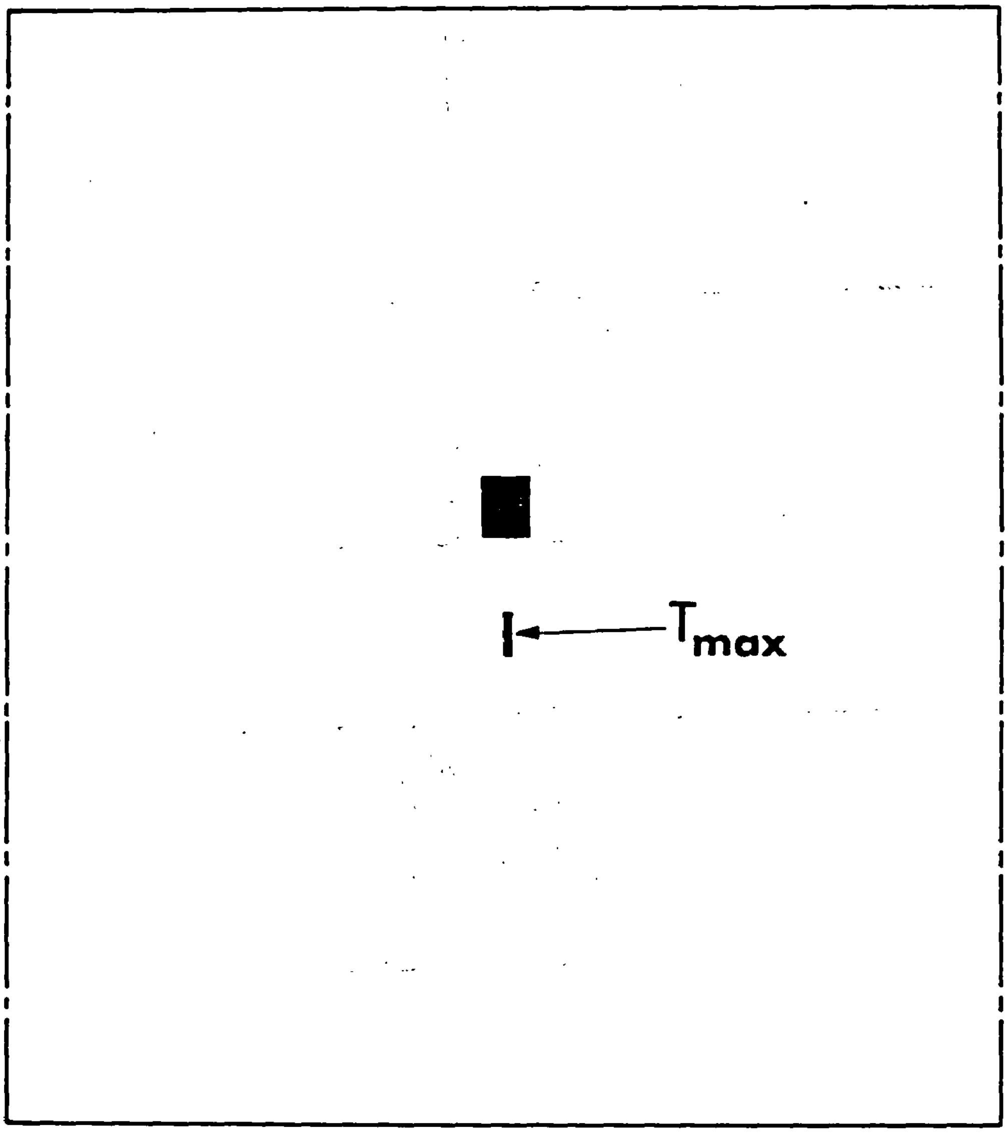

Figure 19. Location of the Maximum Temperaures for Emplacement Scheme 2 (t = 10 years)

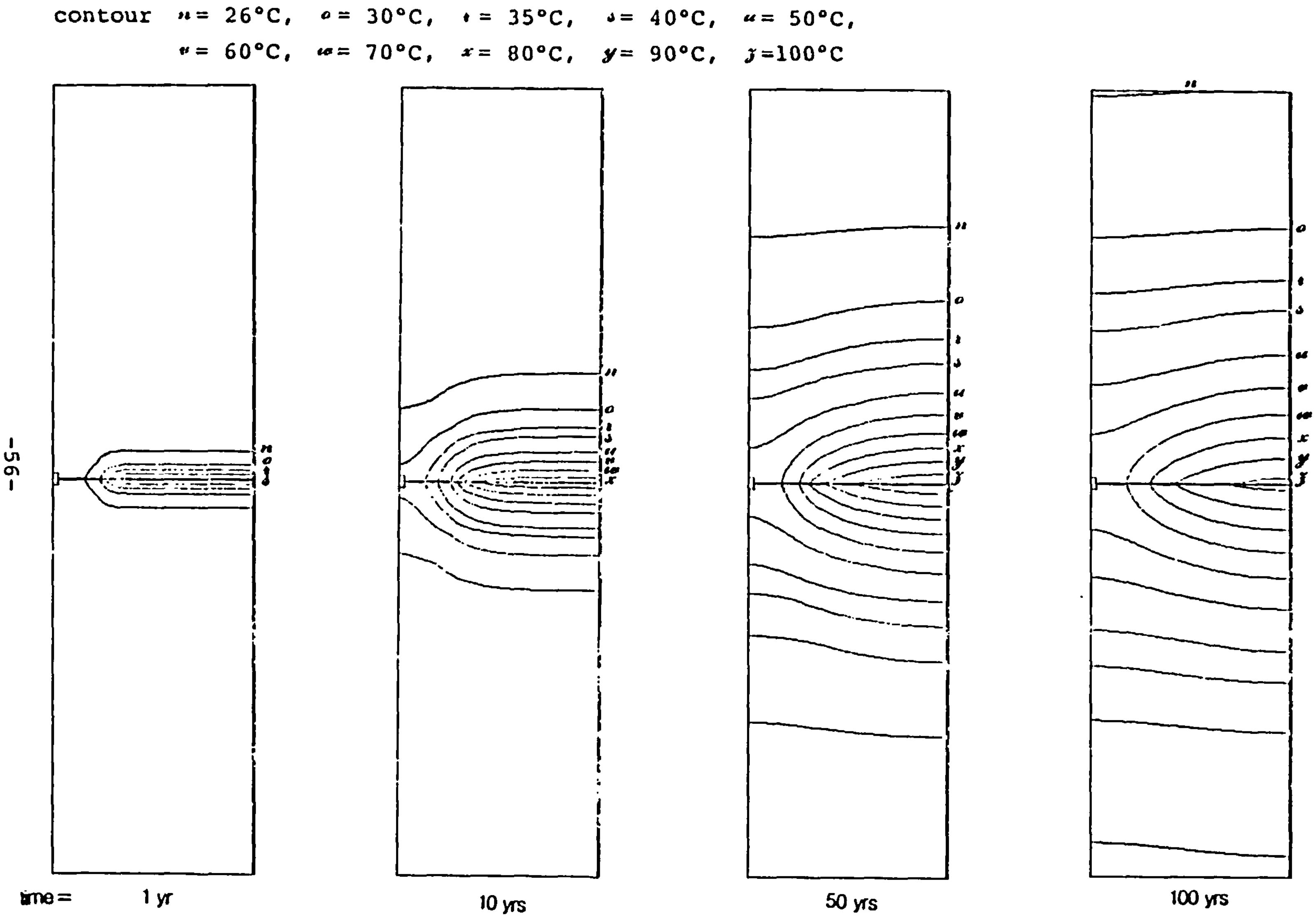

Figure 20. Temperature Contours -- Emplacement Scheme 3
(unventilated drift)

contour n = 26°C, o = 30°C, t = 35°C, s = 40°C, u = 50°C,
v = 60°C, w = 70°C, x = 80°C, y = 90°C, z = 100°C

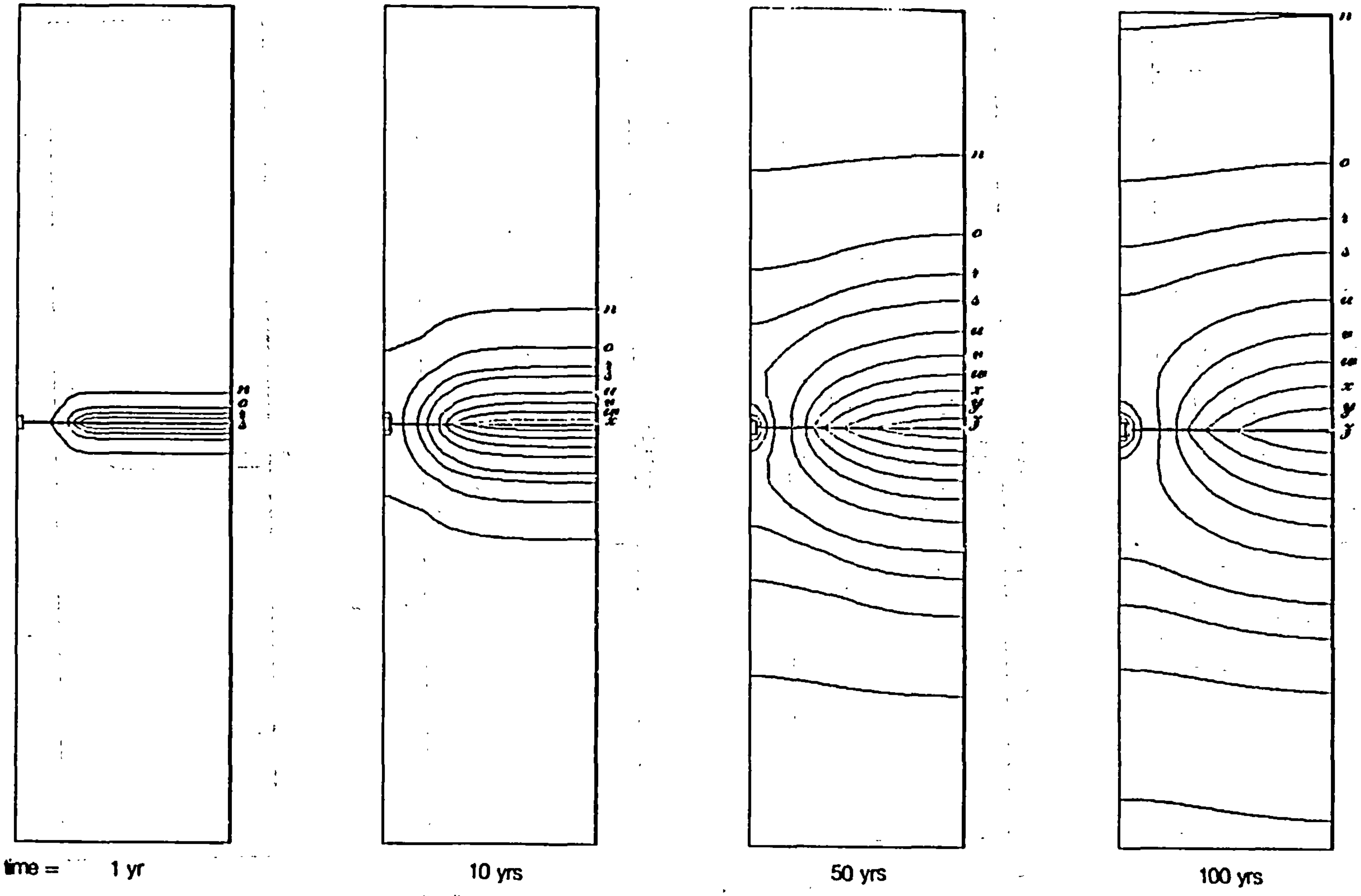

Figure 21. Temperature Contours -- Emplacement Scheme 3
(ventilated, $\theta_{drift}/\phi = 0.80$)

contour n = 26°C, o = 30°C, t = 35°C, s = 40°C, u = 50°C,
v = 60°C, w = 70°C, x = 80°C, y = 90°C, z = 100°C

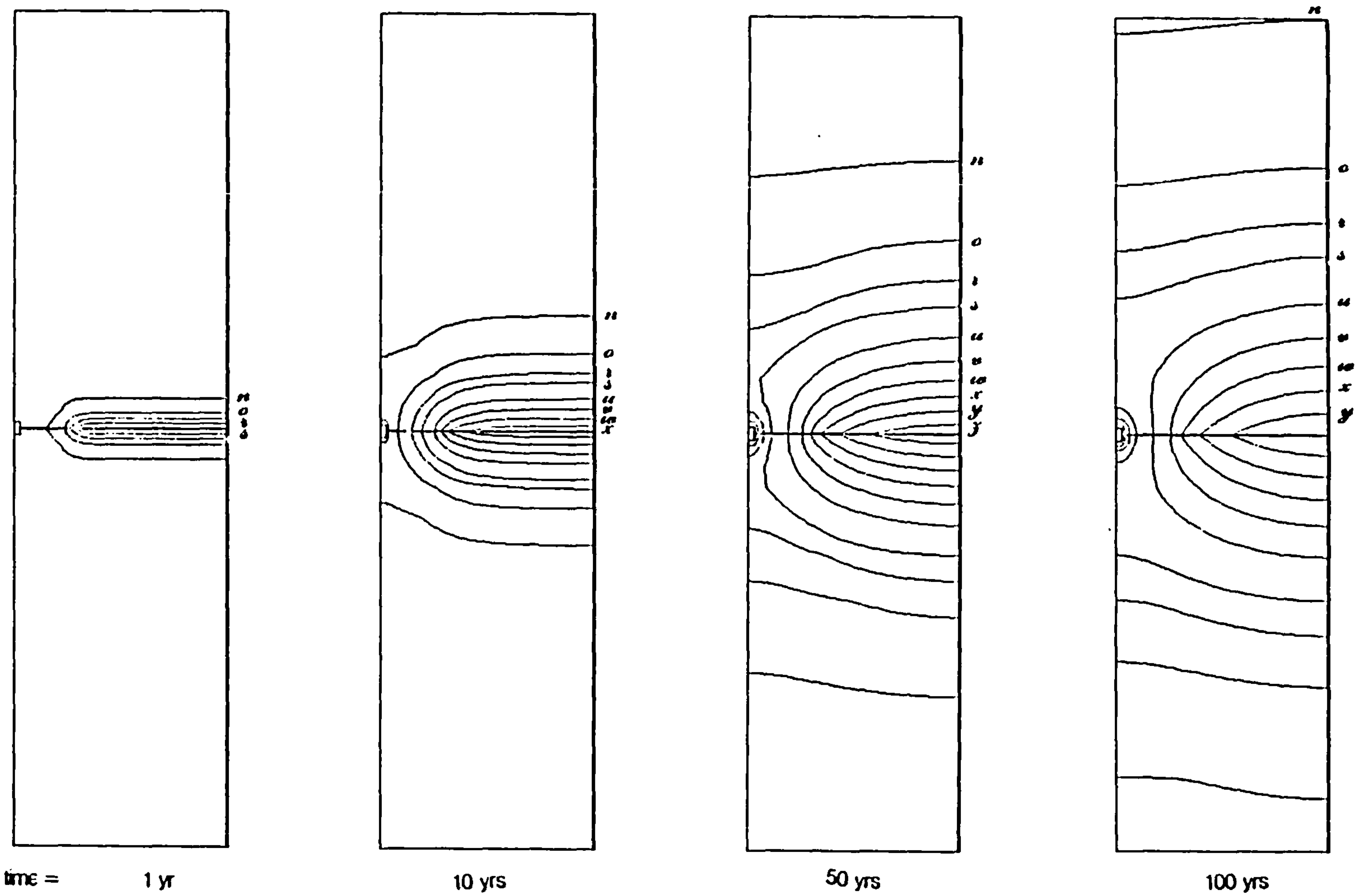

Figure 22. Temperature Contours -- Emplacement Scheme 3
(ventilated, θ_{drift}/ϕ = 0.78)

contour n= 26°C, o= 30°C, t= 35°C, s= 40°C, u= 50°C,
v= 60°C, w= 70°C, x= 80°C, y= 90°C, z=100°C

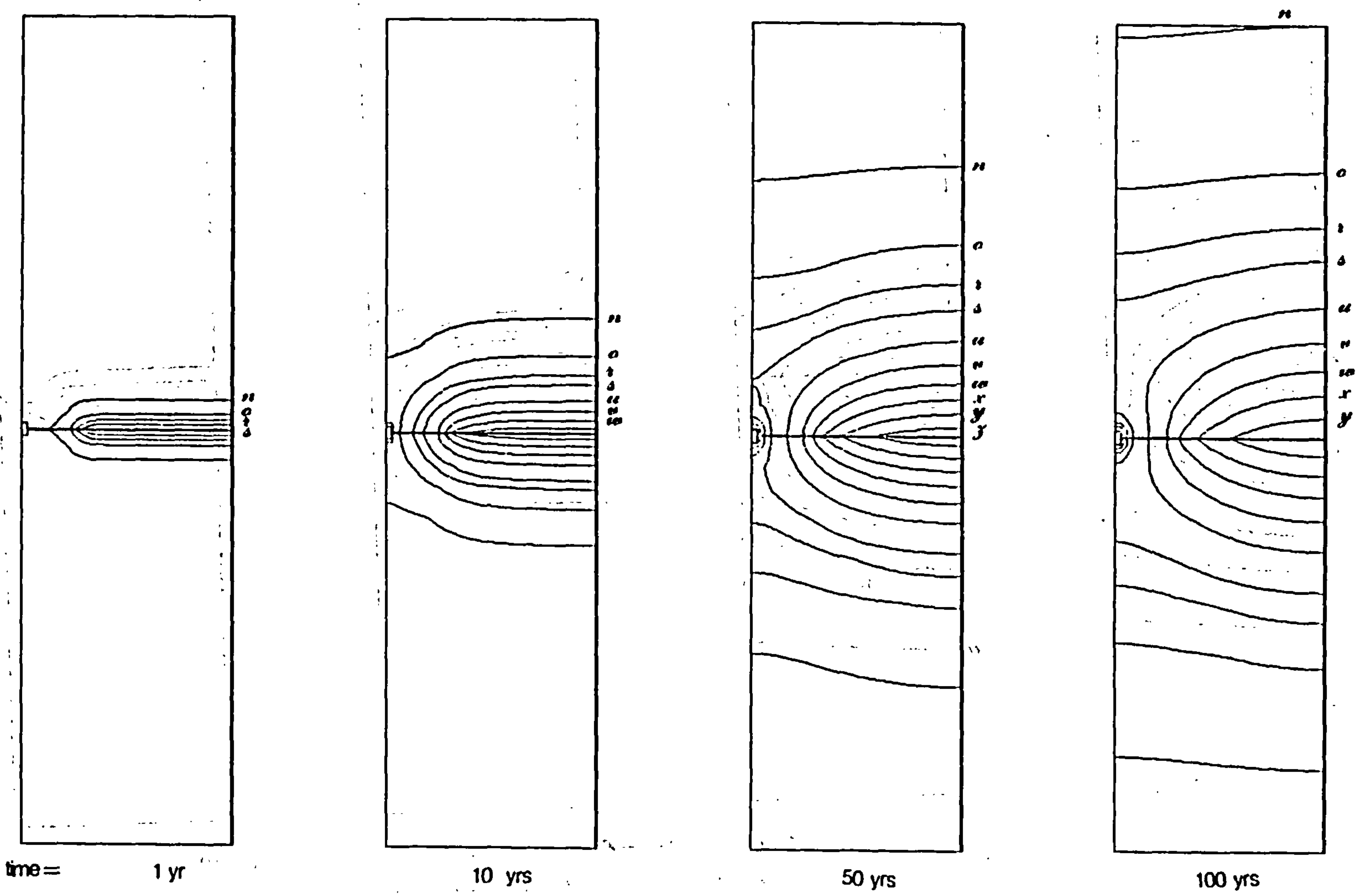

Figure 23. Temperature Contours -- Emplacement Scheme 3
(ventilated, θ_{drift}/ϕ = 0.751)

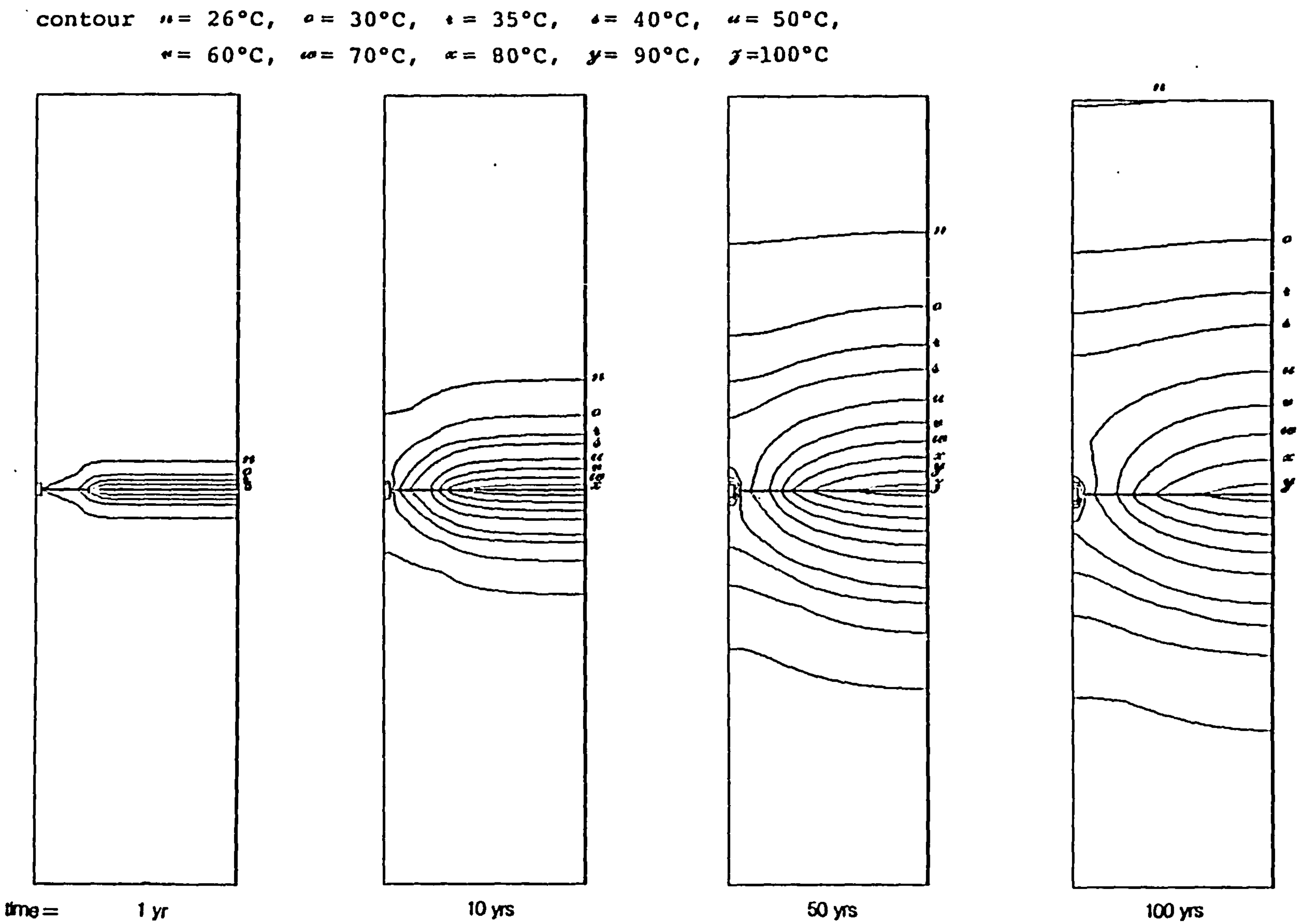

Figure 24. Temperature Contours -- Emplacement Scheme 3
(ventilated, $\theta_{drift}/\phi = 0.635$)

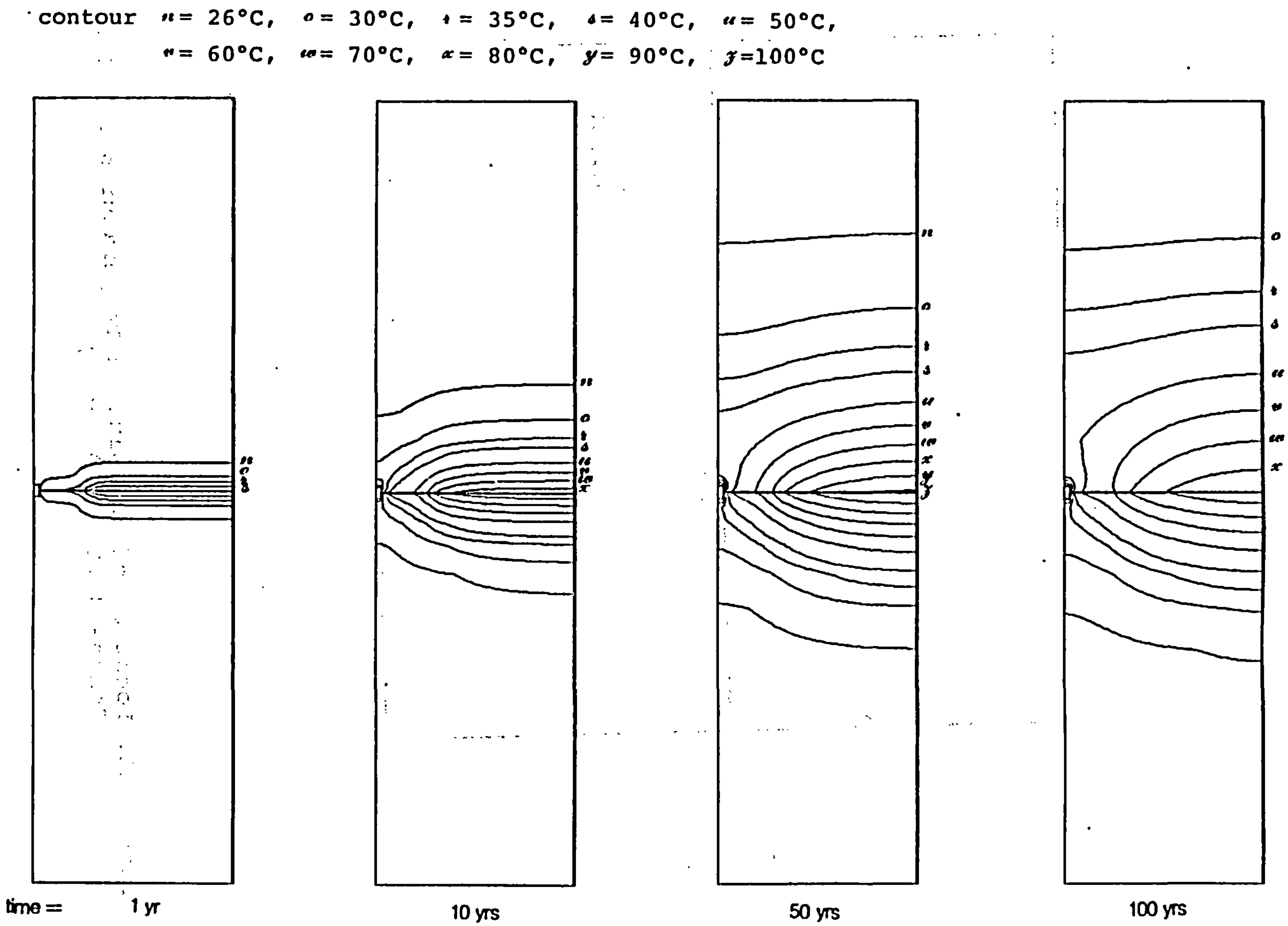

Figure 25. Temperature Contours -- Emplacement Scheme 3
(ventilated, $\theta_{drift}/\phi = 0.47$)

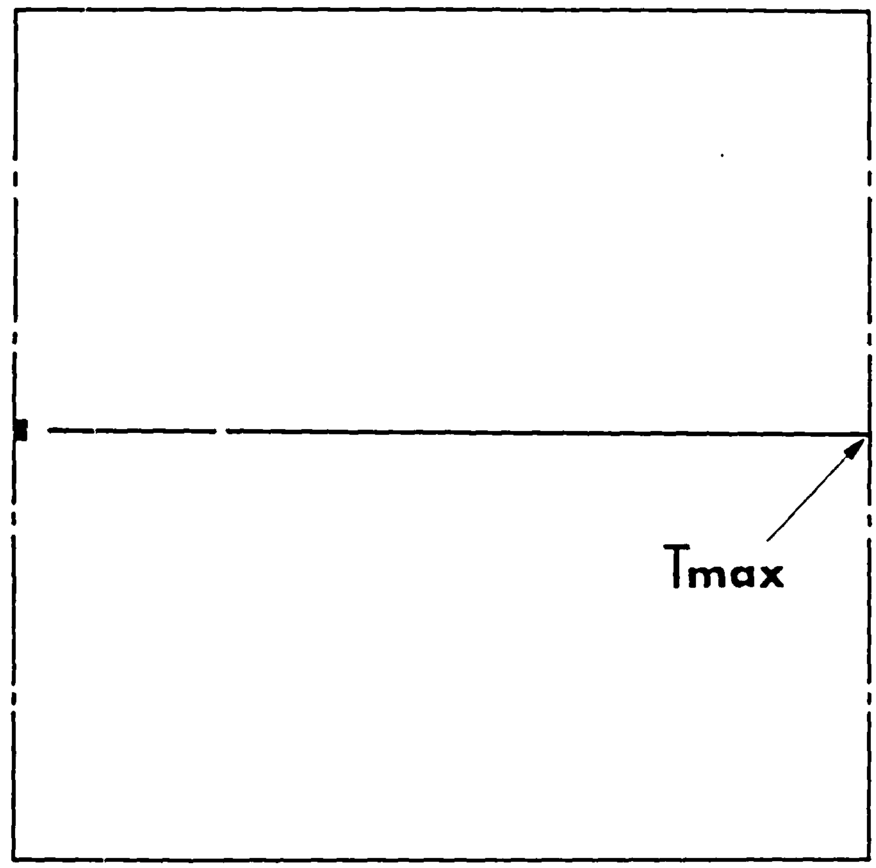

Figure 26. Location of the Maximum Temperatures for Emplacement Scheme 3 (t = 100 years)

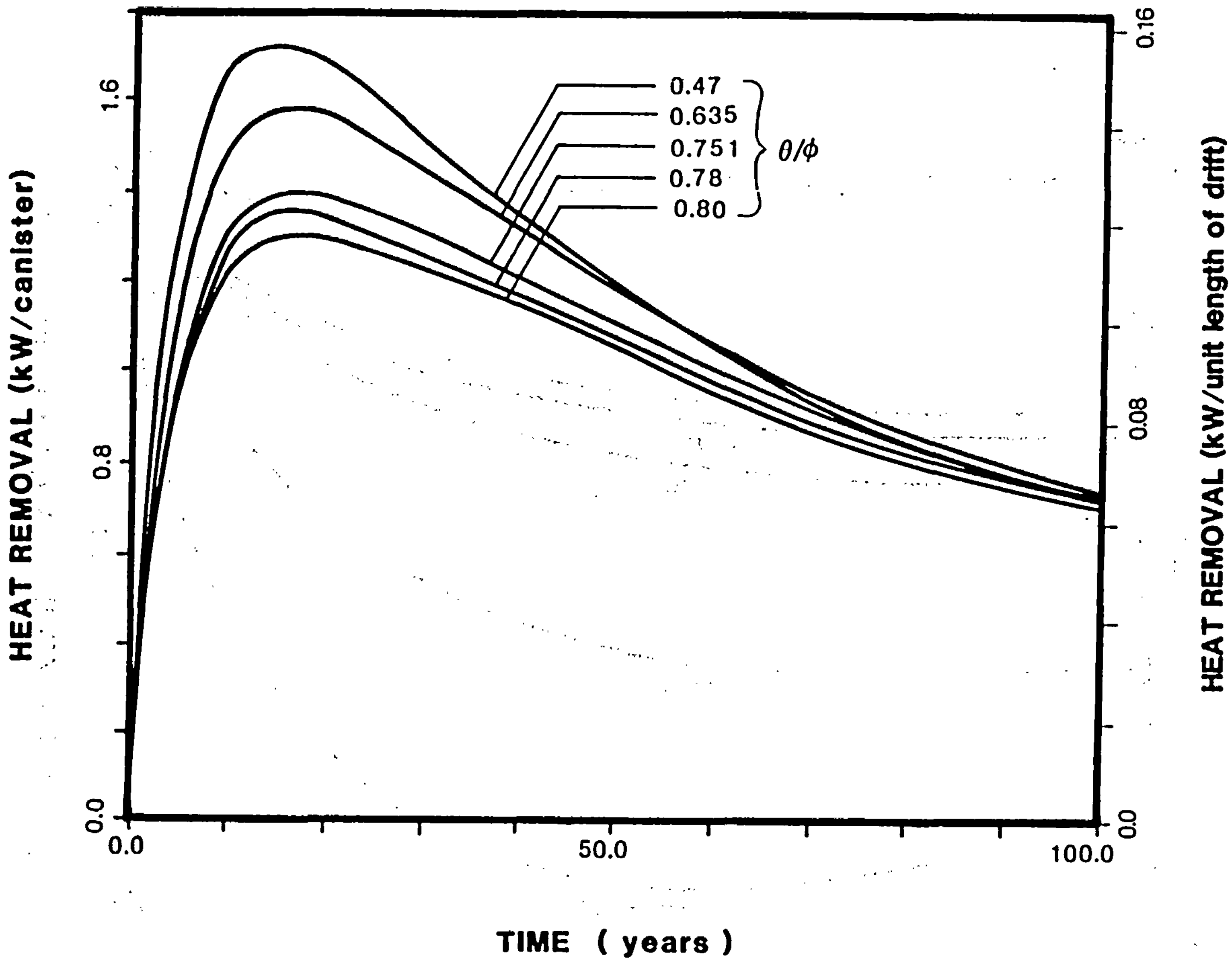

Figure 27. Heat Removal from Emplacement Scheme 2 as a Function of Moisture Content at the Drift Wall

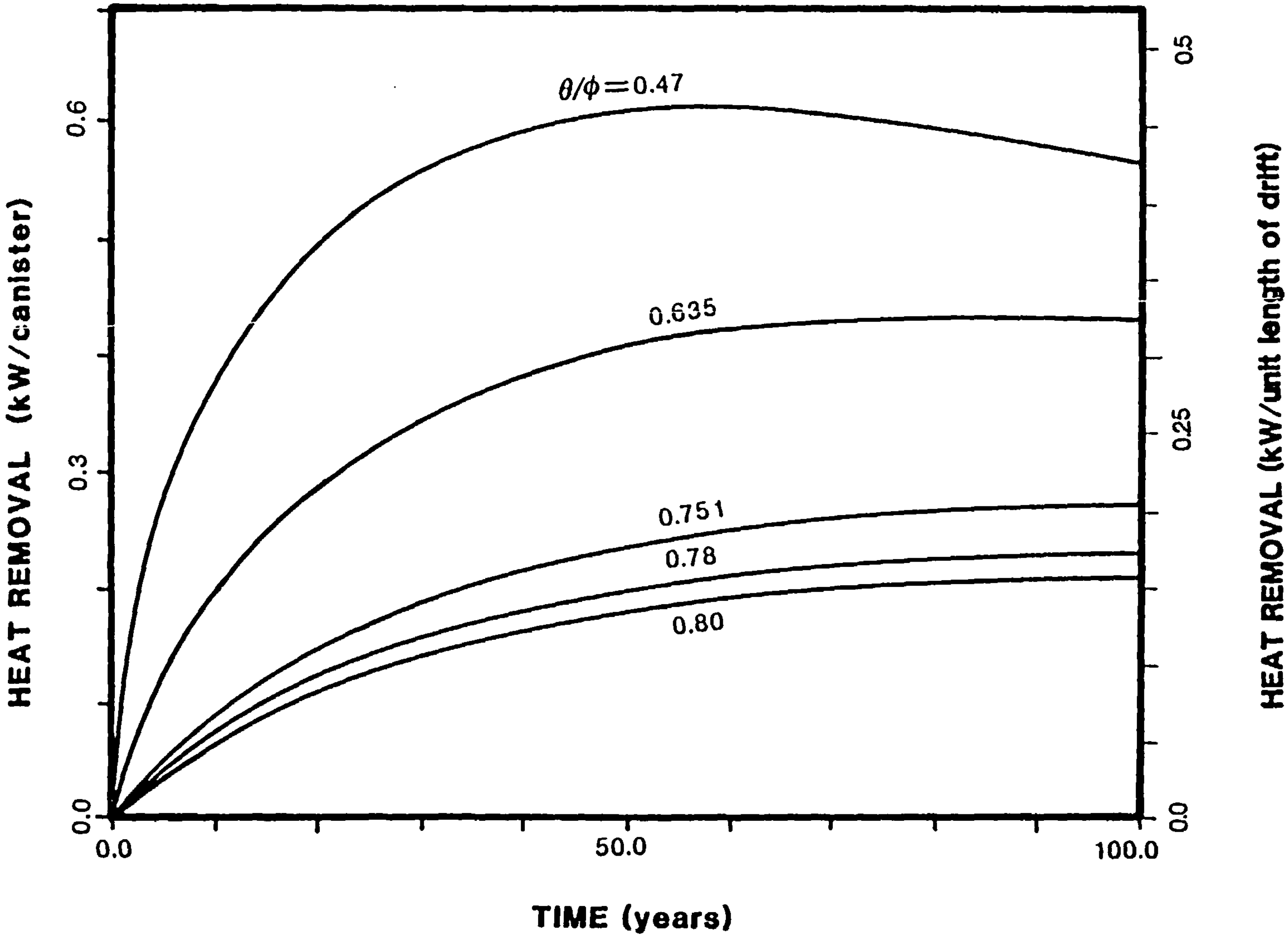

Figure 28. Heat Removal from Emplacement Scheme 3 as a Function of Moisture Content at the Drift Wall

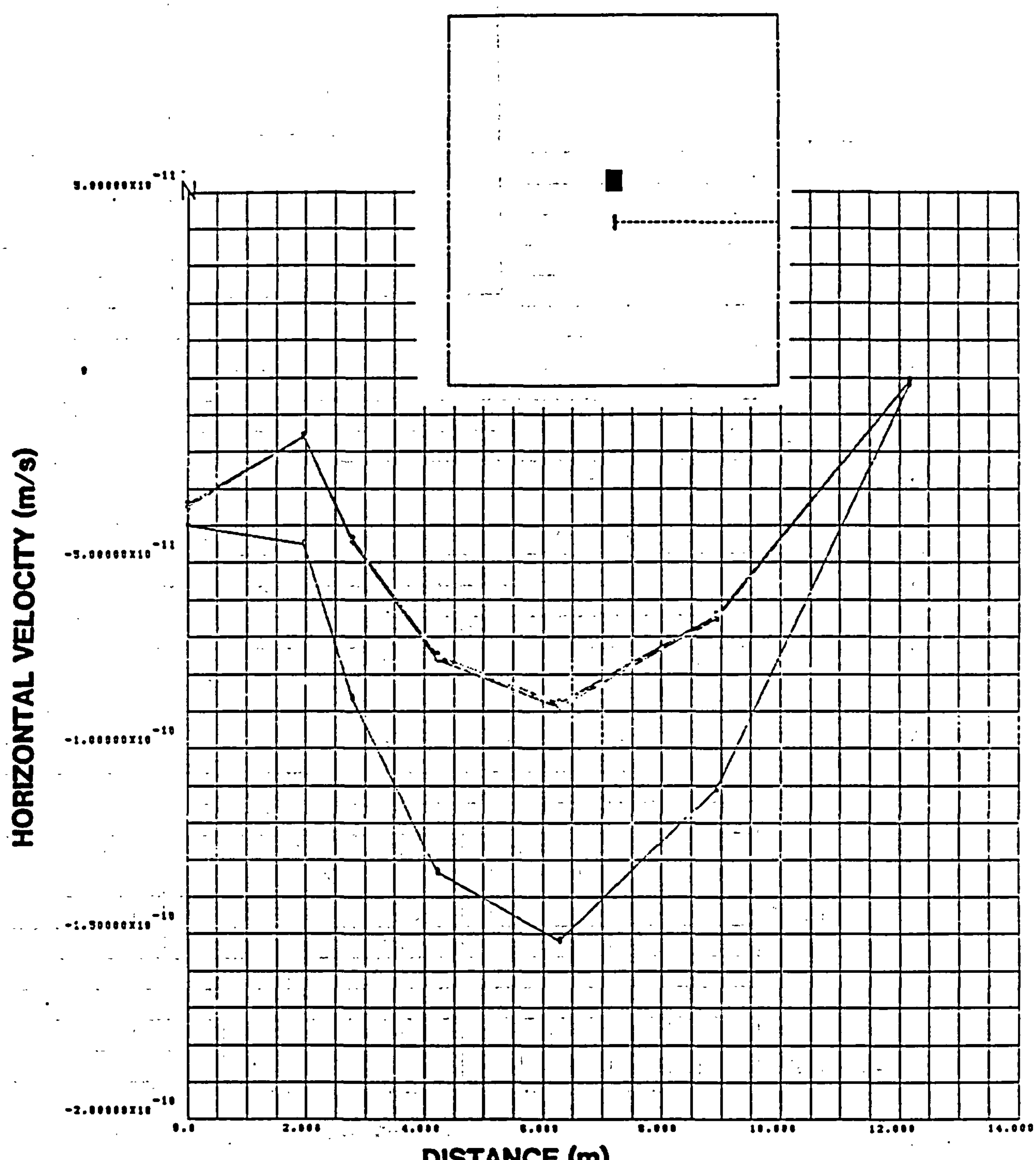

Figure 29. Horizontal Component of Superficial Velocity as a Function of Position -- Emplacement Scheme 2 (θ_{drift}/ϕ = 0.78)

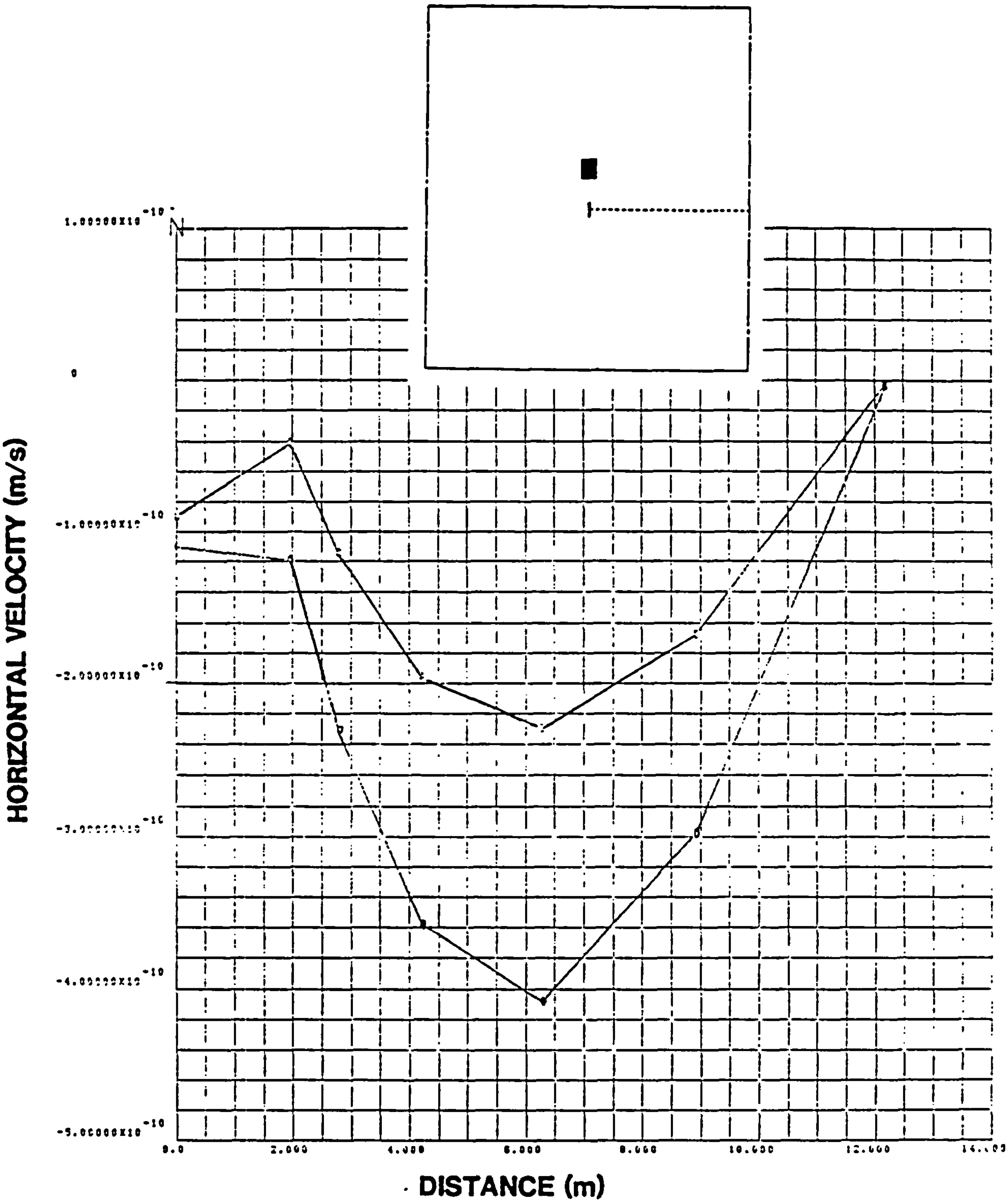

Figure 30. Horizontal Component of Superficial Velocity as a Function of Position -- Emplacement Scheme 2 (θ_{drift}/ϕ = 0.751)

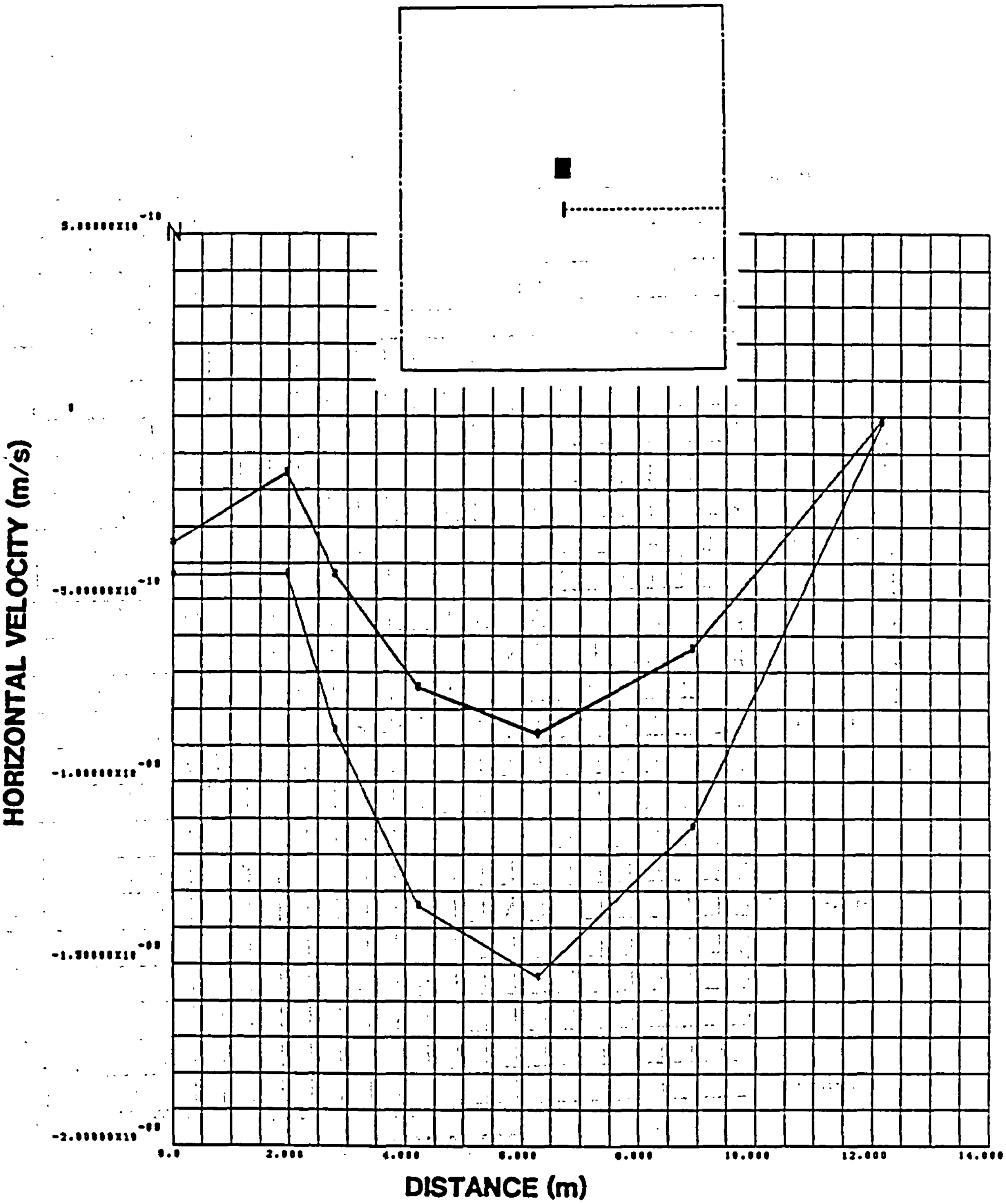

Figure 31. Horizontal Component of Superficial Velocity as a Function of Position -- Emplacement Scheme 2 (θ_{drift}/ϕ = 0.635)

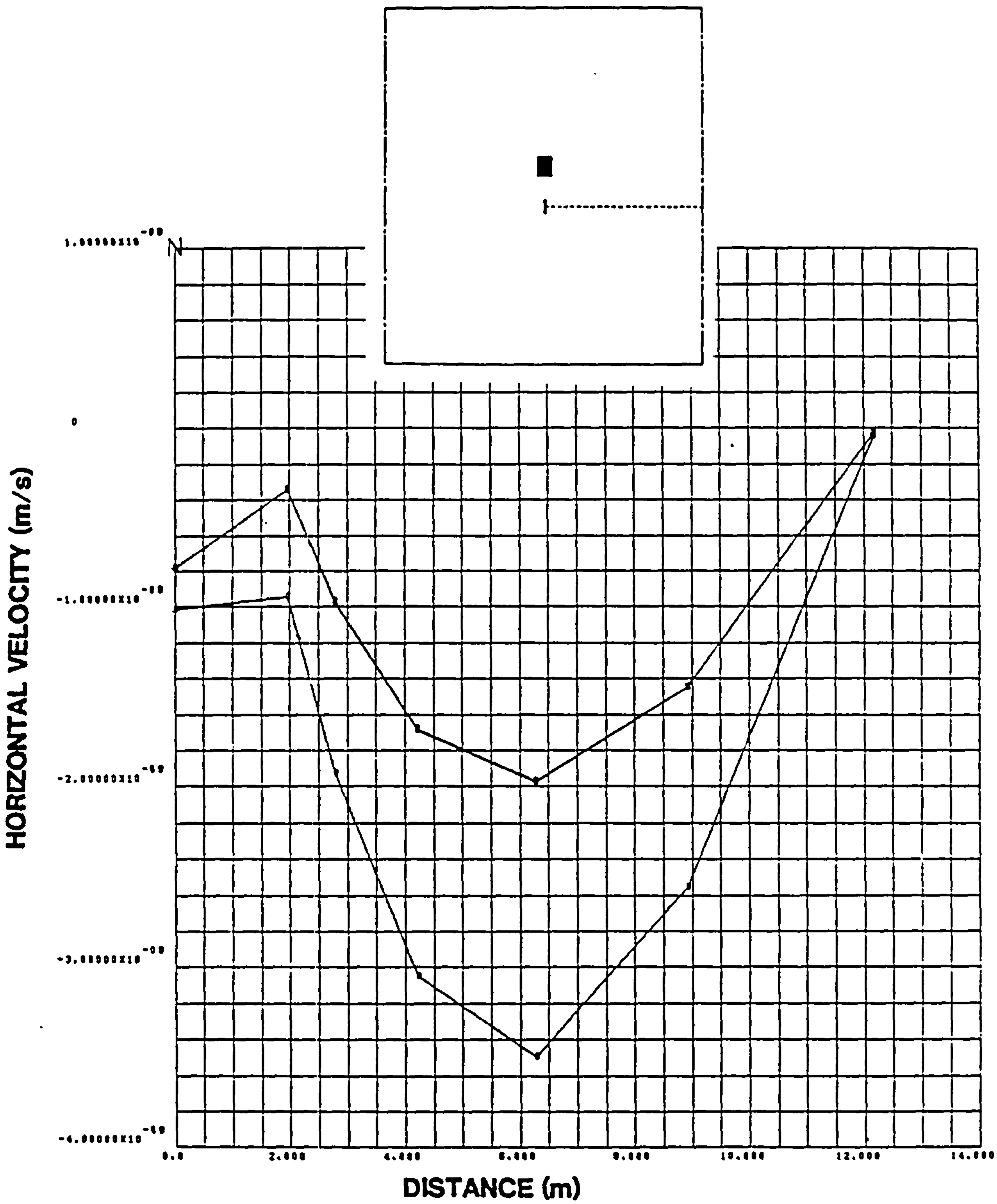

Figure 32. Horizontal Component of Superficial Velocity as a Function of Position -- Emplacement Scheme 2 ($\theta_{drift}/\phi = 0.47$)

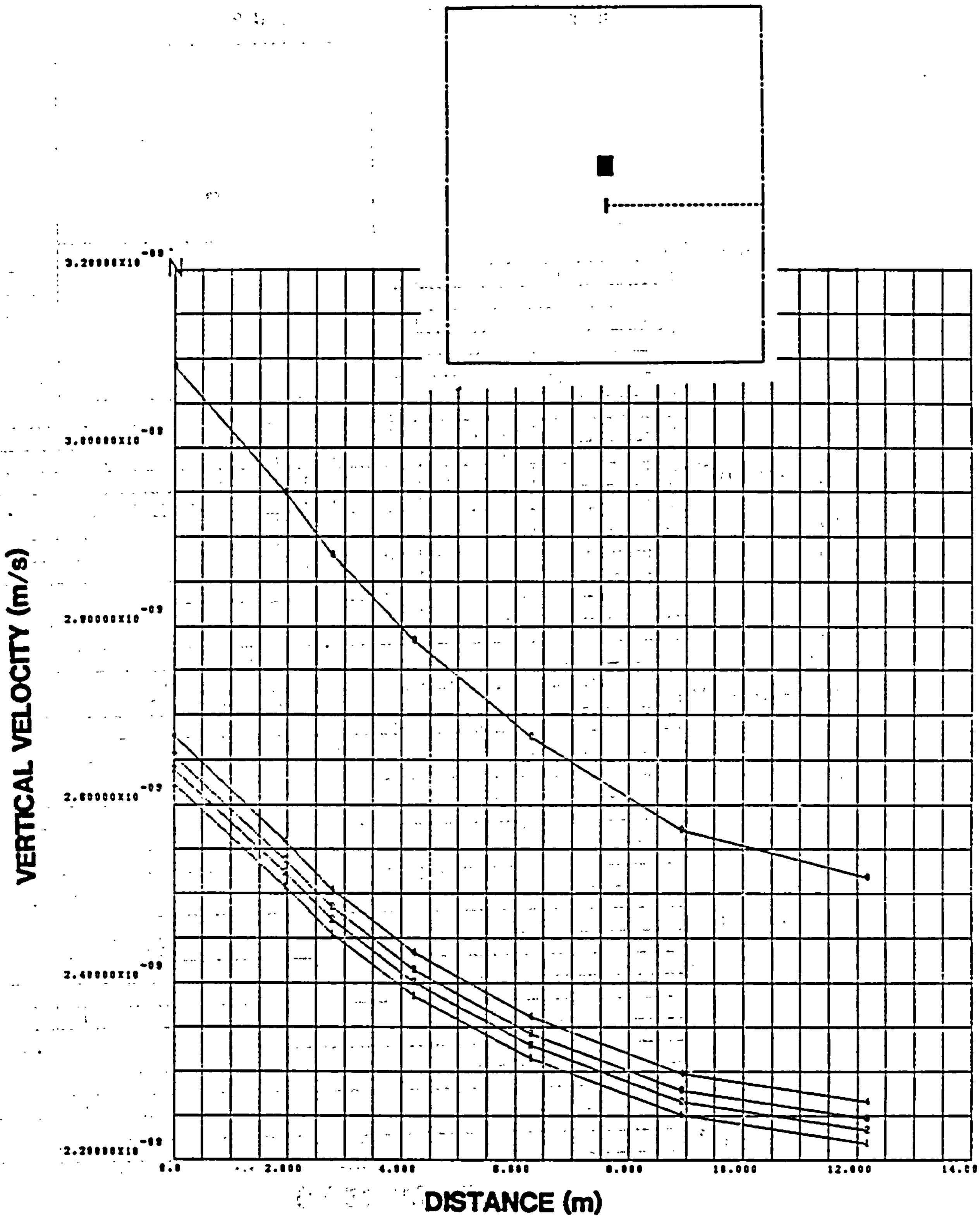

Figure 33. Vertical Component of Superficial Velocity as a Function of Position -- Emplacement Scheme 2 (θ_{drift}/ϕ = 0.78)

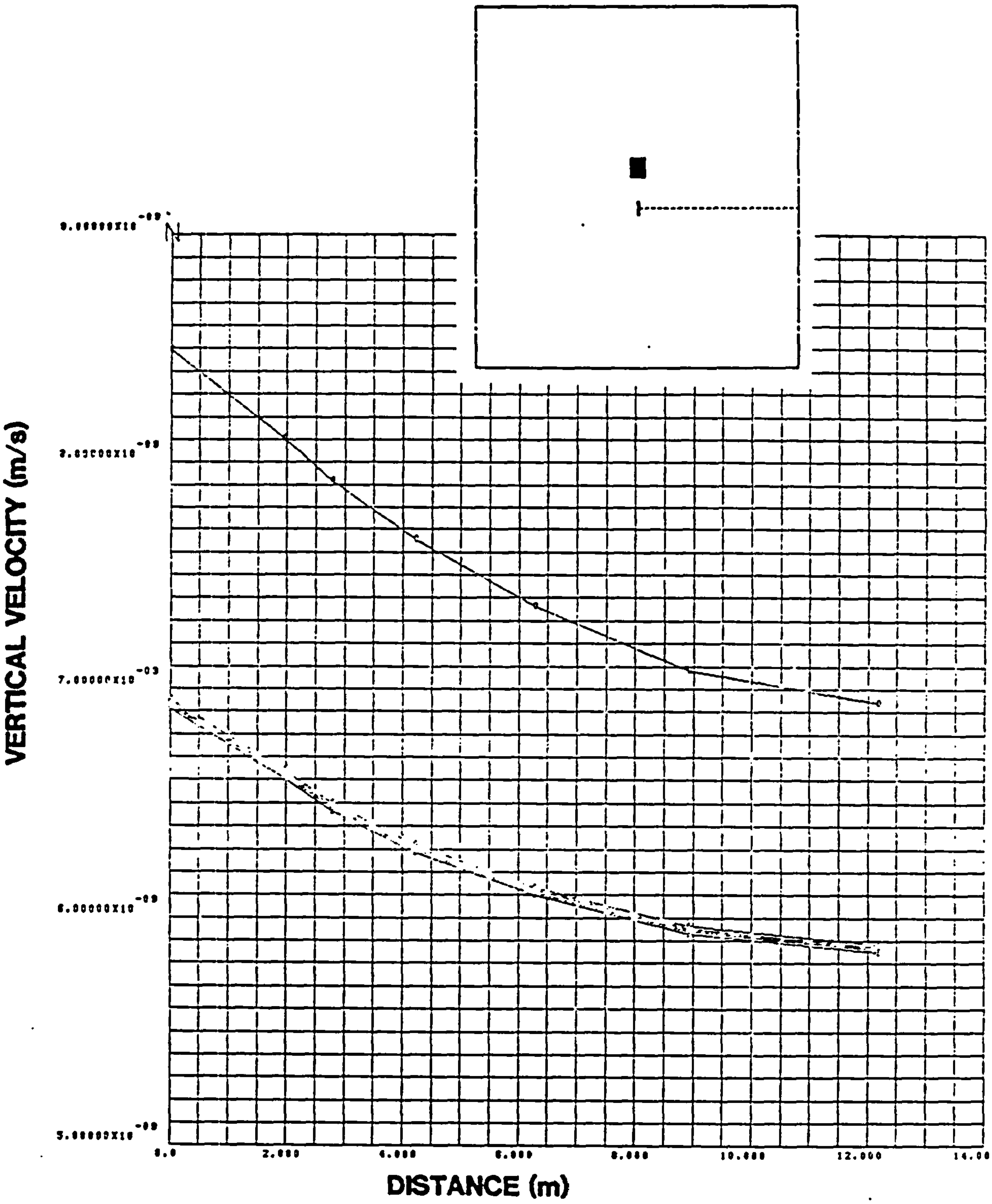

Figure 34. Vertical Component of Superficial Velocity as a Function of Position -- Emplacement Scheme 2 (θ_{drift}/ϕ = 0.751)

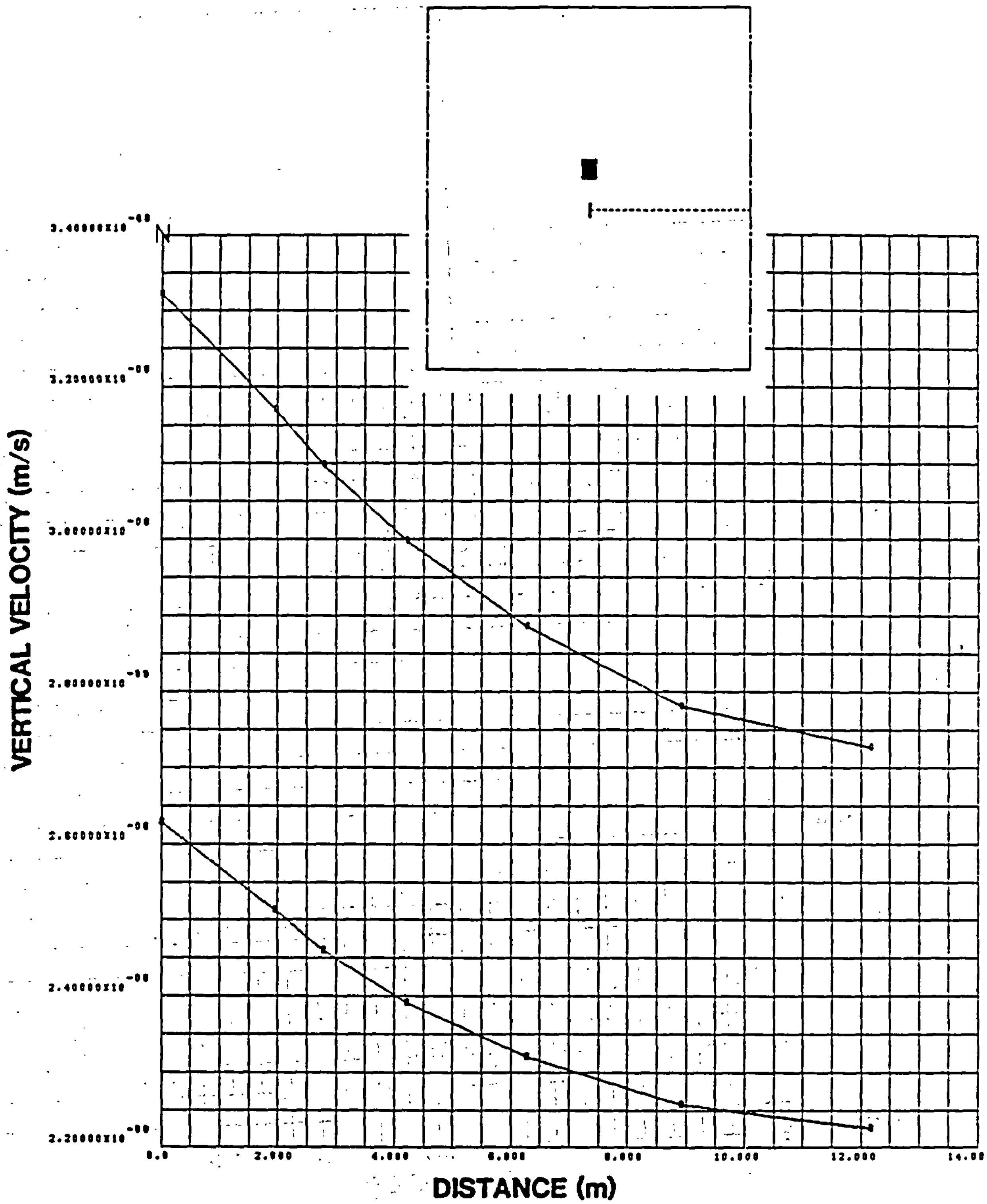

Figure 35. Vertical Component of Superficial Velocity as a Function of Position -- Emplacement Scheme 2 ($\theta_{drift}/\phi = 0.635$)

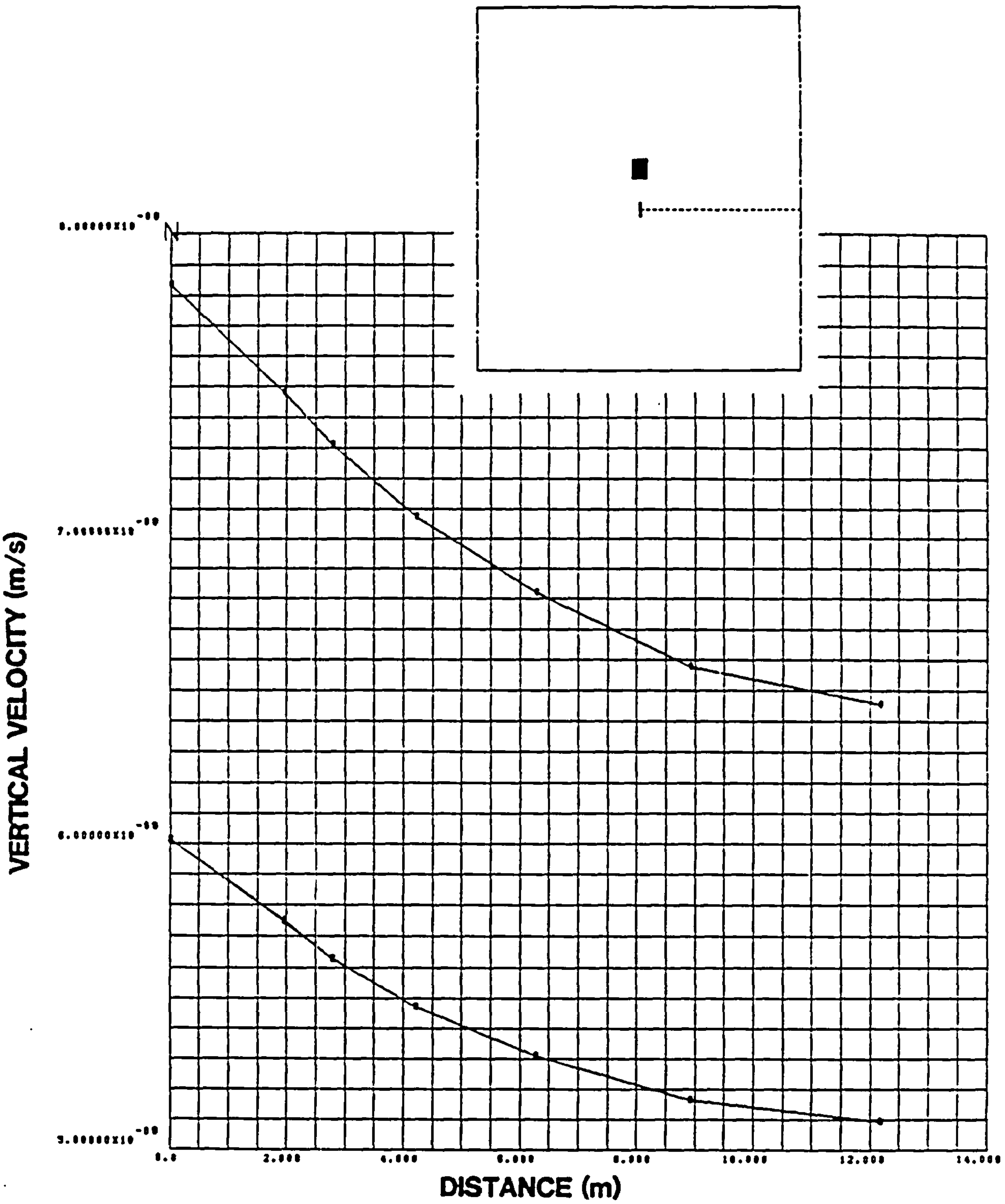

Figure 36. Vertical Component of Superficial Velocity as a Function of Position -- Emplacement Scheme 2 (θ_{drift}/ϕ = 0.47)

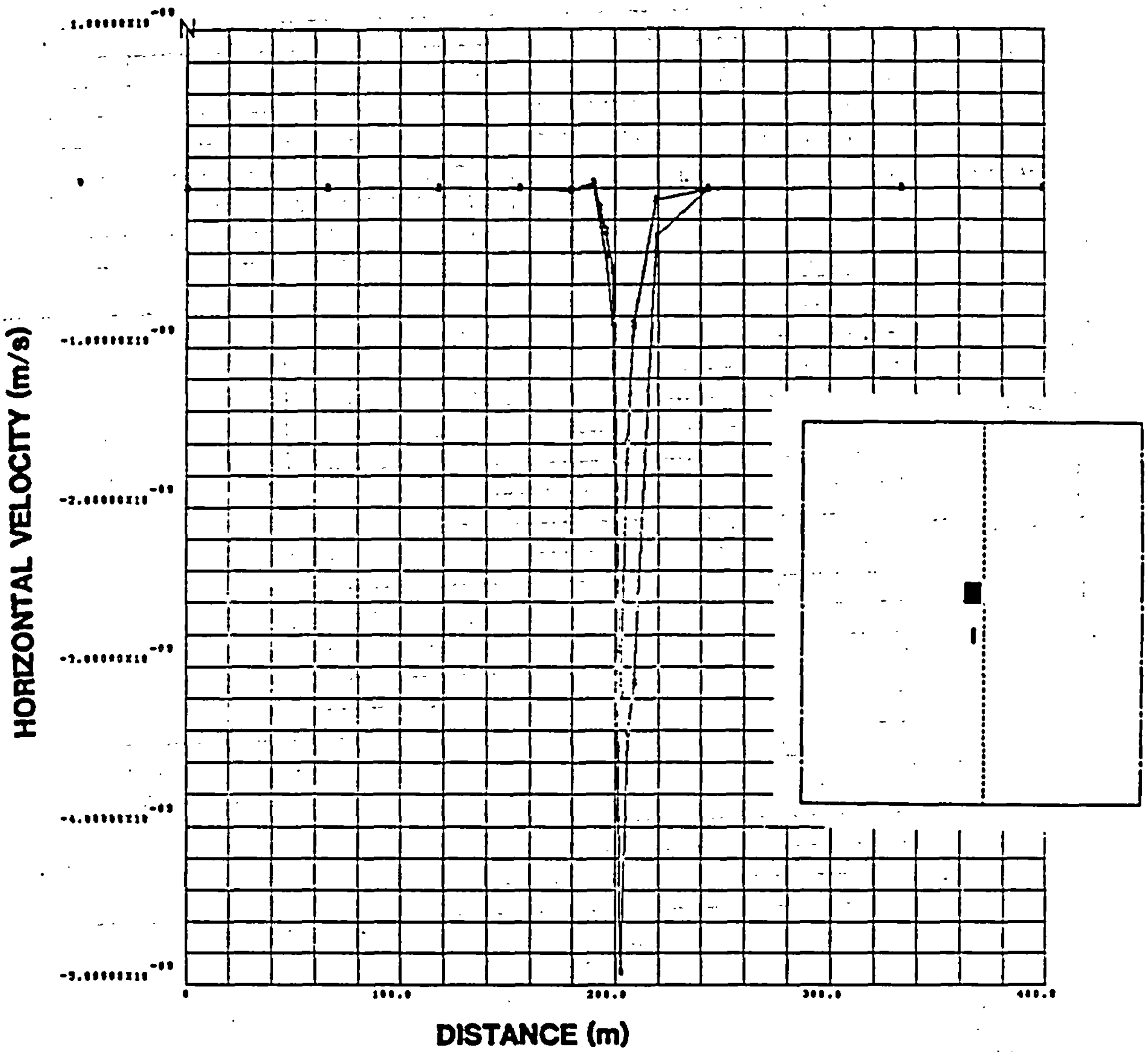

Figure 37. Horizontal Component of Superficial Velocity as a Function of Position -- Emplacement Scheme 2 (θ_{drift}/ϕ = 0.78)

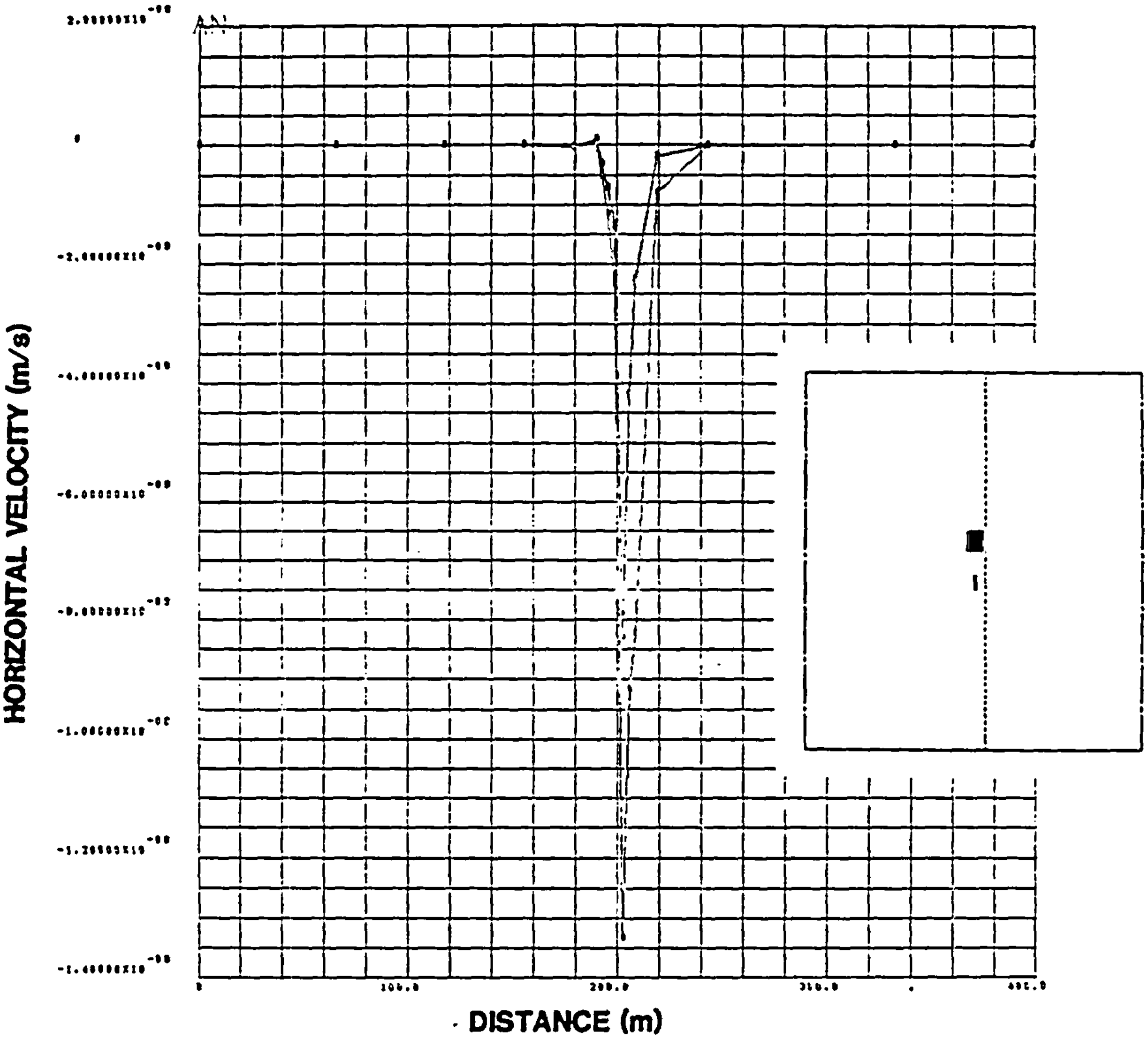

Figure 38. Horizontal Component of Superficial Velocity as a Function of Position -- Emplacement Scheme 2 (θ_{drift}/ϕ = 0.751)

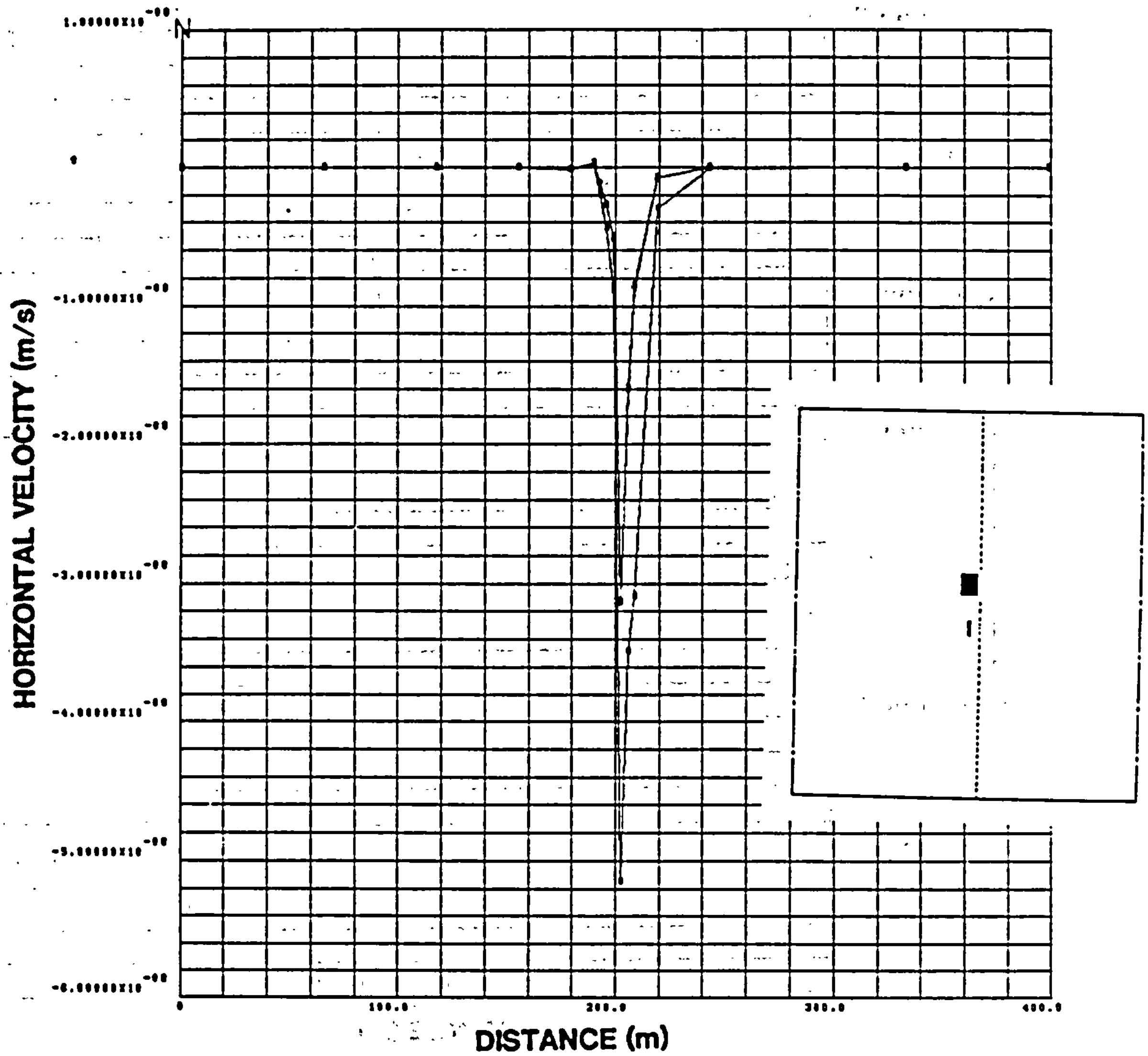

Figure 39. Horizontal Component of Superficial Velocity as a Function of Position -- Emplacement Scheme 2 (θ_{drift}/ϕ = 0.635)

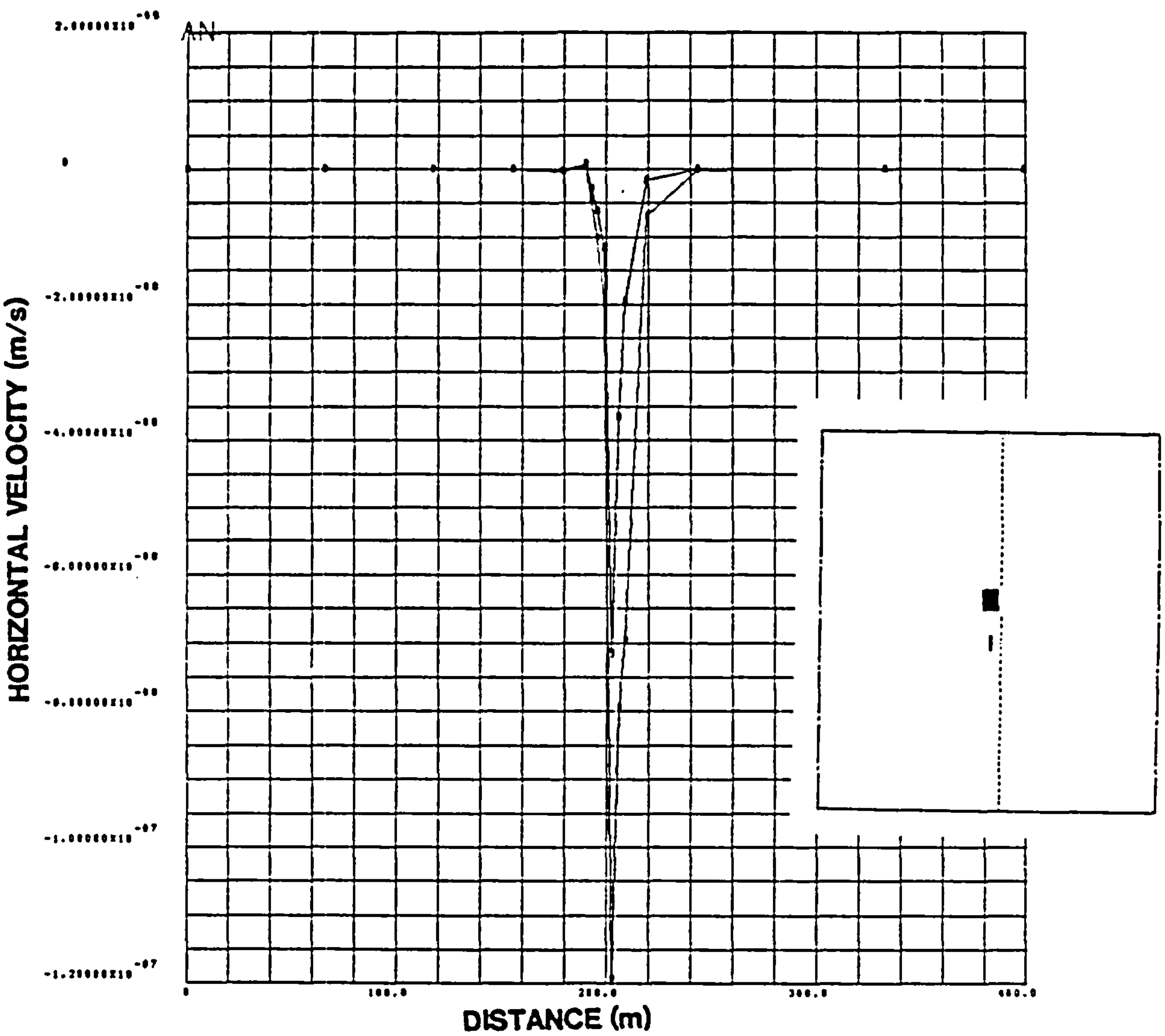

Figure 40. Horizontal Component of Superficial Velocity as a Function of Position -- Emplacement Scheme 2 (θ_{drift}/ϕ = 0.47)

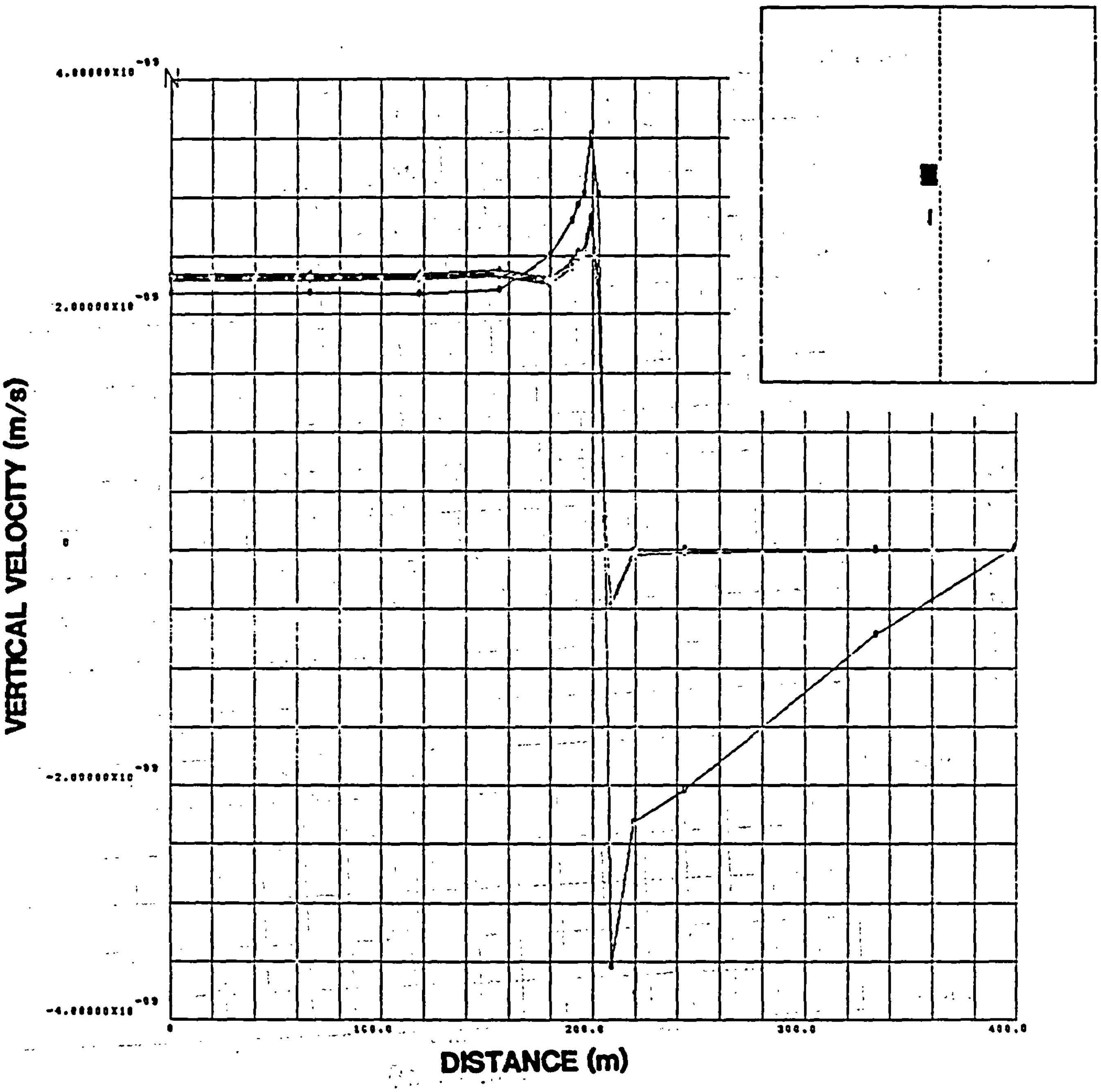

Figure 41. Vertical Component of Superficial Velocity as a Function of Position -- Emplacement Scheme 2 (θ_{drift}/ϕ = 0.78)

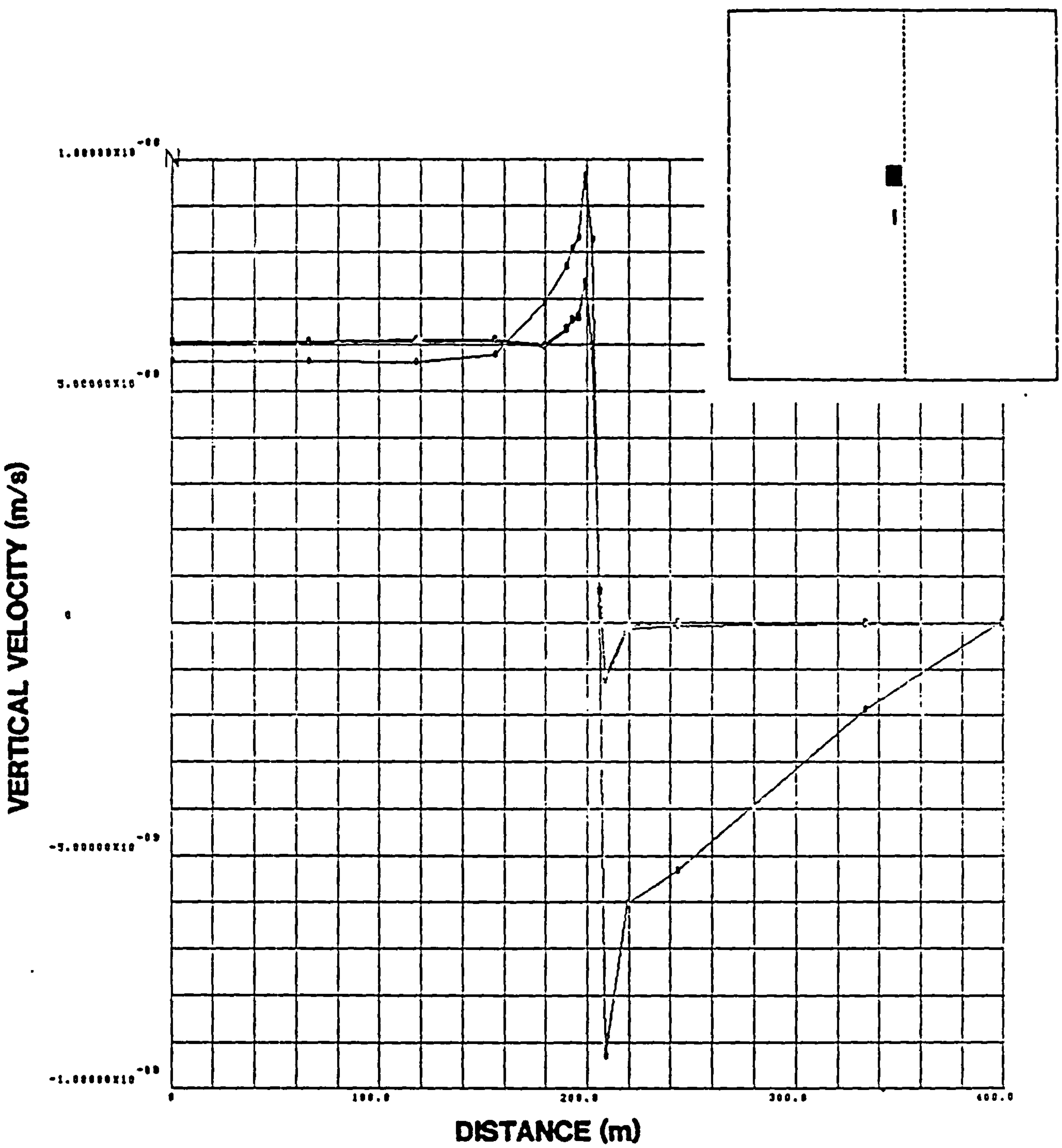

Figure 42. Vertical Component of Superficial Velocity as a Function of Position -- Emplacement Scheme 2 ($\theta_{drift}/\phi = 0.751$)

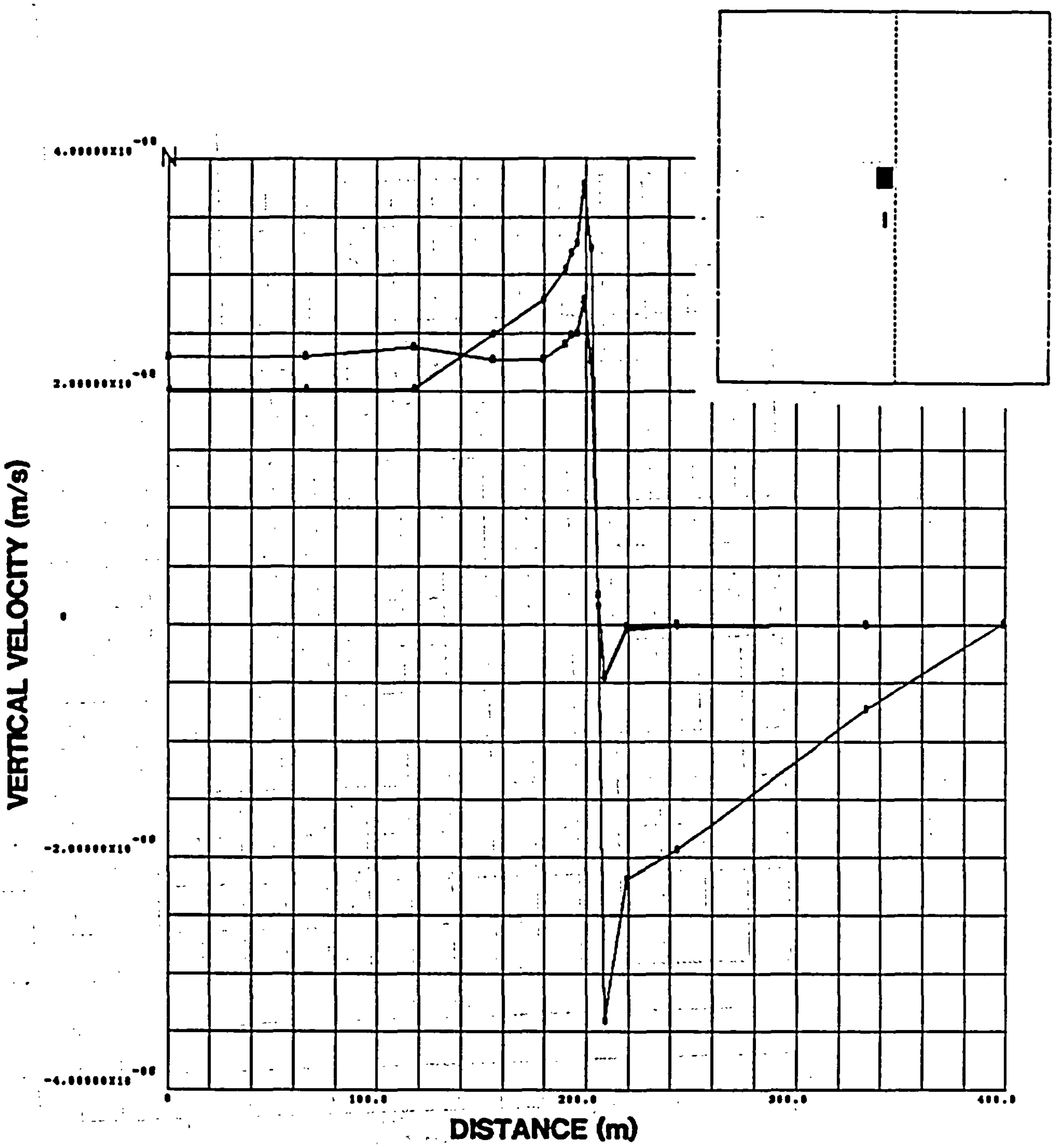

Figure 43. Vertical Component of Superficial Velocity as a Function of Position -- Emplacement Scheme 2 ($\theta_{drift}/\phi = 0.635$)

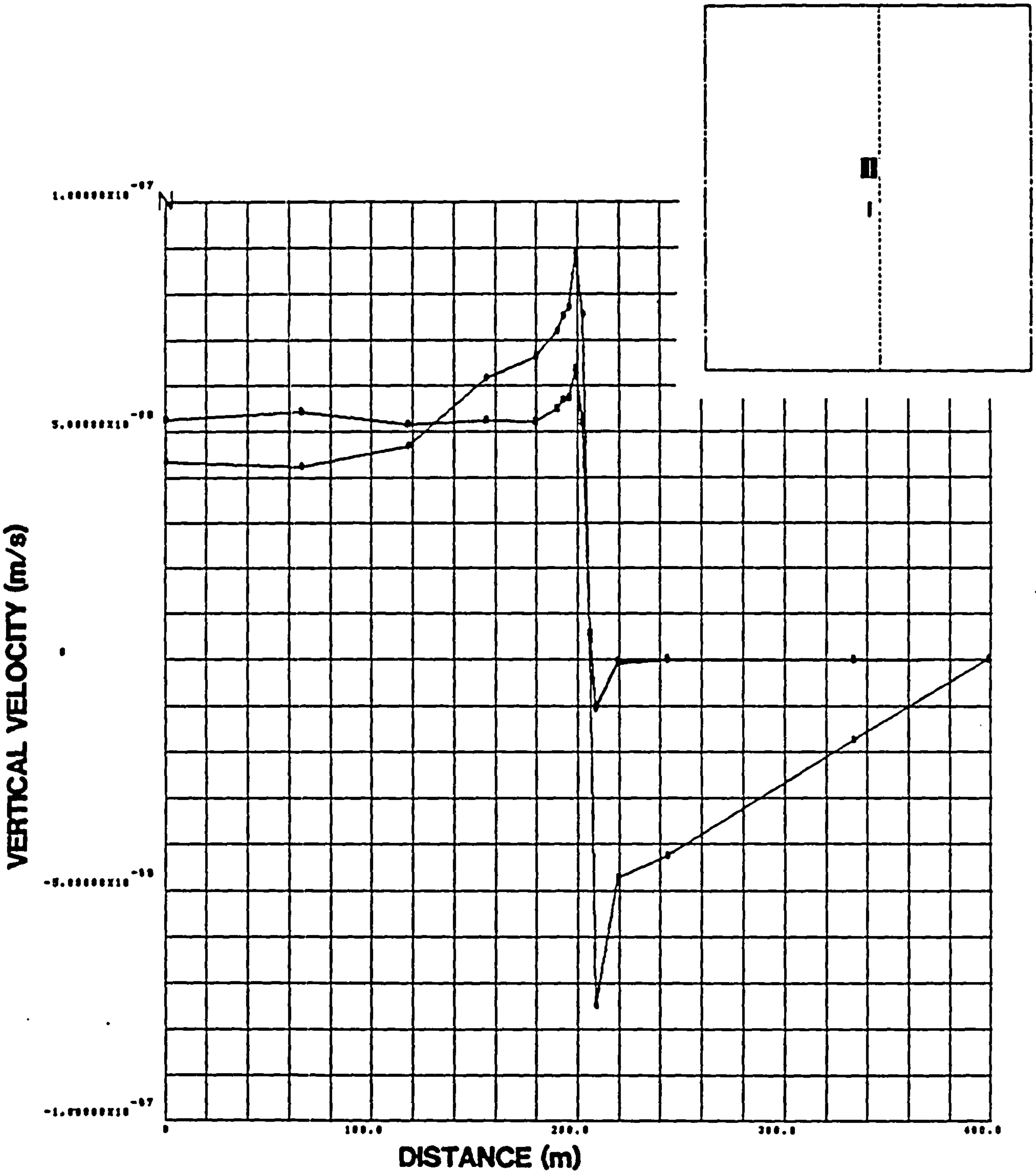

Figure 44. Vertical Component of Superficial Velocity as a Function of Position -- Emplacement Scheme 2 ($\theta_{drift}/\phi = 0.47$)

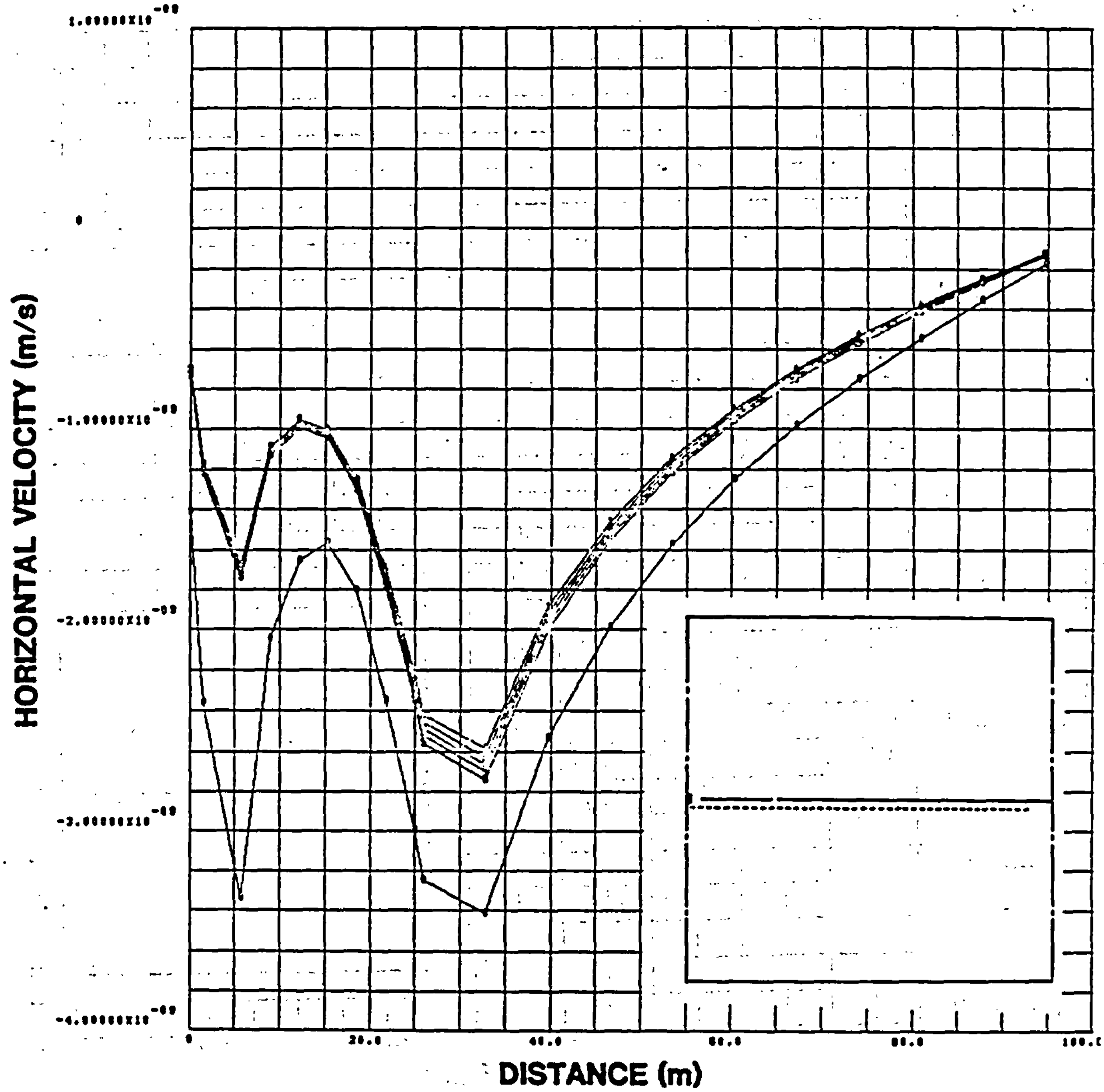

Figure 45. Horizontal Component of Superficial Velocity as a Function of Position -- Emplacement Scheme 3 (θ_{drift}/ϕ = 0.78)

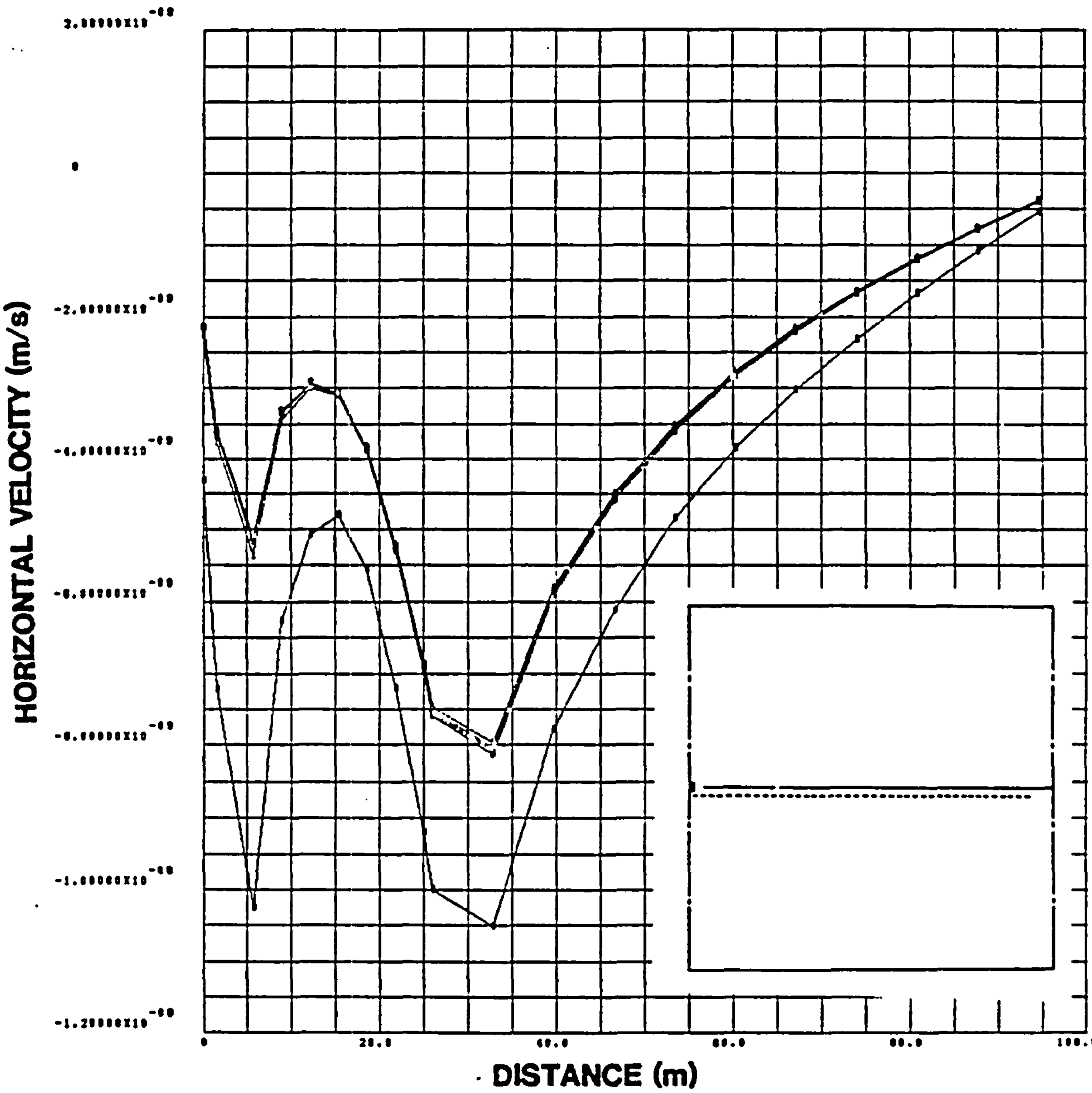

Figure 46. Horizontal Component of Superficial Velocity as a Function of Position -- Emplacement Scheme 3 (θ_{drift}/ϕ = 0.751)

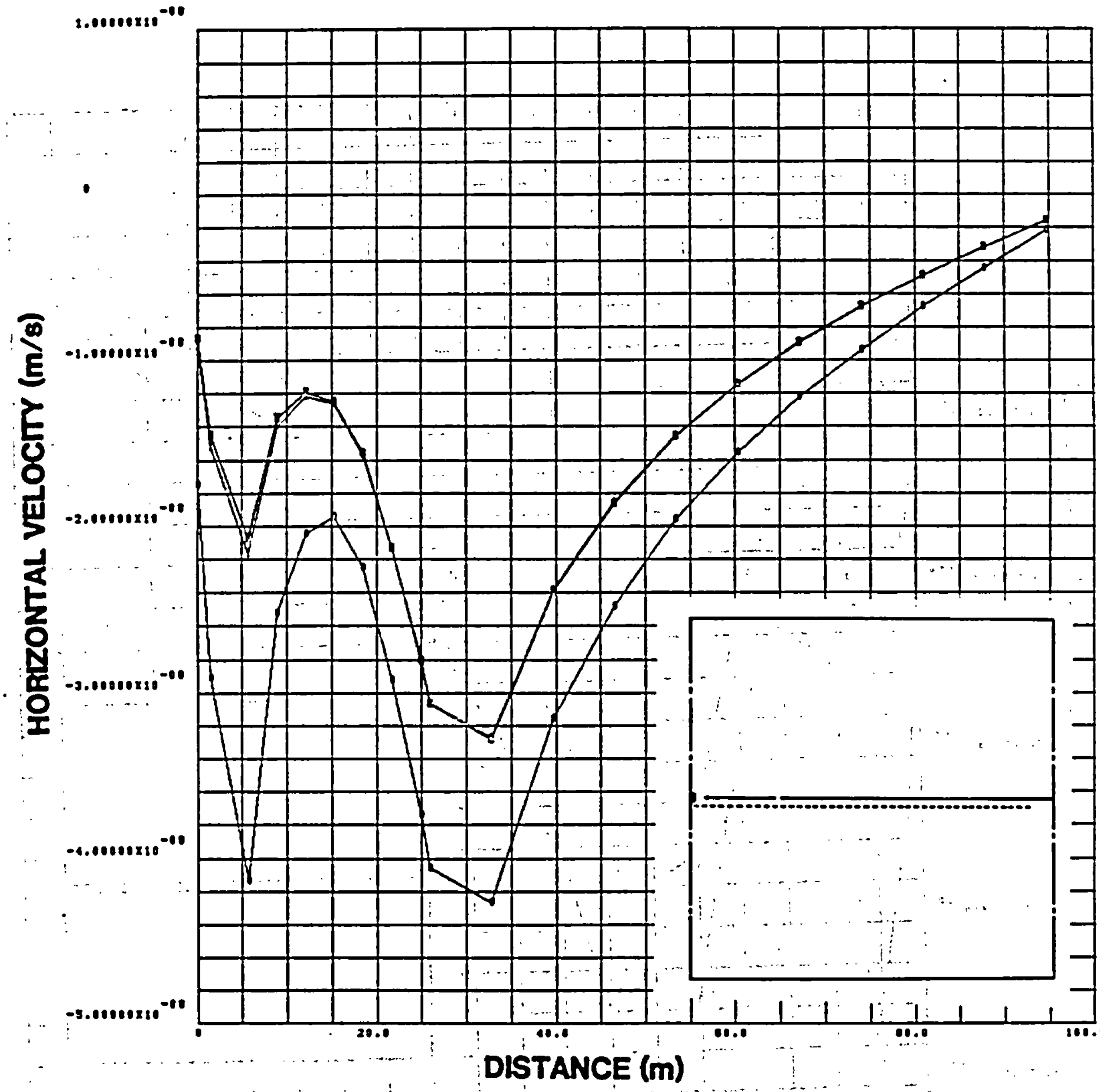

Figure 47. Horizontal Component of Superficial Velocity as a Function of Position -- Emplacement Scheme 3 (θ_{drift}/ϕ = 0.635)

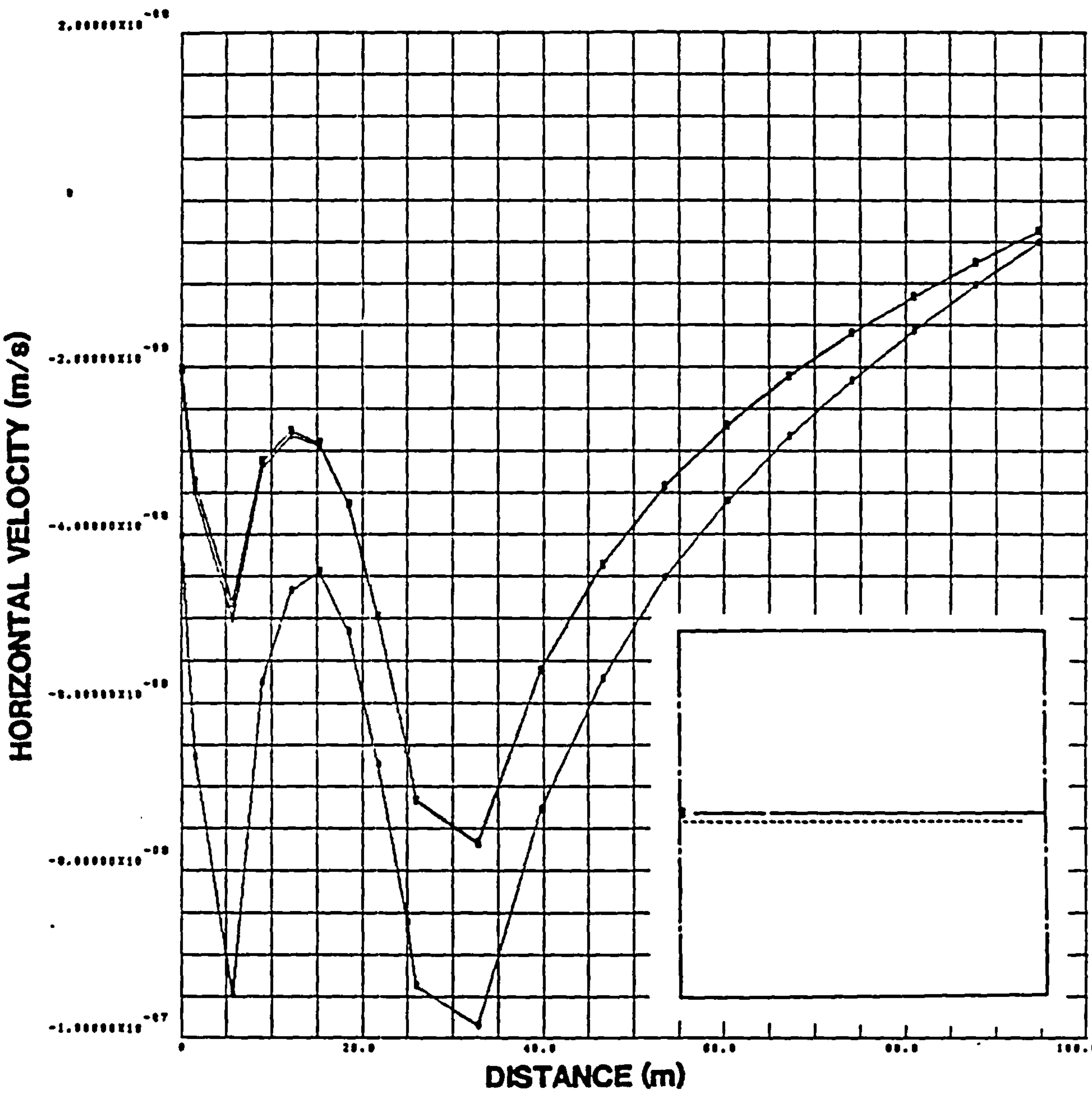

Figure 48. Horizontal Component of Superficial Velocity as a Function of Position -- Emplacement Scheme 3 ($\theta_{drift}/\phi = 0.47$)

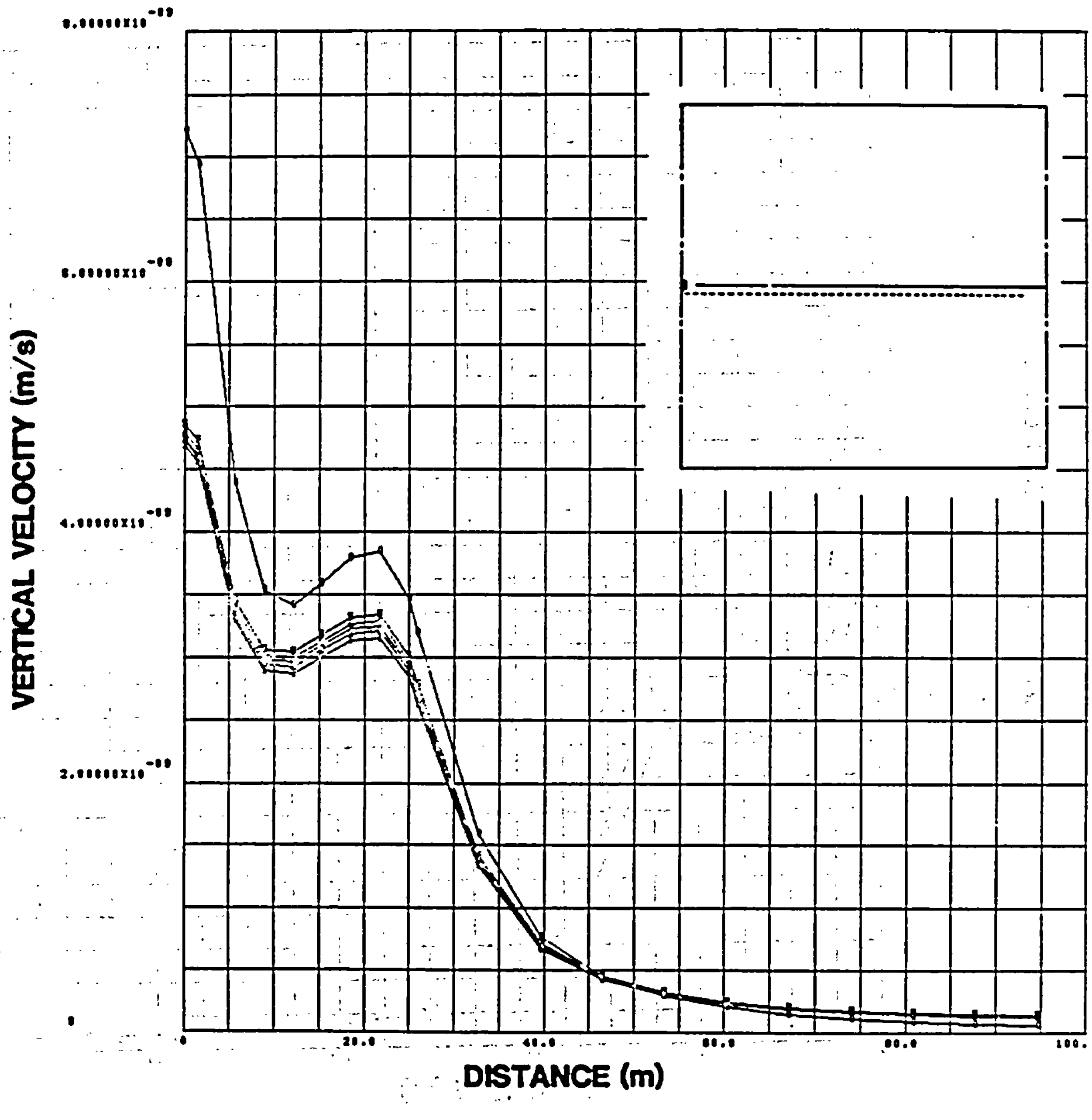

Figure 49. Vertical Component of Superficial Velocity as a Function of Position -- Emplacement Scheme 3 (θ_{drift}/ϕ = 0.78)

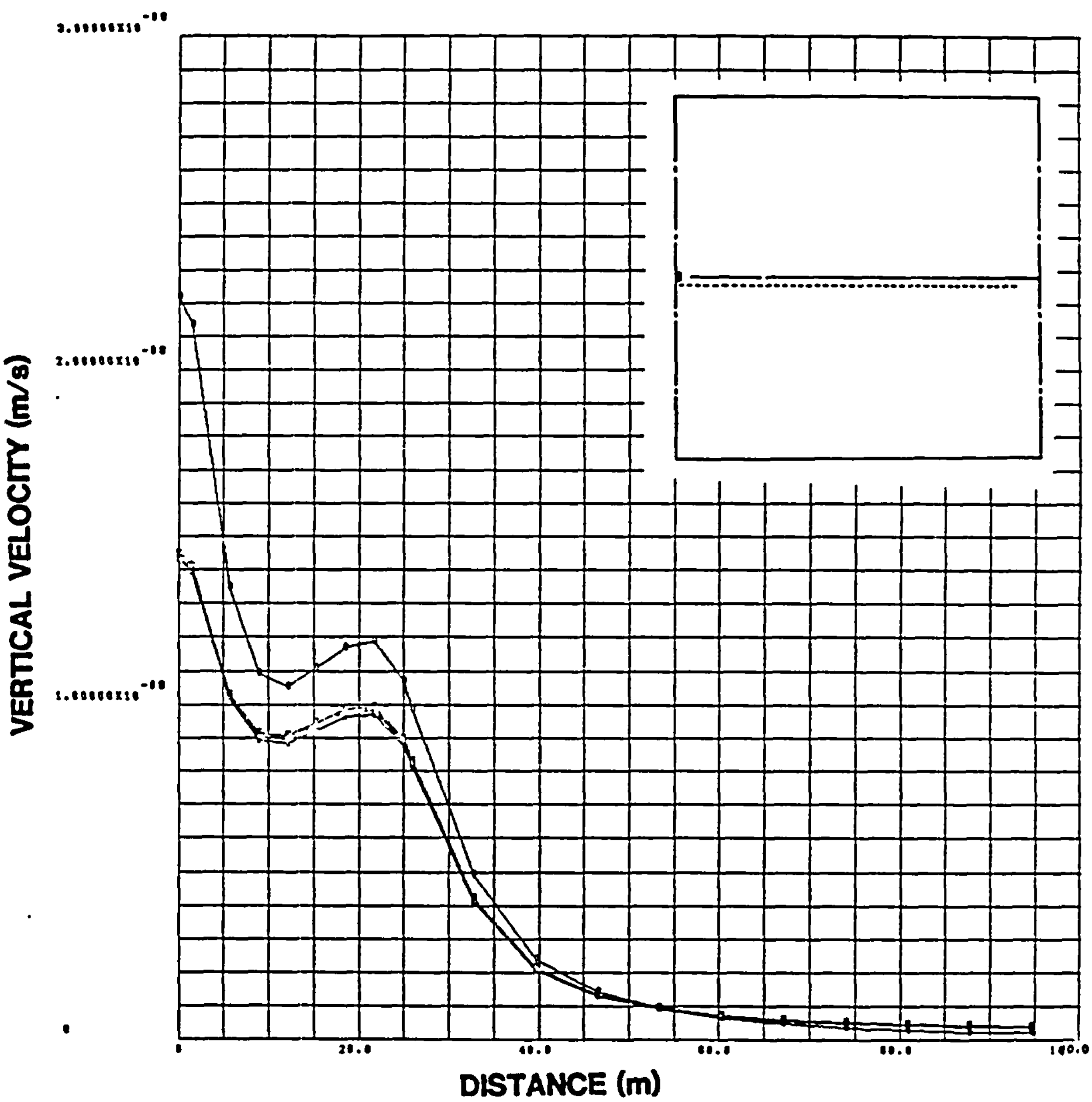

Figure 50. Vertical Component of Superficial Velocity as a Function of Position -- Emplacement Scheme 3 (θ_{drift}/ϕ = 0.751)

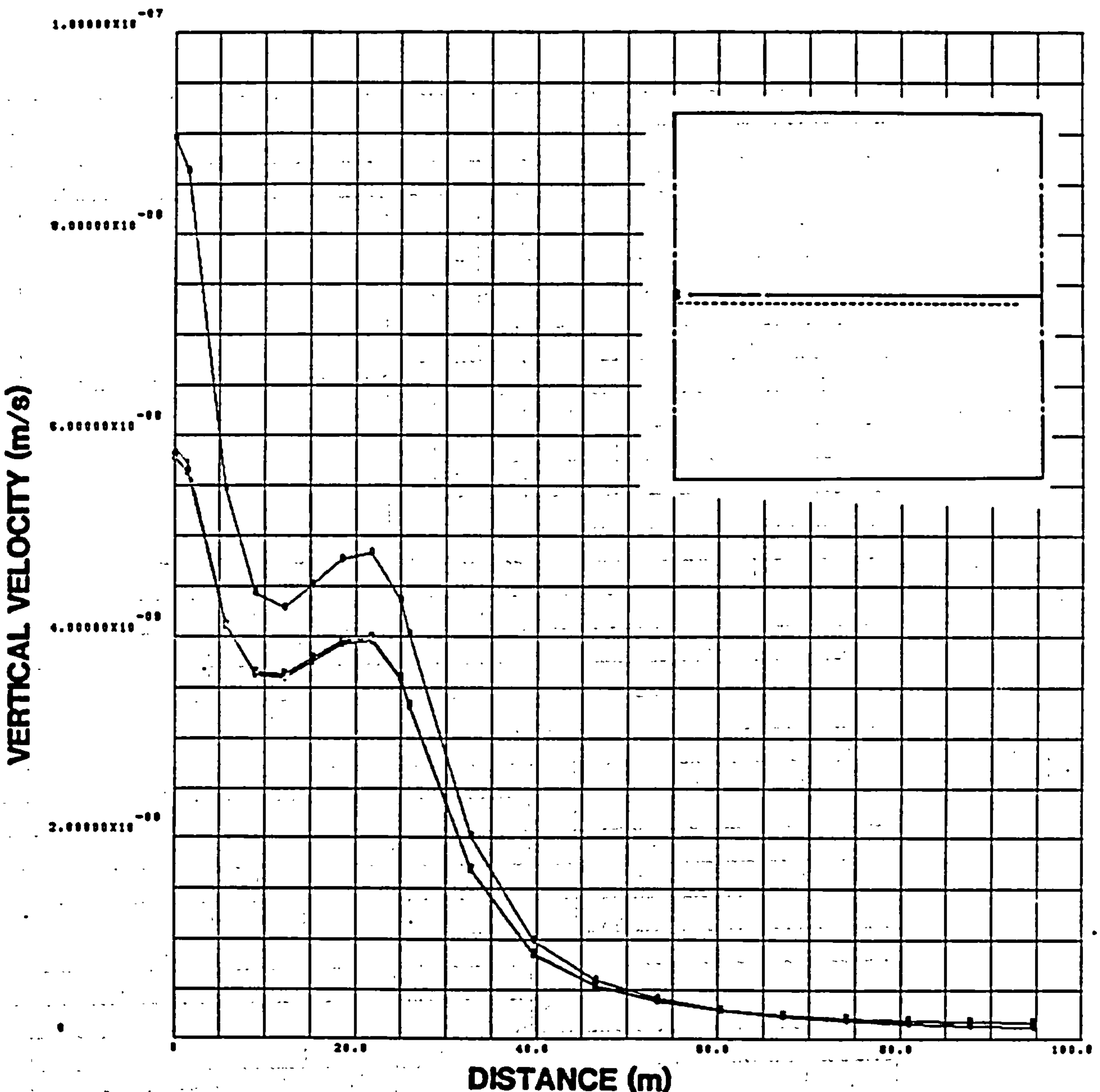

Figure 51. Vertical Component of Superficial Velocity as a Function of Position -- Emplacement Scheme 3 (θ_{drift}/ϕ = 0.635)

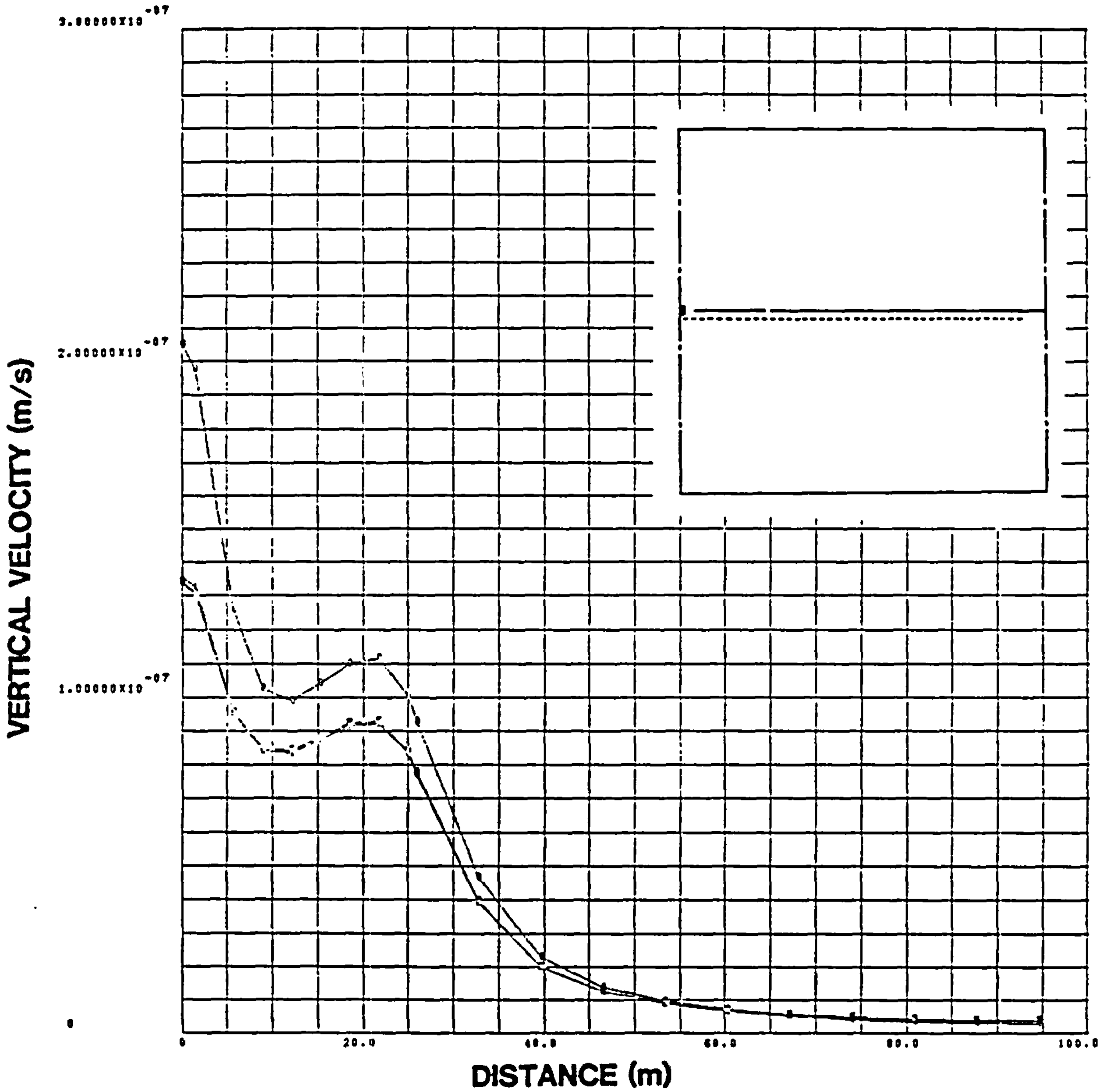

Figure 52. Vertical Component of Superficial Velocity as a Function of Position -- Emplacement Scheme 3 (θ_{drift}/ϕ = 0.47)

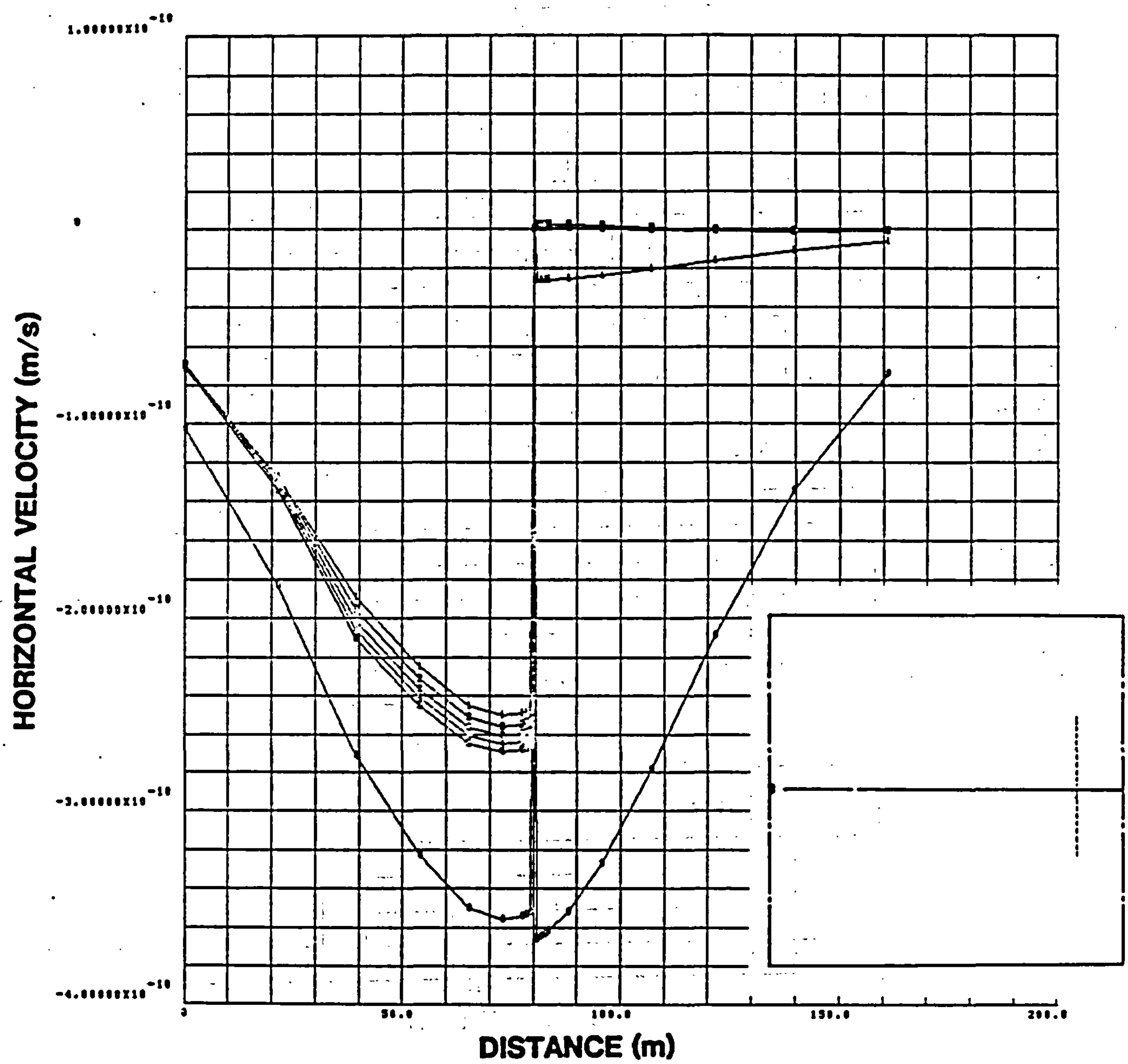

Figure 53. Horizontal Component of Superficial Velocity as a Function of Position -- Emplacement Scheme 3 ($\theta_{drift}/\phi = 0.78$)

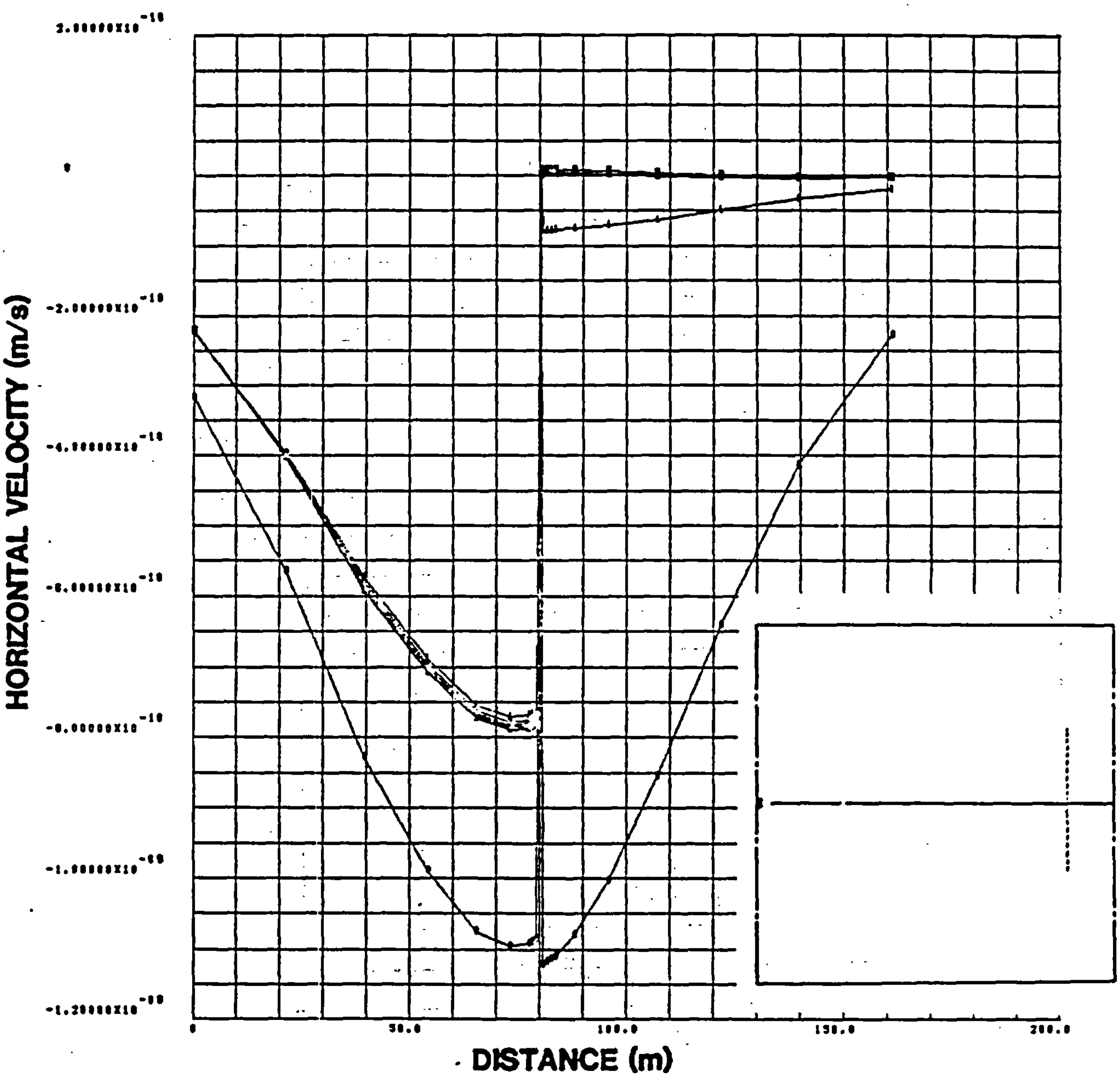

Figure 54. Horizontal Component of Superficial Velocity as a Function of Position -- Emplacement Scheme 3 (θ_{drift}/ϕ = 0.751)

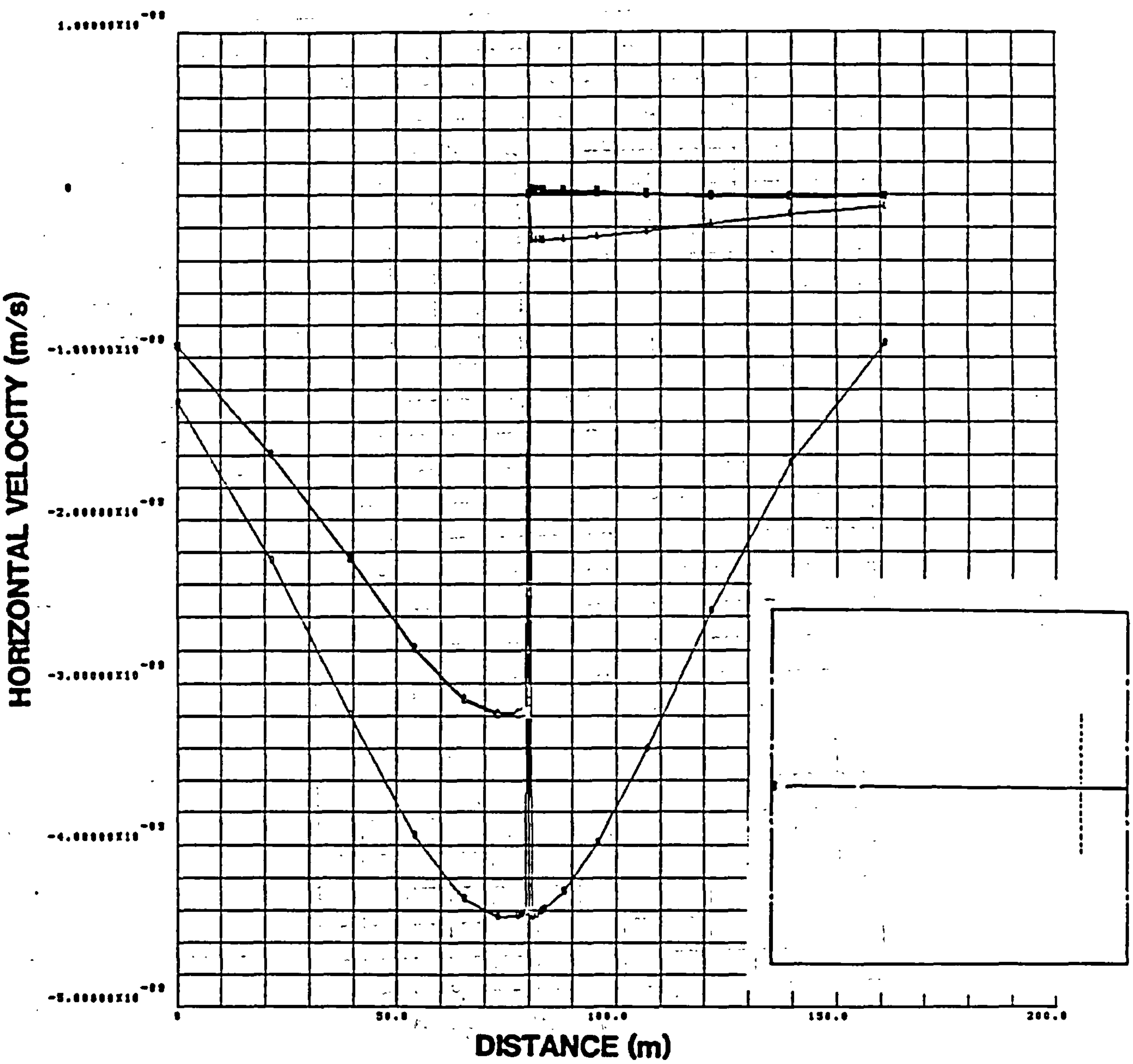

Figure 55. Horizontal Component of Superficial Velocity as a Function of Position -- Emplacement Scheme 3 (θ_{drift}/ϕ = 0.635)

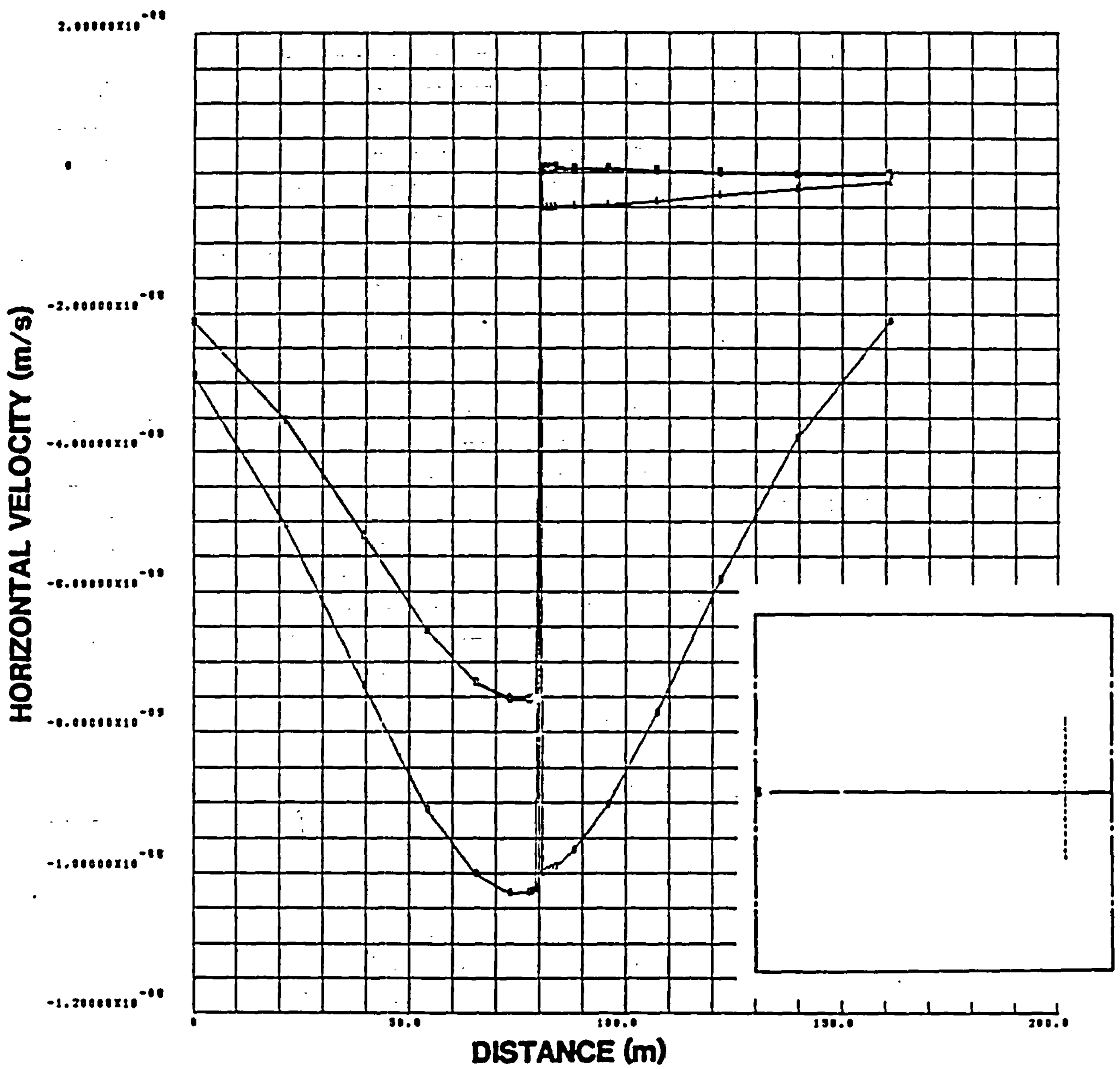

Figure 56. Horizontal Component of Superficial Velocity as a Function of Position -- Emplacement Scheme 3 (θ_{drift}/ϕ = 0.47)

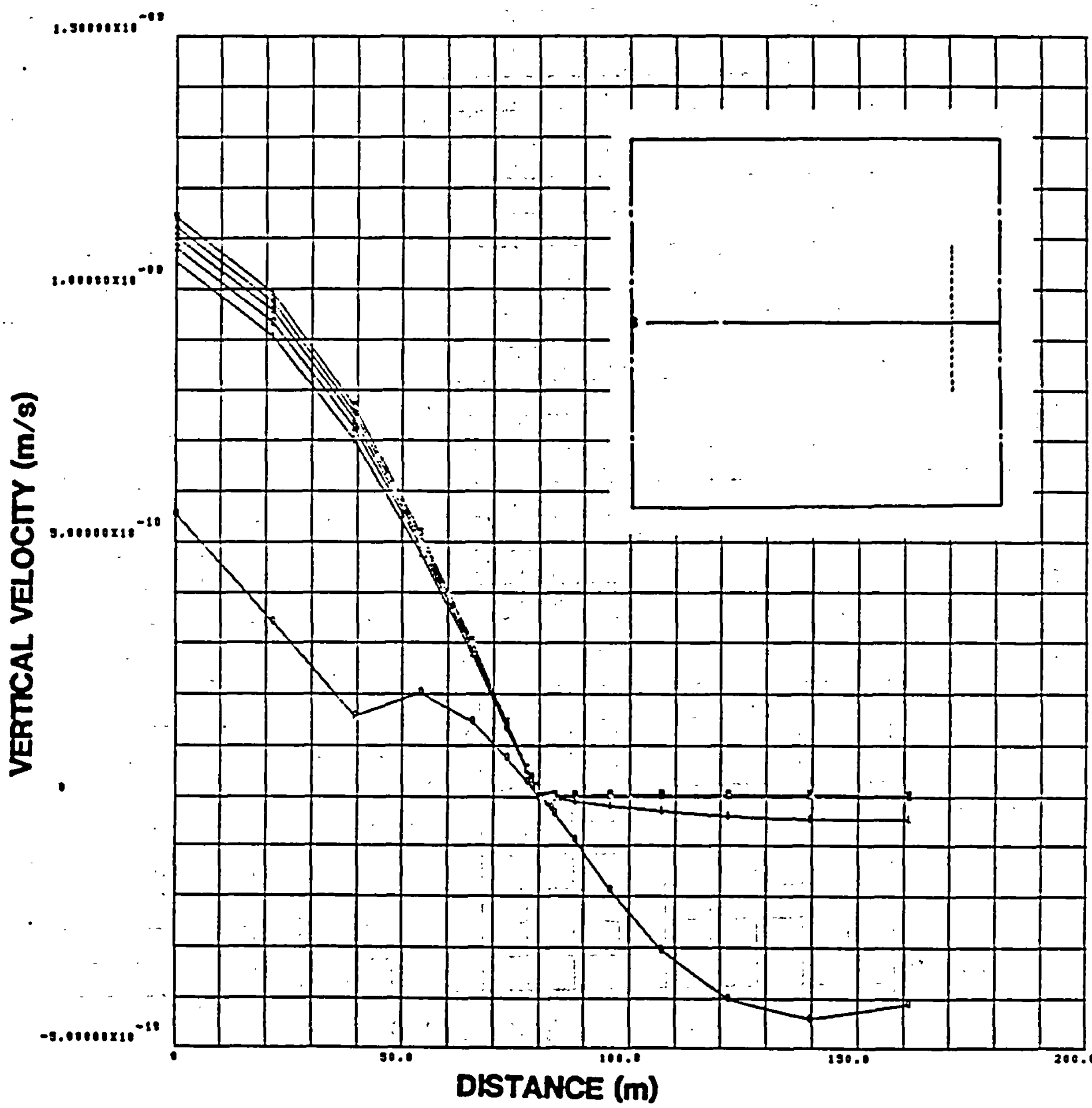

Figure 57. Vertical Component of Superficial Velocity as a Function of Position -- Emplacement Scheme 3 (θ_{drift}/ϕ = 0.78)

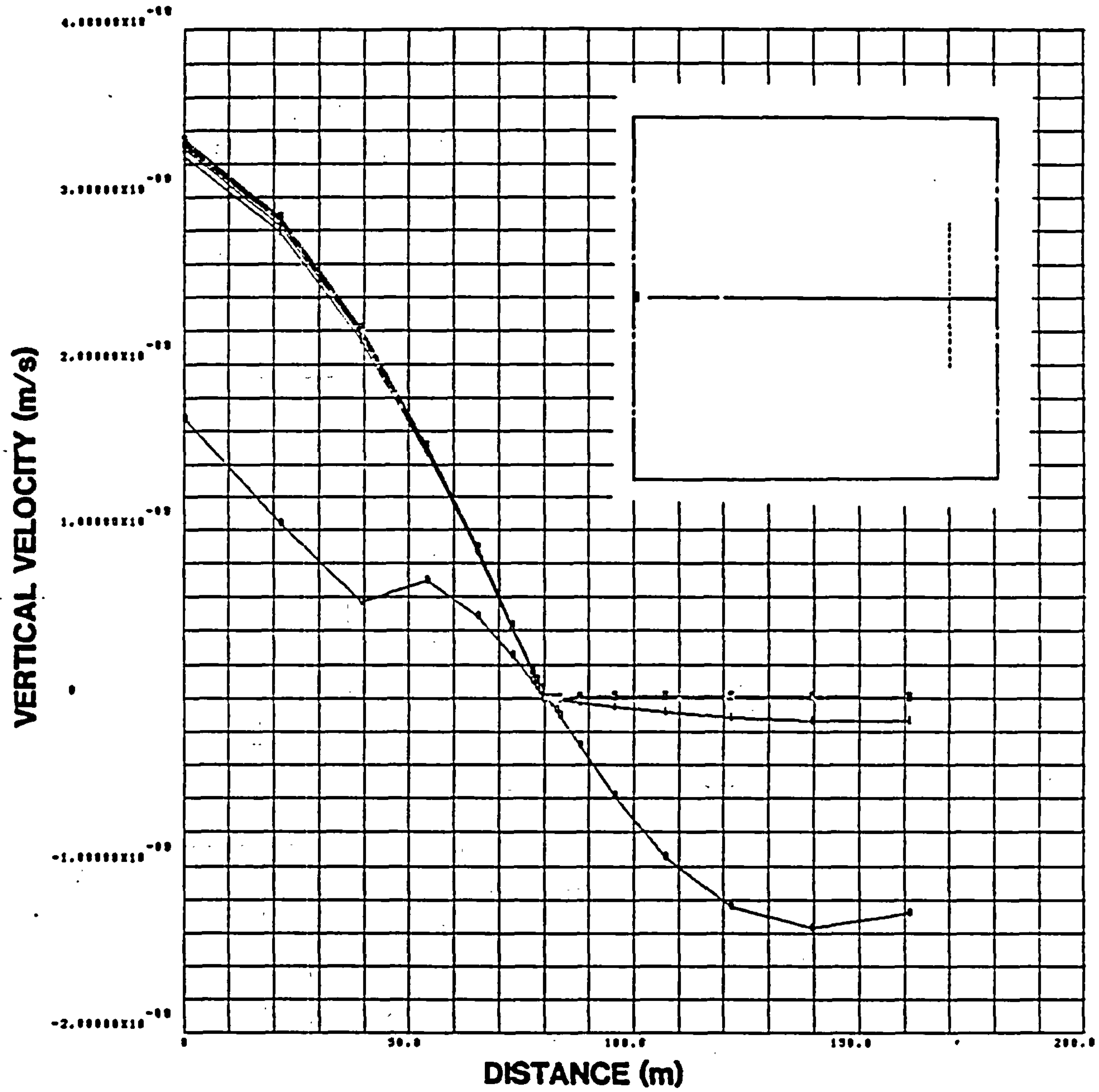

Figure 58. Vertical Component of Superficial Velocity as a Function of Position -- Emplacement Scheme 3 (θ_{drift}/ϕ = 0.751)

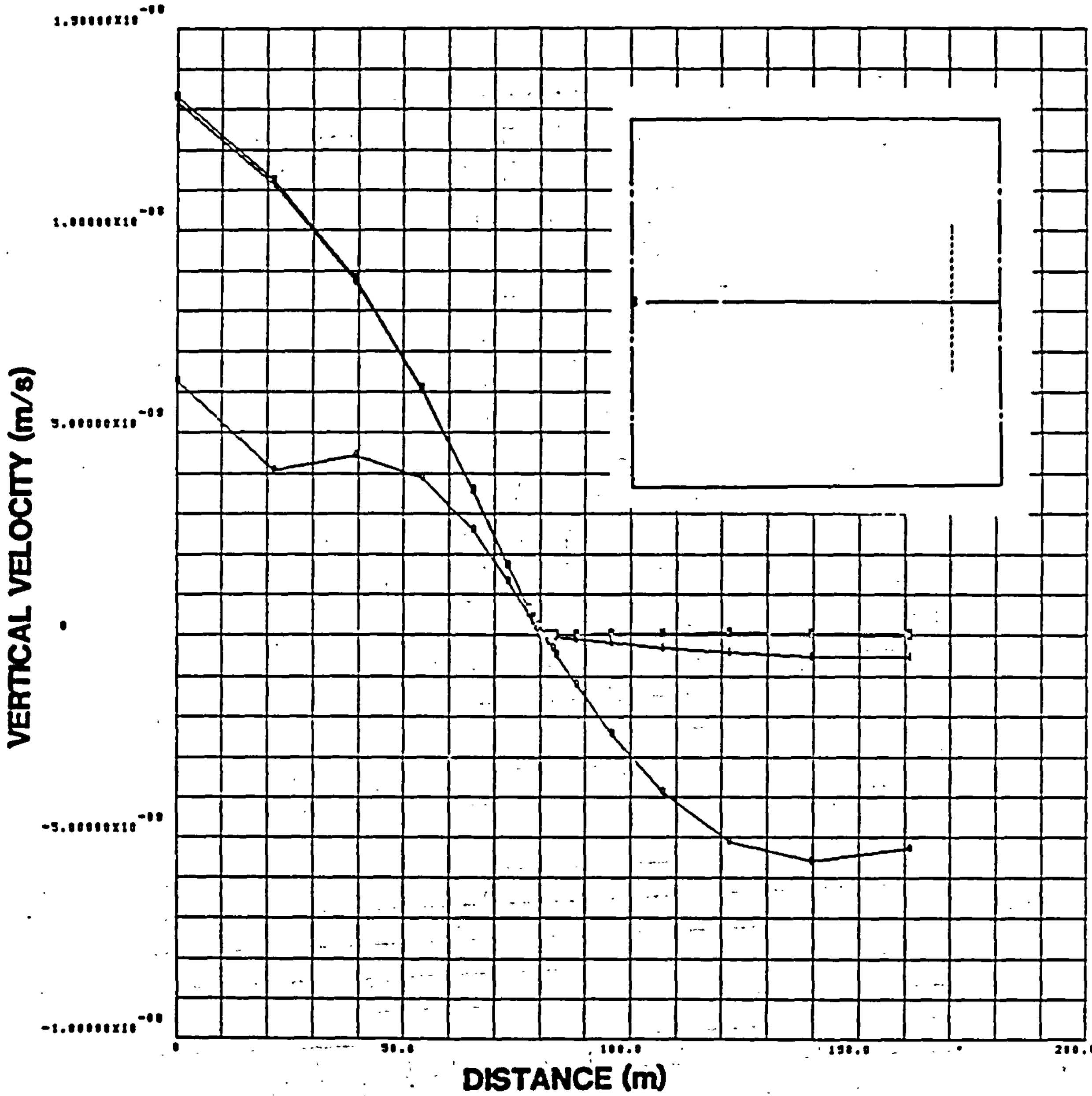

Figure 59. Vertical Component of Superficial Velocity as a Function of Position -- Emplacement Scheme 3 ($\theta_{drift}/\phi = 0.635$)

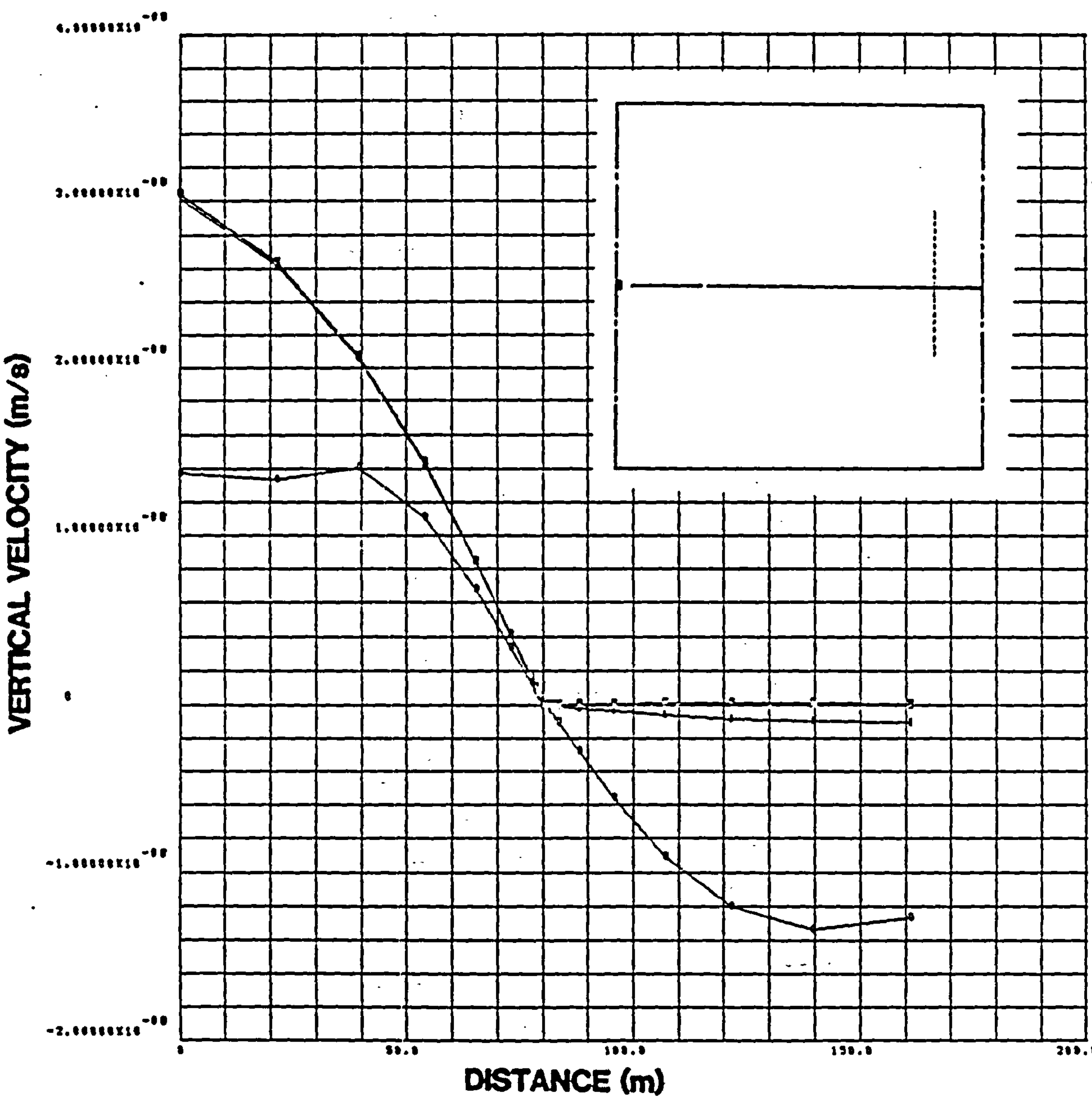

Figure 60. Vertical Component of Superficial Velocity as a Function of Position -- Emplacement Scheme 3 (θ_{drift}/ϕ = 0.47)

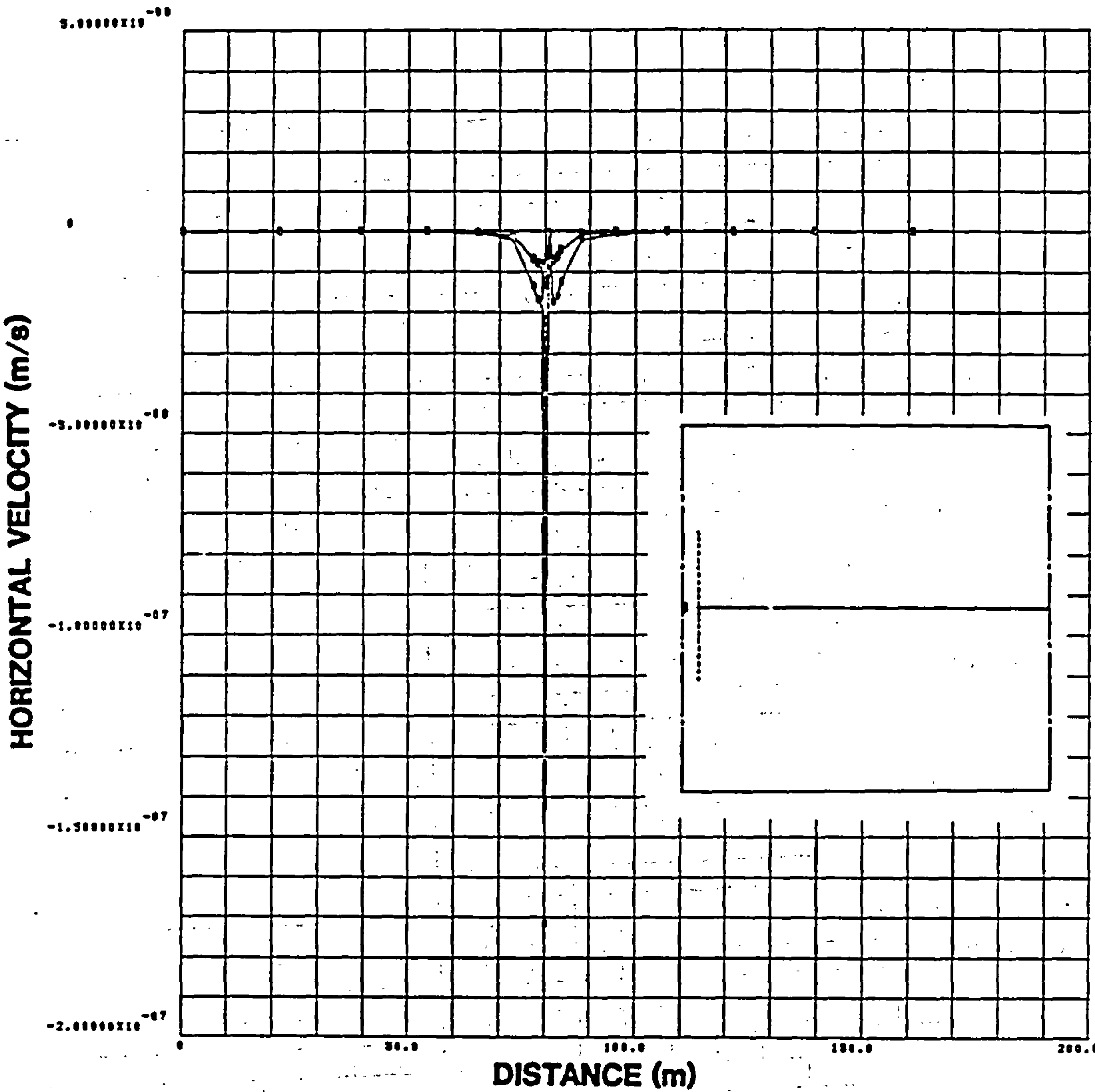

Figure 61. Horizontal Component of Superficial Velocity as a Function of Position -- Emplacement Scheme 3 (θ_{drift}/ϕ = 0.78)

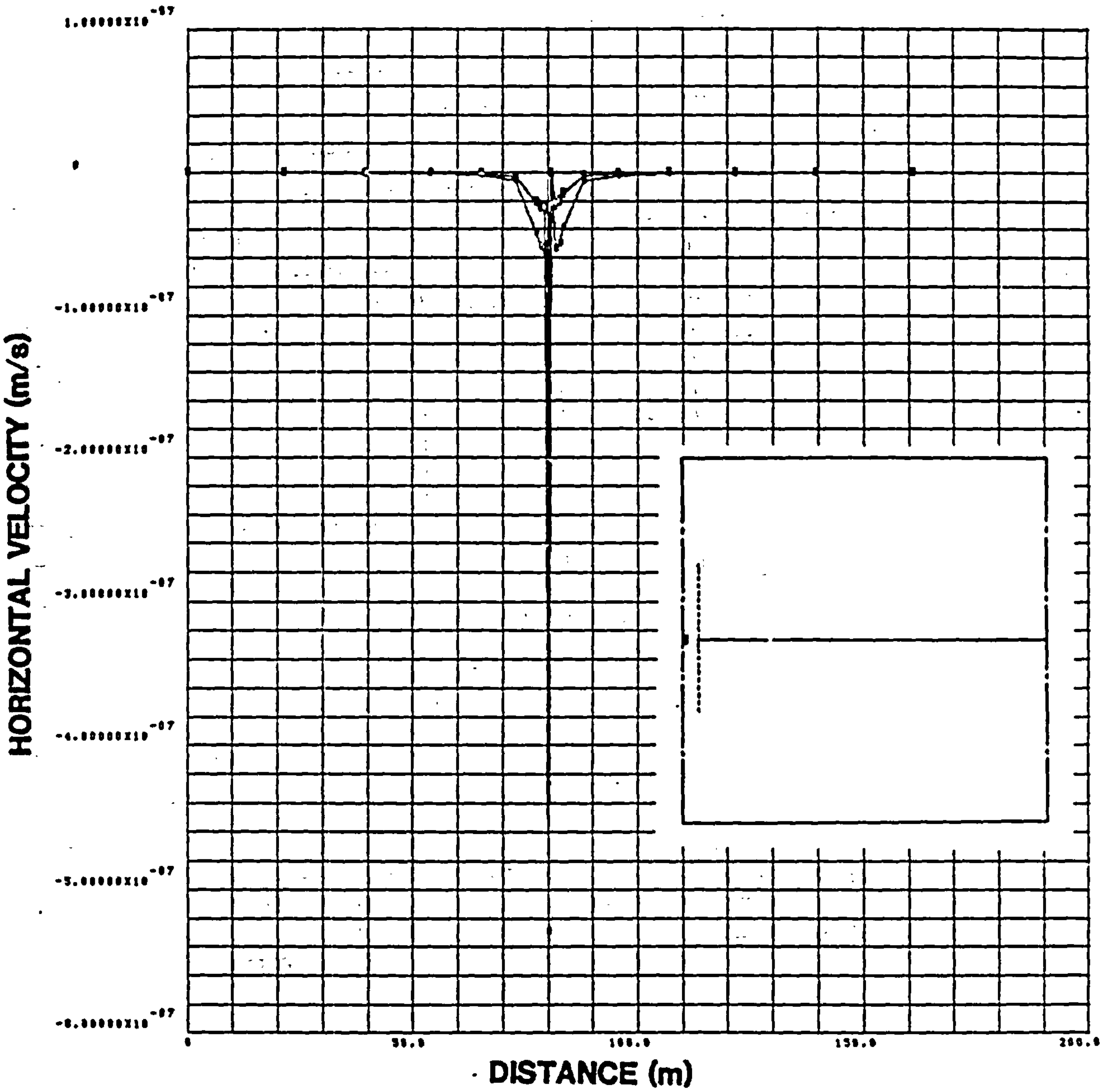

Figure 62. Horizontal Component of Superficial Velocity as a Function of Position -- Emplacement Scheme 3 ($\theta_{drift}/\phi = 0.751$)

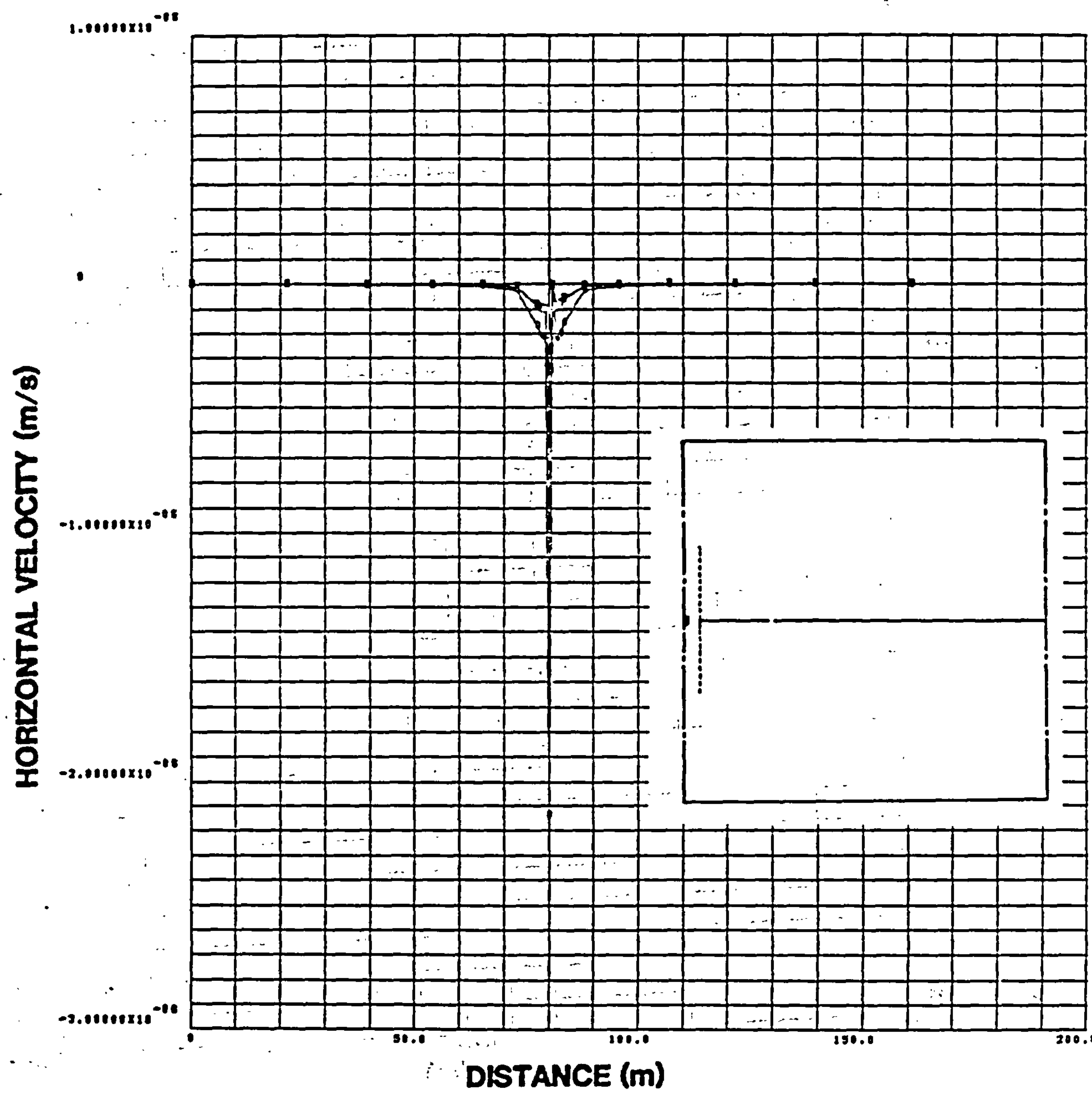

Figure 63. Horizontal Component of Superficial Velocity as a Function of Position -- Emplacement Scheme 3 (θ_{drift}/ϕ = 0.635)

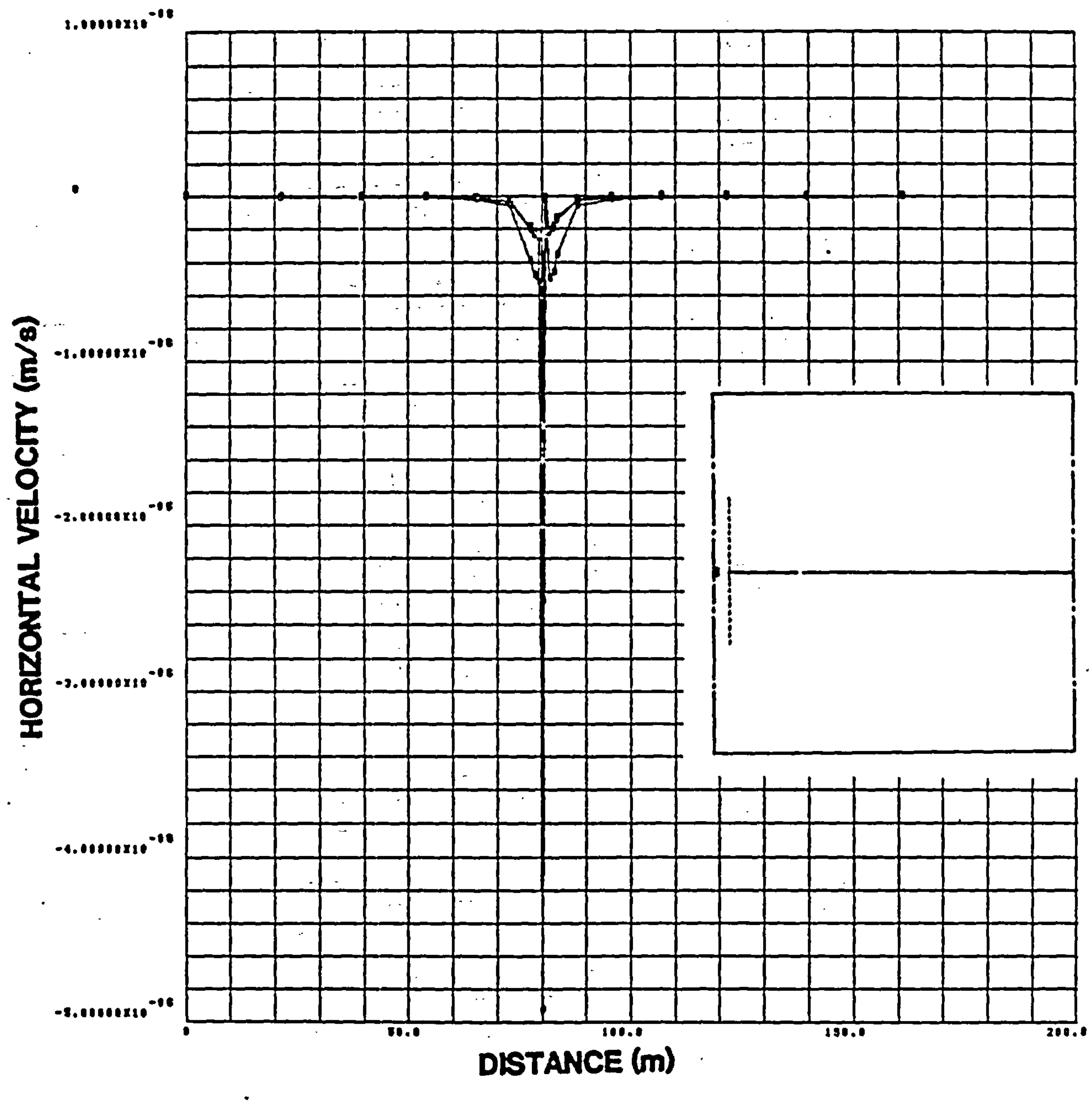

Figure 64. Horizontal Component of Superficial Velocity as a Function of Position -- Emplacement Scheme 3 (θ_{drift}/ϕ = 0.47)

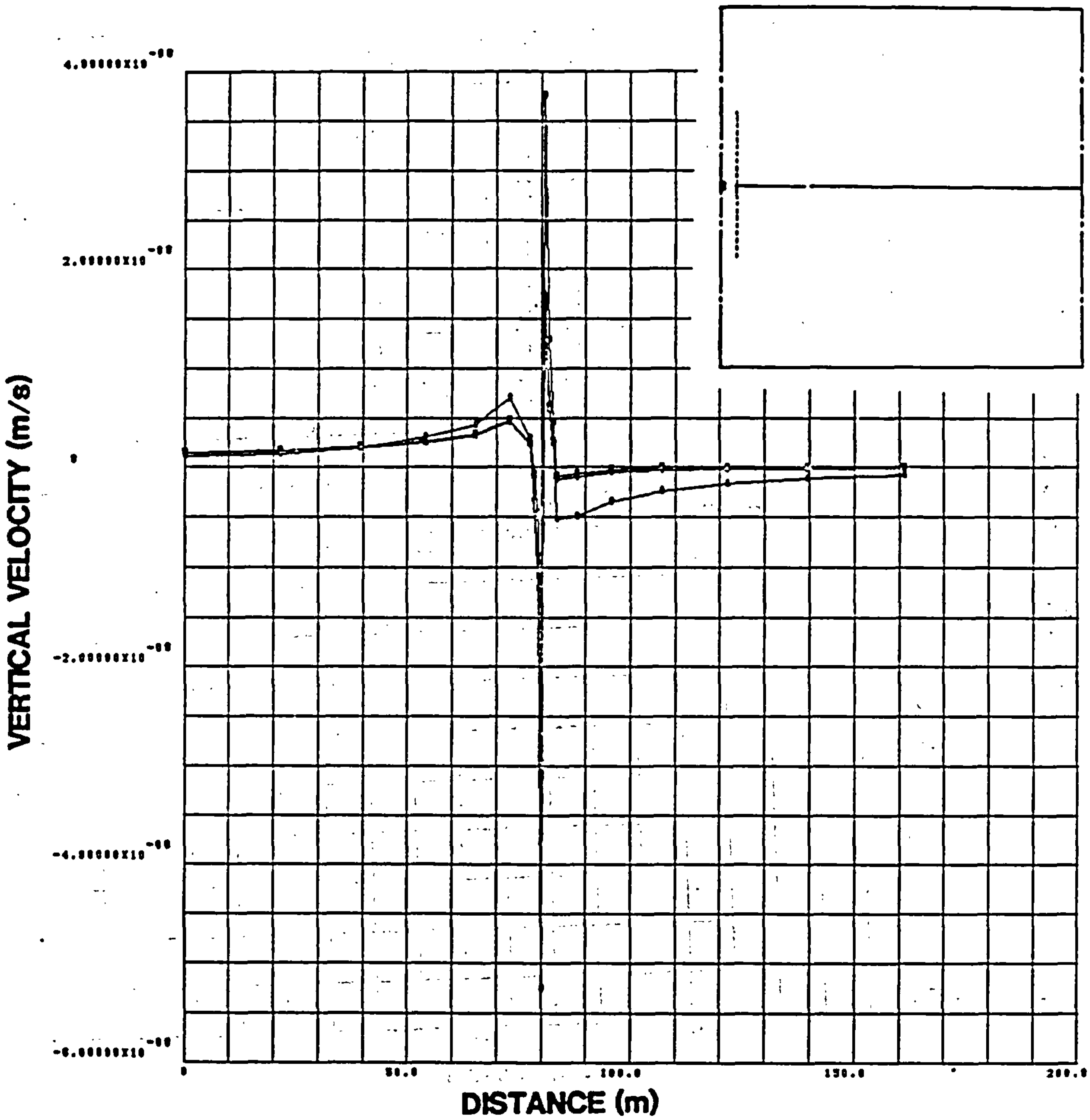

Figure 65. Vertical Component of Superficial Velocity as a Function of Position -- Emplacement Scheme 3 (θ_{drift}/ϕ = 0.78)

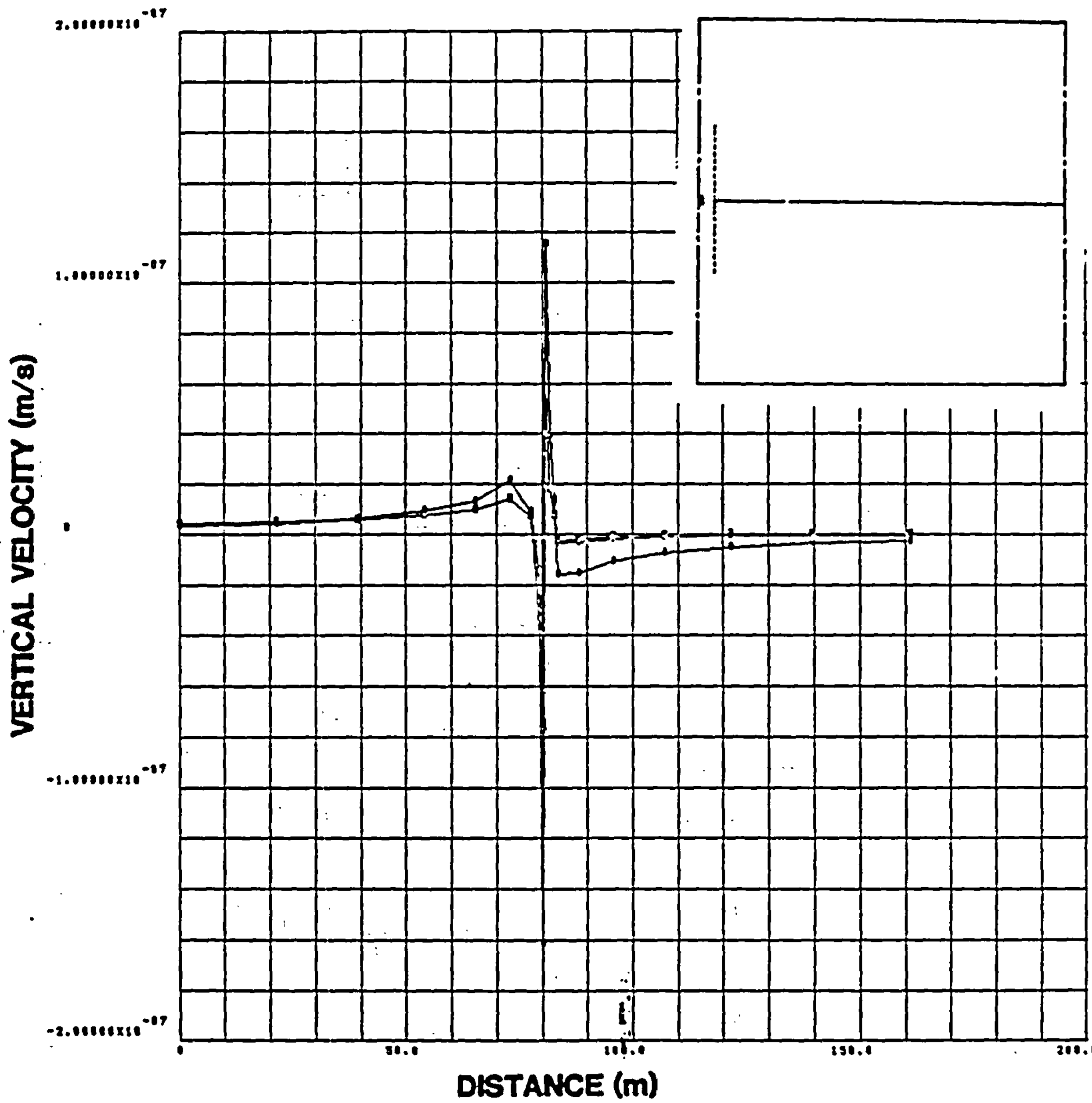

Figure 66. Vertical Component of Superficial Velocity as a Function of Position -- Emplacement Scheme 3 (θ_{drift}/ϕ = 0.751)

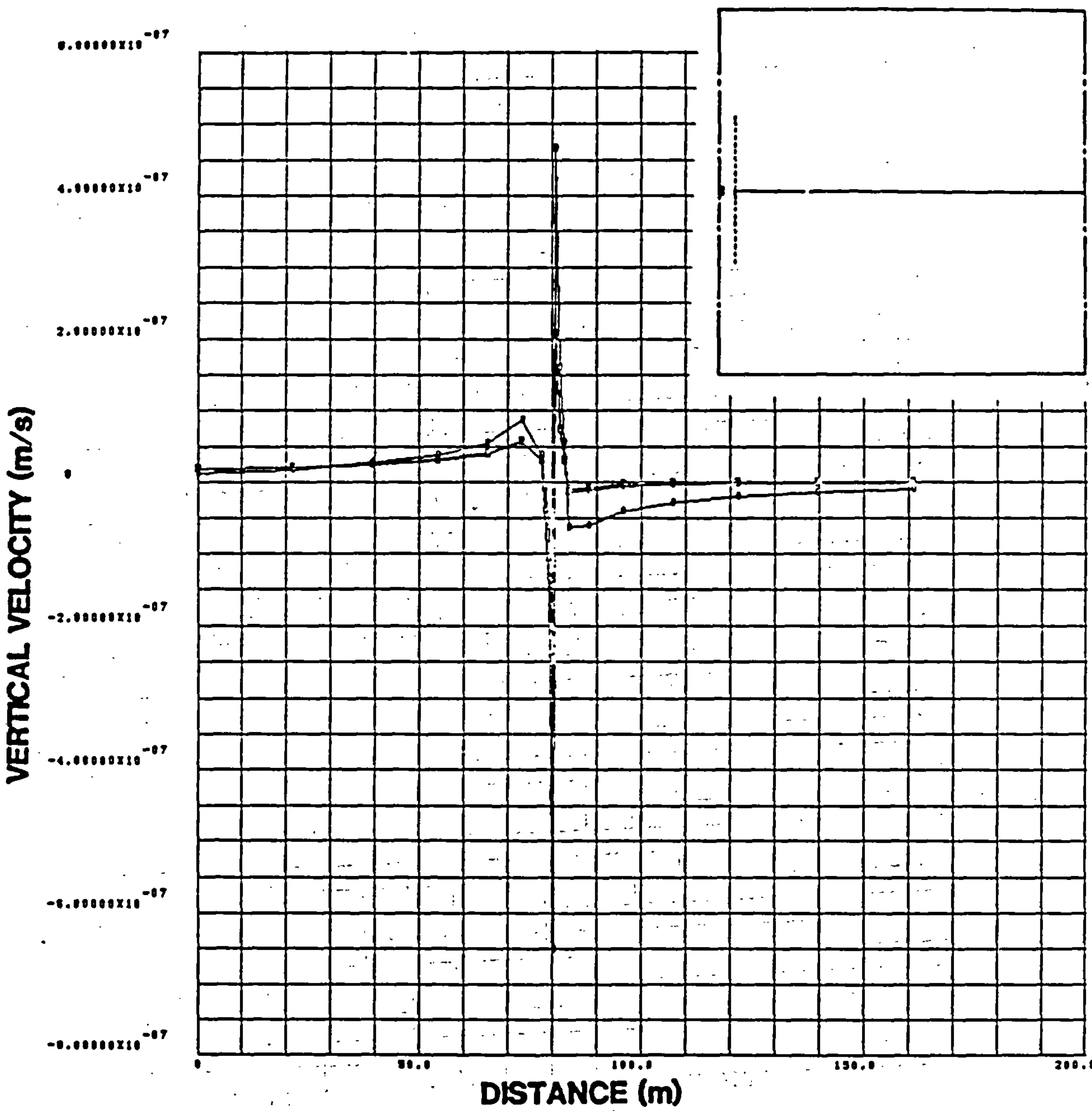

Figure 67. Vertical Component of Superficial Velocity as a Function of Position -- Emplacement Scheme 3 (θ_{drift}/ϕ = 0.635)

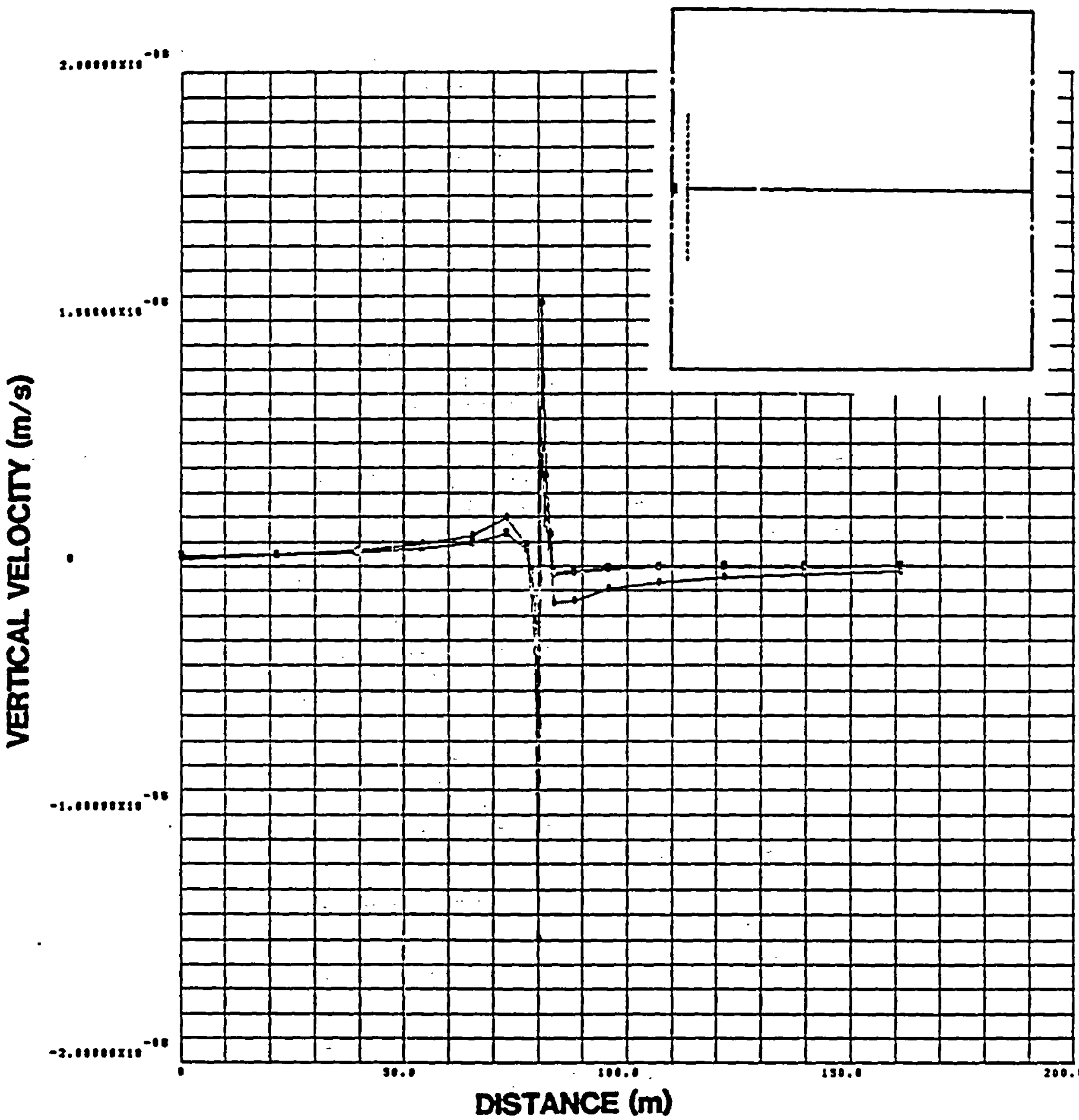

Figure 68. Vertical Component of Superficial Velocity as a Function of Position -- Emplacement Scheme 3 ($\theta_{drift}/\phi = 0.47$)

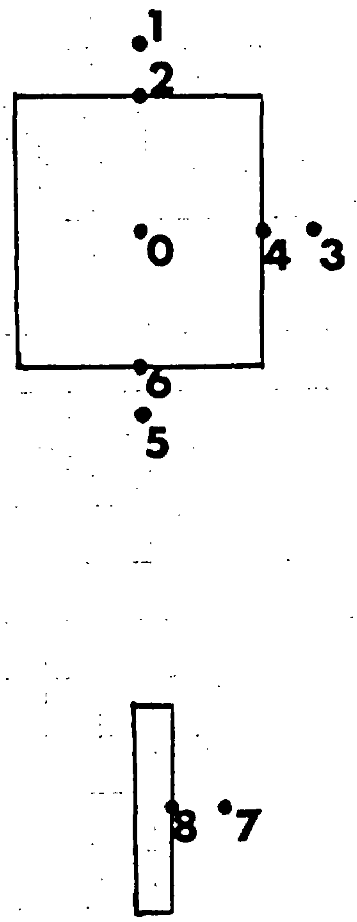

Figure 69. Legend for Figures 70-72

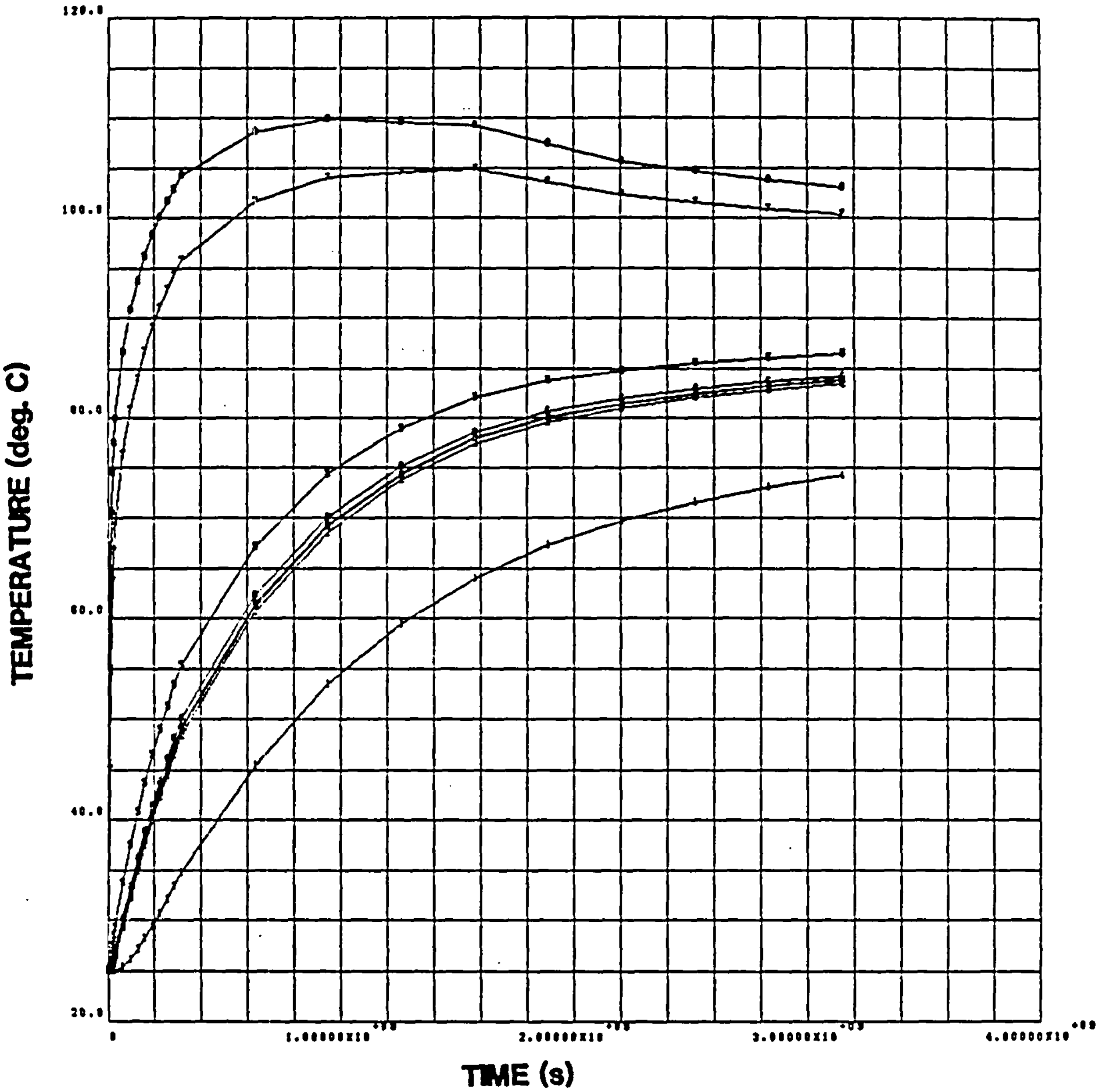

Figure 70. Temperature Histories (Partially Saturated -- No Convection)

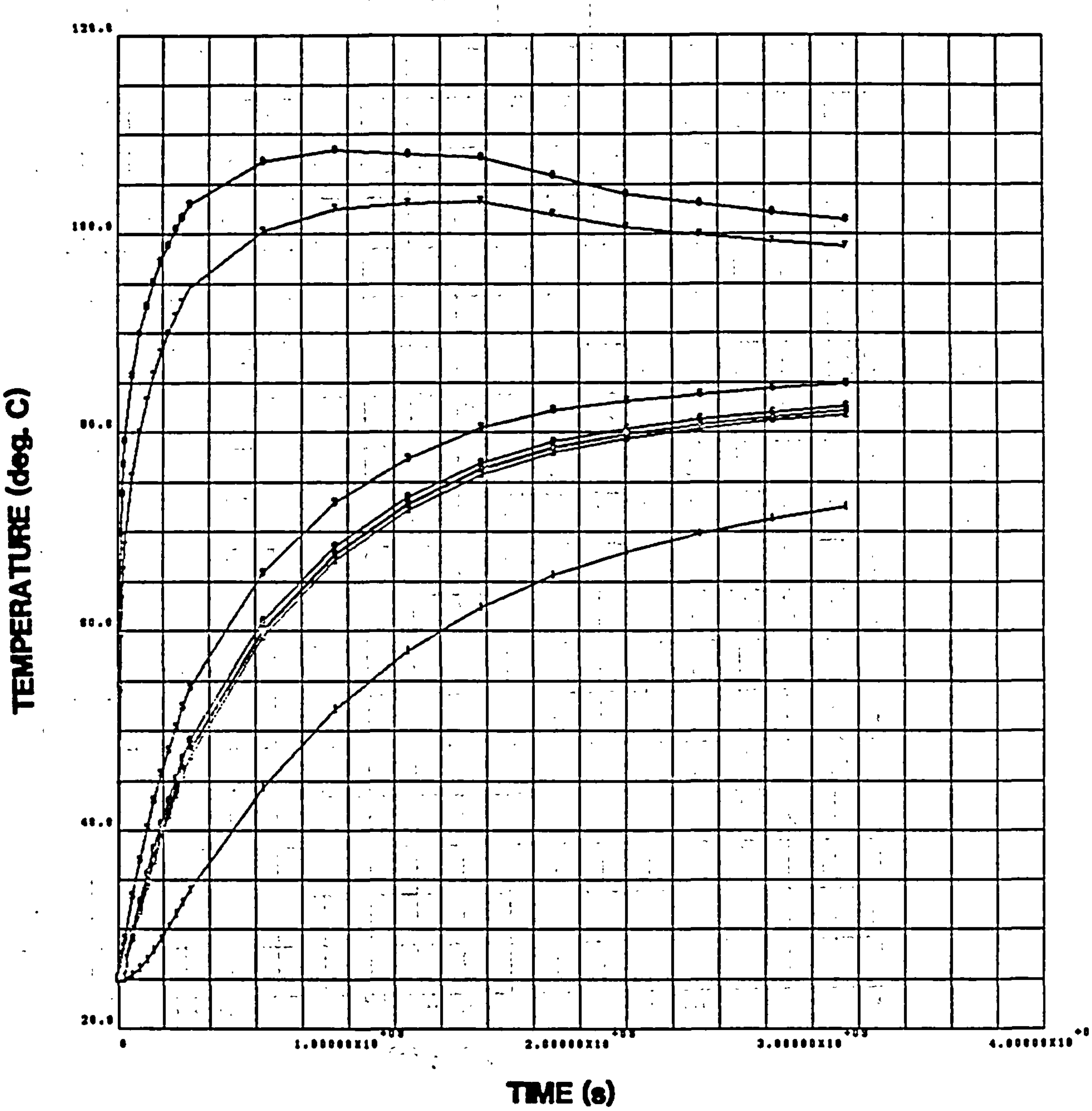

Figure 71. Temperature Histories (Saturated -- Convection)

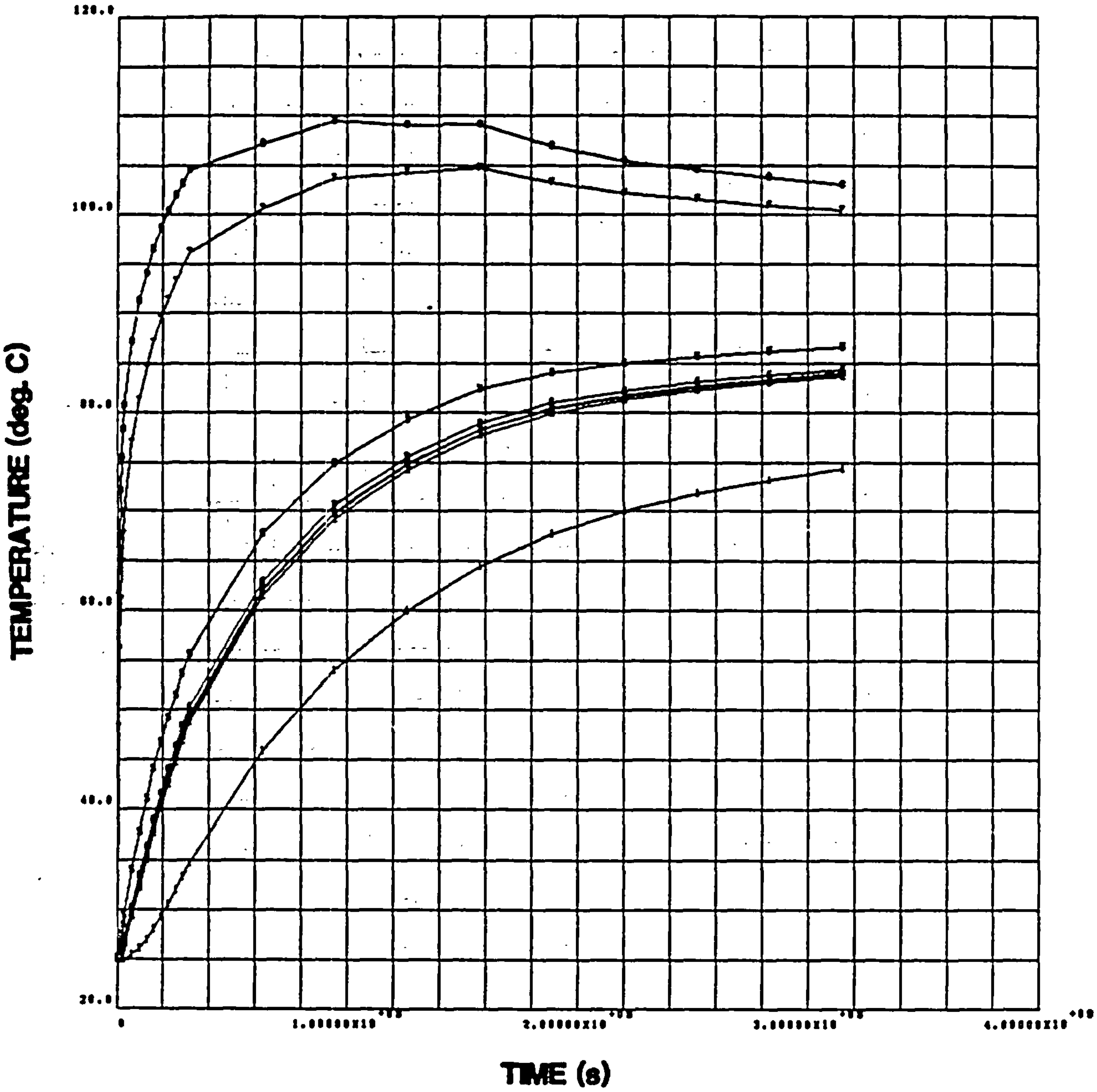

Figure 72. Temperature Histories (COYOTE)

Distribution:
Unlimited Release
UC-70

J. W Bennett, Director
Geologic Repository Division
U.S. Department of Energy
S-10
Washington, DC 20545

M. W. Frei
Geologic Repository Division
U.S. Department of Energy
S-10
Washington, DC 20545

C. R. Cooley
Geologic Repository Division
U.S. Department of Energy
S-10
Washington, DC 20545

C. H. George
Geologic Repository Division
U.S. Department of Energy
S-10
Washington, DC 20545

J. J. Fiore
Geologic Repository Division
U.S. Department of Energy
S-10
Washington, DC 20545

J. G. Vlahakis
Geologic Repository Division
U.S. Department of Energy
S-10
Washington, DC 20545

T. P. Longo
Geologic Repository Division
U.S. Department of Energy
S-10
Washington, DC 20545

C. Klingsberg
Geologic Repository Division
N.S. Department of Energy
S-10
Washington, DC 20545

NTS Project Manager
High-Level Waste Technical
Development Branch
Division of Waste Management
U.S. Nuclear Regulatory Commission
Washington, DC 20555

Chief, High-Level Waste Technical
Development Branch
Division of Waste Management
U.S Regulatory Commission
Washington, DC 20555

J. O. Neff, Program Manager
National Waste Terminal
Storage Program Office
U.S. Department of Energy
505 King Avenue
Columbus, OH 43201

N. E. Carter
Battelle
Office of Nuclear Waste Isolation
505 King Avenue
Columbus, OH 43201

ONWI Library (5)
Battelle
Office of Nuclear Waste Isolation
505 King Avenue
Columbus, OH 43201

O. L. Olson, Project Manager
Basalt Waste Isolation Project Office
U.S. Department of Energy
Richland Operations Office
Post Office Box 550
Richland, WA 99352

R. Deju
Rockwell International Atomics
International Division
Rockwell Hanford Operations
Richland, WA 99352

G. Tomsic
Utah Dept. of Community
Economic Development
Room 6290, State Office Bldg.
Salt Lake City, UT 89114

Distribution (cont.).

Governor's Office Planning Coordinator
Nevada State Planning Coord.
State Capitol Complex 2nd Floor
Carson City, NV 89710

P. J. Iverson Deputy Director
Department of Minerals
State of Nevada
400 West King Street
Carson City, NV 39710

R. R. Loux. Jr.
c/o Department of Minerals
State of Nevada
400 West King Street
Carson City, NV 89710

K. Street, Jr.
Lawrence Livermore National Laboratory
Mail Stop L-209
P O. Box 808
Livermore, CA 94550

L. D. Ramspott
Technical Project Office
Lawrence Livermore National Laboratory
P.O. Box 808
Mail Stop L-204
Livermore, CA 94550

D. C Hoffman
Los Alamos National Laboratory
P.O. Box 1663
Mail Stop E-515
Los Alamos NM 87545

D. T. Oakley
Technical Project Officer
Los Alamos National Laboratory
P.O. Box 1663
Mail Stop F-671
Los Alamos, NM 87545

M Spaeth (3)
Science Applications, Inc.
2769 South Highland Drive
Las Vegas, NV 89109

A. R. Hakl Site Manager
Westinghouse - AESD
P. O. Box 708
Mail Stop 703
Mercury, NV 89023

P. O. Aamodt
Los Alamos National Laboratory
P.O. Box 14100
Las Vegas, NV 89114

D. L. Vieth Director (6)
Waste Management Project Office
U.S. Department of Energy
P.O. Box 14100
Las Vegas, NV 89114

D. F. Miller, Director
Office of Public Affairs
U.S. Department of Energy
P.O. Box 14100
Las Vegas, NV 89114

D. A Nowack (11)
U.S. Department of Energy
P.O. Box 14100
Las Vegas, NV 89114

B. W. Church, Director
Health Physics Division
U.S. Department of Energy
P.O. Box 14100
Las Vegas, NV 89114

A. E. Gurrola
Holmes & Narver Inc.
P.O. Box 14340
Las Vegas, NV 89114

W. W. Dudley, Jr.
Technical Project Officer
U.S. Geological Survey
P.O. Box 25046
Mail Stop 418
Federal Center
Denver, CO 80225

W. S. Twenhofel
820 Estes Street
Lakewood, CO 80215

Distribution (cont.)

H. D. Cunningham
Reynolds Electrical &
Engineering Company, Inc.
P.O Box 14400
Mail Stop 555
Las Vegas, NV 89114

R. H Marks
U.S. Department of Energy
CP-1, M/S 210
P.O. Box 14100
Las Vegas, NV 89114

J A. Cross
Fenix & Scisson, Inc
P.O. Box 15408
Las Vegas, NV 89114

Internal Distribution:

1510 D. B. Hayes
1511 J. W. Nunziato
1511 N. E. Bixler
1511 R. R. Eaton
1511 M. J. Martinez
1511 R. K. Wilson
1512 J. C. Cummings
1512 L. A. Mondy (8)
1513 D W. Larson
1520 T. B. Lane
1521 R D. Krieg
1524 W. N. Sullivan
1530 L. W. Davison
1540 W. C. Luth
7417 F. W. Muller
8120 L. D. Bertholf
9730 W. D. Weart
9760 R. W. Lynch
9761 L. W. Scully (3)
9761 A. J. Mansure
9762 L. D. Tyler
9762 J. K. Johnstone
9762 J. P. Branner
9762 R. R. Peters
9762 N. K. Hayden
9762 Y. T. Lin
9763 J. R. Tillerson
9763 R. M. Zimmerman
9763 J. A. Fernandez
8214 M. A. Pound
3141 L. J. Erickson (5)
3151 W. L. Garner (3)
for DOE/TIC
DOE/TIC (25)
(C. H. Dalin, 3154-3)